https://doi.org/10.5194/egusphere-2025-6210
Preprint. Discussion started: 22 January 2026

Implementing methane dynamics into the LPJmL6 model

Sibyll Schaphoff[1], David Hötten[1,2], Christoph Müller[1], Dieter Gerten[1,3], Sebastian Ostberg[1], and Werner von Bloh[1]

[1]Potsdam Institute for Climate Impact Research (PIK), Member of the Leibniz Association, Potsdam, Germany
[2]Freie Universität Berlin (FU Berlin)
[3]Geography Department, Humboldt-Universität zu Berlin, 10099 Berlin

Correspondence: Sibyll Schaphoff (Sibyll.Schaphoff@pik-potsdam.de)

Abstract. We extend the Dynamic Global Vegetation Model LPJmL to version 6.0 by explicitly representing methane (CH_4) dynamics within the coupled carbon–nitrogen–water system. The implementation (i) prognoses water-table depth and wetland extent using a CTI–TOPMODEL framework, (ii) solves sub-daily, vertically explicit mass balances for CH_4 and O_2 including diffusion, ebullition, and plant-mediated transport, (iii) represents methanogenesis and methanotrophy with temperature- and moisture-dependent kinetics, and (iv) integrates land-use and rice management effects alongside inundation-tolerant plant functional types. This architecture enables consistent simulation of CH_4, carbon dioxide (CO_2) and nitrous oxide (N_2) emissions from natural wetlands and managed systems together with the soil CH_4 sink. Extensive benchmarking against global datasets shows that LPJmL6 reproduces the magnitude and regional–temporal variability of CH_4 flux pathways while maintaining strong skill in the simulated terrestrial carbon, nitrogen, and water budgets. The model thus provides a coherent, process-based framework to quantify CH_4 within the coupled carbon–nitrogen–water system, elucidate interactions with vegetation and soils, and assess how land-use, wetland conservation and restoration, and rice management options affect methane and overall greenhouse–gas budgets in support of climate-mitigation strategies.

1 Introduction

Wetlands, including ponds, lakes, rivers, and marshes are responsible for approximately 30% of global methane (CH_4) emissions (Saunois et al., 2020). These unique ecosystems are characterized by water-saturated conditions that create anoxic environments promoting methanogenic processes. However, wetland dynamics, such as changes in its water balance and vegetation, can significantly impact CH_4 emissions (Yang et al., 2022).

The variability in wetland CH_4 emissions is governed by several environmental factors, including water table depth, temperature, vegetation type, nutrient availability, and air pressure (Whalen and Reeburgh, 1991; Bartlett and Harriss, 1992; Moore et al., 2011; Turetsky et al., 2014; Bloom et al., 2017b). These factors regulate the balance between oxic and anoxic decomposition, which determine CH_4 production and release under anoxic conditions and carbon dioxide production and release under oxic conditions. Water table depth, controlled by precipitation, evapotranspiration, and soil conditions, is a key driver of anoxic conditions necessary for methanogenesis. A high

https://doi.org/10.5194/egusphere-2025-6210
Preprint. Discussion started: 22 January 2026

water table limits O_2 diffusion, promoting CH_4 production, while a low water table fosters oxic decomposition and CH_4 oxidation (Turetsky et al., 2014; Whalen and Reeburgh, 1991). Temperature also influences CH_4 emissions by affecting microbial activity, with soil temperature driving methanogenesis rates and water temperature influencing gas solubility and diffusion (Moore et al., 2011). Vegetation impacts CH_4 fluxes by transporting CH_4 via aerenchyma tissues and contributing organic substrates that fuel microbial processes (Bartlett and Harriss, 1992). Nutrient availability further shapes microbial activity, influencing the balance between CH_4 production and oxidation (Bloom et al., 2017a). Atmospheric pressure and vapor pressure deficit (VPD) indirectly affect emissions by influencing gas diffusion and soil moisture dynamics (Moore et al., 2011).

These interrelated factors underscore the complexity of CH_4 emissions from wetlands and their role in global greenhouse gas budgets. While the emission sources are diverse (including fossil fuel and waste (Saunois et al., 2020)), this paper focuses on the specific issue of CH_4 emissions from land use (excluding direct livestock emissions, which are governed by feed quantity, quality and livestock stocking densities (Heinke et al., 2023)) and from natural peatlands. Understanding and quantifying these emissions is vital for developing effective climate mitigation strategies and improving insights into the carbon cycle and its role in global climate systems.

We have implemented the main processes controlling CH_4 dynamics in an updated version of the Dynamic Global Vegetation Model, LPJmL (Lund-Potsam-Jena managed land; Schaphoff et al., 2018; von Bloh et al., 2018). This enhanced model simulates the intricate dynamics of natural and anthropogenic CH_4 emissions within the terrestrial biosphere, integrating wetland and permafrost dynamics as part of the coupled global carbon and water cycles.

In this work, we extend the LPJmL model from version 5.10 (von Bloh et al., 2018; Lutz et al., 2019; Wirth et al., 2024) to version 6.0 by incorporating processes that represent CH_4 dynamics. Specifically, we introduce a dynamic representation of the water table to determine the surface area influenced by the unconfined aquifer. This, combined with simulated O_2 and CH_4 concentrations in soil layers, enables the estimation of wetland distribution and anaerobic soil conditions. Consequently, the model now simulates CH_4 generation, concentrations in soil layers, and fluxes to the atmosphere, fully integrated with the hydrological and biogeochemical processes of LPJmL.

Following the documentation of this new implementation, we provide a global evaluation of key processes related to wetland and CH_4 dynamics, along with other relevant processes, to assess the overall performance of LPJmL6.

2 Module description

This module description focuses on the newly developed part of the model. A general description of the LPJmL model can be found in Schaphoff et al. (2018) and in subsequent descriptions and evaluations of further model extensions, i.e. von Bloh et al. (2018); Lutz et al. (2019); Wirth et al. (2024). Additional changes are documented in the Supplement and together constitute LPJmL5.10.2. Wetlands are the primary natural sources of CH_4 production, while agricultural land is a major source of human-caused CH_4 emissions. In LPJmL6, we consider both natural and

https://doi.org/10.5194/egusphere-2025-6210
Preprint. Discussion started: 22 January 2026

anthropogenic sources of CH_4 emissions. Given the large computational cost of the simulation of CH_4 soil processes, this can be turned off for simulations with LPJmL6 that are not aiming at studying CH_4 dynamics (see Supplement).

Each grid cell is divided into several sub-regions, called stands, which represent different land-cover and land-use types. We distinguish a natural wetland stand, natural upland stand, several agricultural stands, pasture stands and setaside stands. Managed land-cover types are further distinguished into rainfed and irrigated stands. The introduction of the natural wetland stand makes the conversion of different land-use types more complex in LPJmL6 compared to earlier versions (see section 2.5).

2.1 Wetland representation

We compute the water–saturated area in each 0.5° grid cell from the compound topographic index (CTI), which describes the propensity of a location to accumulate water (Beven and Kirkby, 1979) and is defined as

$$\mathrm{CTI}_i = \ln\left(\frac{\alpha_i}{\tan(\beta_i)}\right), \tag{1}$$

where α_i is the upslope contributing area and β_i the local surface slope at point i. In our implementation, CTI and slope statistics at 0.5° resolution are taken from the topographic datasets described in the section 4.1. Within each grid cell, CTI values are used to represent subgrid-scale variations in wetness and to derive the saturated fraction following a TOPMODEL–type approach (Beven and Kirkby, 1979; Sivapalan et al., 1987; Kleinen et al., 2012).

To relate CTI_i to water-table depth we follow the TOPMODEL framework Beven and Kirkby (1979):

$$z_{\Delta_i} = \bar{z}_\Delta + \frac{1}{f}\cdot(\mathrm{CTI}_i - \overline{\mathrm{CTI}}), \tag{2}$$

where z_{Δ_i} is the local stand specific water table depth at point i (measured relative to the soil surface, with $z_{\Delta_i} = 0$ at the surface), $\bar{z}_\Delta$ the grid cell mean water table depth, $\overline{\mathrm{CTI}}$ is the grid cell mean CTI, and f (m^{-1}) is a soil-dependent parameter describing the exponential decline of transmissivity with depth (see Table 1). Areas are considered saturated when the water table reaches the soil surface, i.e. when $z_{\Delta_i} = 0$. The corresponding threshold CTI value for saturation $\mathrm{CTI}_{\mathrm{sat}}$ follows from Eq. 2:

$$0 = \bar{z}_\Delta + \frac{1}{f}\cdot(\mathrm{CTI}_{\mathrm{sat}} - \overline{\mathrm{CTI}}) \tag{3}$$

Rearranging Eq. 3 yields:

$$\mathrm{CTI}_{\mathrm{sat}} = \overline{\mathrm{CTI}} - f\cdot\bar{z}_\Delta. \tag{4}$$

Within each grid cell we assume that CTI_i follows a gamma distribution (Sivapalan et al., 1987; Kleinen et al., 2012). The parameters of this distribution are estimated from the mean, standard deviation and skewness of CTI_i

https://doi.org/10.5194/egusphere-2025-6210
Preprint. Discussion started: 22 January 2026

Table 1. Soil–type specific parameters for calculation of the saturation area and of the water table depth

Soil type	f in m^{-1}	Ψ_{min} in mm	B_{min}
clay	2.0	-467.7	11.4
silty clay	1.9	-323.6	10.4
sandy clay	1.6	-97.7	10.4
clay loam	1.5	-263.0	8.52
silty clay loam	1.6	-616.6	7.75
sandy clay loam	1.3	-134.9	7.12
loam	1.2	-354.8	5.39
silt loam	1.3	-758.6	5.3
sandy loam	1.2	-141.3	4.9
silt	1.5	-758.6	5.3
loamy sand	1.0	-36.3	4.38
sand	0.8	-69.2	4.05

f describes the decline of transmissivity with depth,
Ψ_{min} is the saturated soil matric potential for mineral soil,
B_{min} is the Clapp – Hornberger exponent (Lawrence and Slater, 2008).

(see section 4.1). The saturated fraction of the grid cell is then given by the probability that $CTI_i \geq CTI_{sat}$, i.e. by the upper tail of the gamma distribution computed from its cumulative distribution function. This fraction defines the inundated area of the grid cell.

The calculation is repeated annually using the annual mean of $\bar{z}_\Delta$; temporal changes in $\bar{z}_\Delta$ therefore translate into changes in wetland extent. The computation of $\bar{z}_\Delta$ is described in section 2.2.

2.2 Soil water balance

Soil water dynamics are represented by a multi-layer model with layer thicknesses of 200, 300, 500, 1000, and 1000 mm. Vertical soil moisture transport in this model is governed by infiltration and percolation. Water is lost from the soil column through transpiration, soil evaporation, surface and lateral runoff, and sub-surface drainage, which in LPJmL6 is influenced by interactions with groundwater (see below).

2.2.1 Infiltration

The processes of vertical water movement in the soil column have remained unchanged since their initial description by Schaphoff et al. (2018) and Lutz et al. (2019). However, infiltration of daily rainfall and applied irrigation amounts (P; in mm) is now influenced by topography and is modified by accounting for a contribution to surface runoff (β_{HAG}), which depends on the mean slope gradient of the stand (β):

https://doi.org/10.5194/egusphere-2025-6210
Preprint. Discussion started: 22 January 2026

$$infil = P \cdot (1 - \beta_{\mathrm{HAG}} + \alpha \cdot \beta_{\mathrm{HAG}}), \tag{5}$$

where α is the factor representing the dependence on soil water conditions as described in Schaphoff et al. (2018):

$$\alpha = \left(1 - \frac{\mathrm{W}_{\mathrm{liq}(1)} + \mathrm{W}_{\mathrm{ice}(1)}}{(\theta_{\mathrm{sat}(1)} - \mathrm{w}_{\mathrm{pwp}(1)}) \cdot z_{(1)}}\right)^{\frac{1}{\Phi_{\mathrm{inf}}}}, \tag{6}$$

based on the first layer's relative volumetric soil water content at saturation ($\theta_{\mathrm{sat}_{(1)}}$), the relative soil water content at the wilting point ($\mathrm{w}_{\mathrm{pwp}(1)}$), and its actual soil water content ($\mathrm{W}_{\mathrm{liq}_{(1)}}$ in mm) and the actual ice content ($\mathrm{W}_{\mathrm{ice}_{(1)}}$ in mm) of the first layer. $z_{(1)}$ is the layer thickness (in mm). The factor α is scaled with Φ_{inf}, to account for the actual above-ground litter layer cover fraction as described in (Lutz et al., 2019). P is routed through the soil column partitioned into packets of maximum 4 mm at a time. The newly added Haggard function relates the slope gradient (β) to the fraction of non-infiltrating water contributing to surface runoff (Haggard et al., 2005):

$$\beta_{\mathrm{HAG}} = \frac{0.06 \cdot \ln(\beta + 0.1) + 0.22}{0.43}. \tag{7}$$

Infiltrated water is routed through the soil column depending on the hydraulic conductivity of the soil layer and the soil moisture of the layer below (Schaphoff et al., 2018; Lutz et al., 2019) down to the layer of the water table. The percolation of the last unsaturated layer recharges the ground water, and thus the model is able to simulate the temporal variation of the water stored in the unconfined aquifer (W_a). Lateral runoff is determined by the groundwater–soil water interactions which is adopted from the CLM4.5 model (Riley et al., 2011; Niu and Yang, 2006; Niu et al., 2005).

2.2.2 Drainage

Subsurface drainage (i.e. groundwater discharge) ($\mathrm{q}_{\mathrm{drain}}$) is distinguished between completely and partially frozen and completely unfrozen conditions of the layers below the groundwater table. In the unfrozen state:

$$q_{\mathrm{drain}} = q_{\mathrm{drain,max}} \cdot \exp(-f_{\mathrm{drain}} \cdot z_{\Delta}), \tag{8}$$

where $f_{\mathrm{drain}} = 2.0\ \mathrm{m}^{-1}$ is a decay factor describing the exponential decrease of drainage with increasing mean water table depth (z_{Δ}). The local maximum subsurface drainage rate ($q_{\mathrm{drain,max}}$ at $z_{\Delta} = 0$) depends on the stand-specific topographic slope β:

$$q_{\mathrm{drain,max}} = \mathrm{max}_{\mathrm{drain}} \cdot \tan^2(\beta). \tag{9}$$

https://doi.org/10.5194/egusphere-2025-6210
Preprint. Discussion started: 22 January 2026

The reference parameter $\max_{\text{drain}}$ is set to 50 mm day^{-1} following Christen et al. (2006) and increased to 100 mm day^{-1} for agricultural land to mimic enhanced field drainage. The subsurface drainage rate for the at least partially frozen state is:

$$q_{\text{perched}} = \Theta_{\text{ice}} \cdot \max_{\text{perch}} \cdot k_{\text{s}} \cdot (z_{\text{frost}} - z_{\Delta}). \tag{10}$$

Lateral drainage above the frozen soil column depends on the saturated hydraulic conductivity (k_s), and the maximum rate $\max_{\text{perch}}$, equivalent to $\max_{\text{drain}}$ for sub-soil dynamics, is assumed to be 50 mm day^{-1}, but is strongly limited by Θ_{ice} that gives the ice impedance factor (Swenson et al., 2012a). z_{frost} is the depth at which the soil is frozen. Drainage only occur when $z_{\text{frost}} > z_{\Delta}$. Θ_{ice} is calculated from the ice content of the layer that is partly frozen. It describes the increased tortuosity of the water flow when parts of the pore space are filled with ice:

$$\Theta_{\text{ice}} = 10^{-\Omega \cdot \text{icefrac}} \tag{11}$$

and

$$\text{icefrac} = \int_0^{\text{soildepth}} F_{\text{ice}}(z)/\text{soildepth}\,\mathrm{d}z, \tag{12}$$

where $F_{\text{ice}} = \frac{\theta_{\text{ice}}}{\theta_{\text{sat}}}$ is the frozen part of the water filled pore space relating θ_{sat}, the relative water content at saturation (m^3 water pro m^3 soil), to the ice content relative to the soil porosity. If the soil is saturated and all water is frozen F_{ice} is at unity. Ω is a parameter set to 6 following Swenson et al. (2012b), to meet the impedance of frozen ground.

2.2.3 Water table depth calculation

This section describes how the water table depth (and therefore the groundwater level) changes depending on the exchange of water between the saturated zone (below the water table) and the unsaturated zone (above it). The equilibrium matric potential and corresponding water content follow the hydrostatic formulation of Zeng and Decker (2009), as implemented in the Community Land Model-CLM4.5 (Oleson et al., 2013) , and used for dynamic groundwater–soil coupling and recharge calculation following Swenson and Lawrence (2014). The recharge rate $q_{recharge}$ of the water table depth can be determined by applying Darcy's law to z_{Δ}:

$$q_{\text{recharge}} = -k_{\text{aq}} \cdot \frac{\Psi_{\Delta} - \Psi_{(\text{lwt})}}{z_{\Delta} - z_{(\text{lwt})}}, \tag{13}$$

where Ψ_{Δ} and $\Psi_{(\text{lwt})}$ are the soil matric potential at z_{Δ} and of the layer above z_{Δ}, where lwt is the index of this layer. k_{aq} is the hydraulic conductivity of the layer which contains the water table and is calculated as follows:

https://doi.org/10.5194/egusphere-2025-6210
Preprint. Discussion started: 22 January 2026

$$k_{\mathrm{aq}} = \Theta_{\mathrm{ice,(lwt+1)}} \cdot k_s \cdot \left(\frac{\theta_{(lwt+1)}}{\theta_{\mathrm{sat,(lwt+1)}}} \right)^{2 \cdot B_{(\mathrm{lwt}+1)}+3} . \tag{14}$$

$\Psi_{(\mathrm{lwt})}$ is not simply a constant, it depends on how the soil would behave under hydrostatic equilibrium at the current water–table depth (z_Δ). $\Psi_{(\mathrm{lwt})}$ represents the equilibrium potential at the interface between saturated and unsaturated zones and is described by the saturated soil matric potential of the different soil types (Ψ_{sat}), the relation of the volumetric water content above the water table ($\theta_{(\mathrm{lwt})}$ in m^3 water pro m^3 soil) and θ_{sat}:

$$\Psi_{(\mathrm{lwt})} = \Psi_{\mathrm{sat,(lwt)}} \cdot \left(\frac{\theta_{(\mathrm{lwt})}}{\theta_{\mathrm{sat,(lwt)}}} \right)^{-B_{(\mathrm{lwt})}} . \tag{15}$$

The Clapp – Hornberger exponent ($B_{(\mathrm{lwt})}$) is an empirical parameter that controls the steepness of the soil water retention curve (Clapp and Hornberger, 1978), describing how rapidly soil suction increases as the soil dries. When the soil is saturated ($\theta = \theta_{\mathrm{sat}}$), the matric potential is close to zero and the soil water is under little or no tension. As the soil dries, the matric potential becomes increasingly negative, reflecting stronger capillary and adsorptive forces that hold water within smaller pores. Following the approach from Lawrence and Slater (2008), both $B_{(\mathrm{lwt})}$ and $\Psi_{\mathrm{sat,(lwt)}}$ are adjusted based on the soil's fraction of organic material using a weighted combination approach:

$$B_{(\mathrm{lwt})} = (1 - f_{\mathrm{sc,(lwt)}}) \cdot B_{\mathrm{min}} + f_{\mathrm{sc,(lwt)}} \cdot B_{\mathrm{sc}} \tag{16}$$

and

$$\Psi_{\mathrm{sat,(lwt)}} = (1 - f_{\mathrm{sc,(lwt)}}) \cdot \Psi_{\mathrm{min}} + f_{\mathrm{sc,(lwt)}} \cdot \Psi_{\mathrm{sc}}, \tag{17}$$

where $f_{\mathrm{sc,(lwt)}}$ is the fraction of organic material in this layer and B_{min} is the Clapp – Hornberger exponent for mineral soils (Table 1) and $B_{\mathrm{sc}} = 2.7$ for organic soils respectively Ψ_{min} the saturated matric potential for mineral soils and $\Psi_{\mathrm{sc}} = 10.3$ for organic soils (parameters for mineral soils are given in Table 1).

Within the soil bucket, the equilibrium state between the water table and the layers above is reached when the water entering the soil layer equals the water leaving it. The adjustment of the water table reflects the balance of water fluxes between the saturated zone and the unsaturated zone.

q_{recharge} determines from the hydraulic properties (Eq.¨?? if the water table rises or falls. z_Δ is initially set to the maximum soil depth and gradually reaches equilibrium during the spin-up simulation. This adjustment is based on changes in saturated zone storage. From the balance of the recharge rate (q_{recharge}) and drainage (q_{drain} or q_{perched} for partly frozen soils) the water table can be adjusted using the following equation:

$$\Delta z_\Delta = \frac{q_{\mathrm{recharge}} - q_{\mathrm{drain}}}{S_y}, \tag{18}$$

https://doi.org/10.5194/egusphere-2025-6210
Preprint. Discussion started: 22 January 2026

where S_y is the specific yield ranging between 0 an 1. It depends on the water table location and saturated soil properties:

$$S_y = \theta_{\mathrm{sat,(lwt)}} \left(1 - \left(1 + \frac{z_\Delta}{\Psi_{\mathrm{sat,(lwt)}}} \right)^{\frac{-1}{B_{\mathrm{(lwt)}}}} \right). \tag{19}$$

The stand-specific aquifer (W_a in mm) represents a vertically and spatially constrained water pool that is associated with individual stands within a grid cell. Its volume is limited to a maximum of 5000 l and is updated by the balance of q_recharge and q_drain if the water table is below the calculated soil column W_a:

$$W_\mathrm{a} = q_\mathrm{recharge} - q_\mathrm{drain}. \tag{20}$$

The W_a is stand specific and becomes hydraulically active and declines only when the water table falls below the maximum soil depth or the maximum storage is not reached, allowing the compartment to store additional water or release it through drainage. For the ground water dynamics an additional pool is introduced as described in section 2.2.4

2.2.4 Groundwater Pool Representation and Baseflow Recession Approach

A spatially explicit groundwater storage compartment was implemented for each grid cell to account for subsurface water dynamics. The groundwater pool is recharged by two components: (i) the percolation flux, defined as the downward drainage from the bottom soil layer, and (ii) the lateral runoff generated in the lowest saturated soil layer, representing subsurface flow contributing to groundwater recharge.

To simulate the temporal evolution of groundwater discharge, we apply a baseflow-recession approach (Beck et al., 2013). The dimensionless baseflow recession coefficient ($k_\mathrm{bf} \in [0,1]$) characterises the rate at which baseflow declines (Fig. A1). The specific formulation used here was developed in the ERMITAGE project (ERMITAGE project report (2013)) and is defined separately for each grid cell to account for spatial heterogeneity in hydrogeological properties such as aquifer transmissivity, soil texture and topographic gradient. High values of k_bf denote fast-draining soils or shallow aquifers, leading to rapid groundwater release, whereas low values represent deep or low-conductivity aquifers with slow recession and more sustained baseflow contributions. The release of groundwater to streamflow (baseflow) is described by a first-order linear recession function:

$$Q_\mathrm{bf}(t) = k_\mathrm{bf} \cdot GW(t), \tag{21}$$

where $Q_\mathrm{bf}(t)$ denotes the baseflow at time t, $GW(t)$ is the current groundwater storage.

The residual groundwater storage after baseflow release is retained in the groundwater compartment and contributes to subsequent discharge events, thereby introducing a memory effect in the hydrological system. This pa-

https://doi.org/10.5194/egusphere-2025-6210
Preprint. Discussion started: 22 January 2026

rameterization ensures both spatial differentiation and temporal delay in the subsurface runoff component, improving the realism of long-term streamflow simulations.

In cells with irrigated agriculture the groundwater storage pool also serves as an additional source for irrigation that is accessed only when surface water availability is insufficient to meet irrigation demand.

2.2.5 Stand-specific slope calculation

As the slope has an enormous importance for the infiltration and the runoff formation, but there is no information about the exact location of different stands within the grid cell, we distinguish only the mean slope for the wetland (β_{wet}) and for the upland area (β_{up}), respectively. To derive stand-specific slopes for wetlands and uplands, we therefore make a simple statistical assumption about the subgrid distribution of slope. Within each grid cell, the subgrid slope m is treated as a random variable which is assumed to follow a negative exponential probability distribution with cumulative distribution function (CDF)

$$F(m) = 1 - \exp(-\lambda m). \tag{22}$$

The rate parameter λ is chosen such that the mean of this distribution equals the DEM-derived grid-cell mean slope (β_{mean})

$$\mathbb{E}[m] = \frac{1}{\lambda} = \beta_{\text{mean}}\,. \tag{23}$$

where $\mathbb{E}[m]$ denotes the expectation (statistical mean) of m. After computing the wetland area fraction (A_{wet}) of the grid cell (see section 2.1), we determine a threshold slope $m_{\text{w,max}}$ such that $F(m_{w,max}) = A_{\text{wet}}$, assuming that the fraction of the cell with $m \leq m_{\text{w,max}}$ is equal to the wetland area fraction. Using the inverse CDF of the exponential distribution this yields

$$m_{\text{w,max}} = -\frac{1}{\lambda}\ln(1 - A_{\text{wet}}), \tag{24}$$

which is then constrained to the range $[m_{\text{min}}, m_{\text{max}}]$ of the grid cell. Slopes between m_{min} and $m_{\text{w,max}}$ are assigned to the wetland stand, and slopes between $m_{\text{up,min}}$ and m_{max} to the upland (natural or agricultural) stand. The mean slope of the wetland part is obtained from the truncated exponential distribution over $[m_{\text{min}}, m_{\text{w,max}}]$ as

$$\beta_{\text{wet}} = \frac{\int_{m_{\text{min}}}^{m_{\text{w,max}}} m\,\lambda e^{-\lambda m}\,dm}{\int_{m_{\text{min}}}^{m_{\text{w,max}}} \lambda e^{-\lambda m}\,dm}, \tag{25}$$

https://doi.org/10.5194/egusphere-2025-6210
Preprint. Discussion started: 22 January 2026

and is additionally constrained not to exceed β_{mean}. In the code these integrals are evaluated analytically using the antiderivative $-\exp(-\lambda m)\,(m+1/\lambda)$. Analogously, the upland mean slope β_{up} is computed as the conditional mean of the same exponential distribution over $[m_{\mathrm{w,max}}, m_{\mathrm{max}}]$ (see Fig. 1). The DEM-derived minimum and maximum slopes of the cell are denoted m_{min} and m_{max}. All non-rice agricultural stands are assigned the upland mean slope, whereas rice paddies are assumed to be levelled fields and therefore receive a slope of exactly zero.

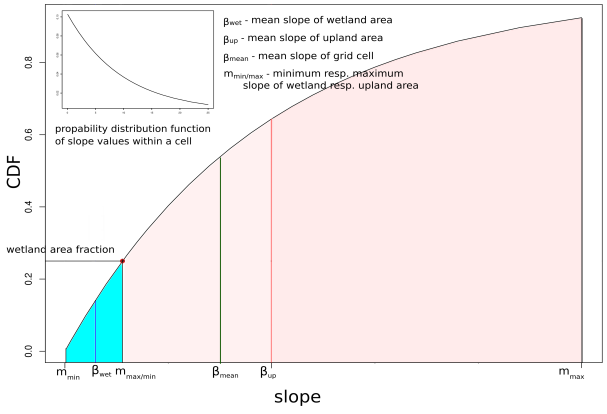

Figure 1. Determination of the slope values of wetland and upland stands depending on the fraction of the wetland area within a grid cell

2.3 Methane cycle

CH_4 dynamics within the terrestrial biosphere arise from both natural biogeochemical cycles and anthropogenic influences. Natural CH_4 emissions are predominantly driven by anaerobic microbial methanogenesis in O_2-deprived environments such as wetlands, peatlands, and rice paddies, where the decomposition of organic matter under anoxic conditions facilitates CH_4 production. Anthropogenic processes—such as those associated with intensive livestock farming, rice cultivation, fossil fuel extraction, and land-use modifications—contribute additional CH_4 through altered substrate availability and ecosystem disruption. Within LPJmL 6.0, soil CH_4 dynamics are resolved at sub-daily time steps that simulate the CH_4 pool by accounting for concurrent production and oxidation (see Fig. 2). An adaptive sub-stepping scheme refines the time step when local CH_4–O_2 concentration gradients become steep, ensuring numerical stability and mass conservation. The CH_4 flux to the atmosphere is computed as the sum of ebullition, molecular diffusion, and plant-mediated transport. The magnitude of each pathway responds to soil moisture (saturation and air-filled porosity), substrate availability (labile carbon), and the soil redox state (oxygen availability), which together regulate both production and oxidation rates.

https://doi.org/10.5194/egusphere-2025-6210
Preprint. Discussion started: 22 January 2026

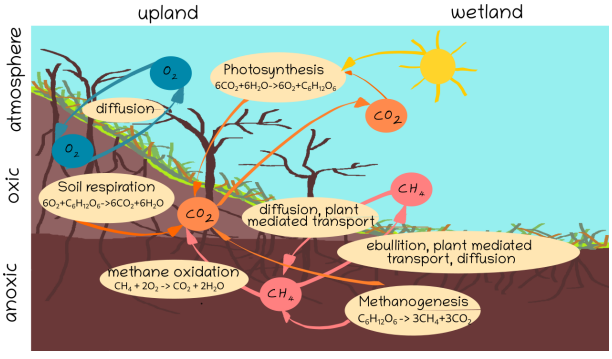

Figure 2. Newly added or modified soil processes in the LPJmL6 model. CO_2 diffusion is assumed to be instantaneous as in earlier versions of LPJmL (Schaphoff et al., 2018) and there is no interaction of CO_2 with the soil during the diffusion process, whereas the diffusion processes of oxygen and CH_4 are explicitly modeled because the time and position in the soil column is important for the CH_4 dynamics.

2.3.1 Balance of Methane and Oxygen Concentrations in Soils

The evolution of the CH_4 concentration in the soil is characterized by the diffusive transport of CH_4 through the soil column (first part of the equation) and the production of CH_4 (methanogenesis (R_{prod})) and losses through CH_4 oxidation above the water saturated layer if enough oxygen is available (R_{oxic}), the de-gassing through forming of bubbles in water filled pores (ebullition (Q_{ebull})), and the plant mediated transport ($Q_{\text{plant,CH}_4}$) by vascular plants through their aerenchyma:

$$\begin{aligned}\epsilon_{\text{CH}_4}\frac{\partial C_{\text{CH}_4}(z,t)}{\partial t} = {} & \frac{\partial}{\partial z}\left[D_{\text{CH}_4}(z)\frac{\partial C_{\text{CH}_4}(z,t)}{\partial z}\right] \\ & - Q^{\text{out}}_{\text{ebull}}(z,t) + Q^{\text{in}}_{\text{ebull}}(z,t) - Q_{\text{plant,CH}_4}(z,t) \\ & + R_{\text{prod}}(z,t) - R_{\text{oxic}}(z,t).\end{aligned} \tag{26}$$

The O_2 concentration is calculated analogously to the CH_4 concentration equation including the O_2 consuming processes of oxic decomposition of soil organic matter (R_{CO_2}),the plant mediated transport ($Q_{\text{plant,O}_2}$), nitrification of NH_4^+ to NO_3^- ($R_{\text{NO}_3^-}$), and aerobic root respiration (R_{root}):

$$\begin{aligned}\epsilon_{\text{O}_2}(z)\frac{\partial C_{\text{O}_2}(z,t)}{\partial t} = {} & \frac{\partial}{\partial z}\left[D_{\text{O}_2}(z)\frac{\partial C_{\text{O}_2}(z,t)}{\partial z}\right] - Q_{\text{plant,O}_2}(z,t) \\ & - \frac{W_{\text{O}_2}}{W_{\text{C}}}R_{\text{CO}_2}(z,t) - 2\frac{W_{\text{O}_2}}{W_{\text{CH}_4}}R_{\text{oxic}}(z,t) \\ & - 2\frac{W_{\text{O}_2}}{W_{\text{N}}}R_{\text{NO}_3^-}(z,t) - \frac{W_{\text{O}_2}}{W_{\text{C}}}R_{\text{root}}(z,t).\end{aligned} \tag{27}$$

https://doi.org/10.5194/egusphere-2025-6210
Preprint. Discussion started: 22 January 2026

where ϵ_{O_2} resp. ϵ_{CH_4} are the O_2 and CH_4 porosities, that convert concentration per soil volume to the gas concentration per air volume and are calculated as

$$\epsilon_{O_2} = v + \phi \cdot \theta_{sat} \cdot B_{O_2}, \quad \epsilon_{CH_4} = v + \phi \cdot \theta_{sat} \cdot B_{CH_4}, \tag{28}$$

where ϕ is the volumetric soil water content expressed per unit pore volume (mm^3 of water / mm^{-3} of soil porous volume; here θ_{sat} is used as an equivalent measure of the pore-volume fraction), and v is the soil air content (m^3 air per m^3 soil). W_C, W_{O_2}, and W_{CH_4} are the molar masses of Carbon ($12\,g\,mol^{-1}$), O_2 ($32\,g\,mol^{-1}$), and CH_4 ($16\,g\,mol^{-1}$), respectively. The Bunsen coefficients of O_2 (B_{O_2}) and CH_4 (B_{CH_4}) describe the solubility of these gases in water as a function of temperature. Due to the decreasing capacity of water to dissolve gases with rising temperature, this dependence is commonly expressed using exponential decay functions. Following Yamamoto et al. (1976) and Wiesenburg and Guinasso Jr (1979), we apply the following empirical relationships:

$$B_{O_2} = 0.0647 \cdot e^{-0.0257 \cdot T_{soil}}, \quad B_{CH_4} = 0.0523 \cdot e^{-0.0236 \cdot T_{soil}}. \tag{29}$$

The net CH_4 flux to the atmosphere, F_{atm}, represents the total upward CH_4 transfer from the soil to the atmosphere. It is considered positive when the soil acts as a net CH_4 source and negative when it acts as a net sink. This flux is composed of three contributing terms

$$F_{atm}(t) = \left(-D_{CH_4}(z) \frac{\partial C_{CH_4}(z,t)}{\partial z} \right)_{z=0} + Q^{out}_{ebull}(0,t) + F_{plant}(t), \tag{30}$$

where the diffusive flux at the soil-atmosphere interface, $-D_{CH_4}(z)\frac{\partial C_{CH_4}(z,t)}{\partial z}$, and the ebullition flux, $Q^{out}_{ebull}(z=0,t)$, escape directly to the atmosphere. Note that ebullition contributes directly to the atmospheric flux only from the surface layer ($z=0$), as ebullition from deeper layers is transferred to the layer above instead of escaping directly (see section 2.3.5). The third term, $F_{plant}(t)$, represents the flux of CH_4 transported through plant tissues (see section 2.3.6) , particularly aerenchyma structures, which provide a low-resistance conduit for CH_4 transfer from anaerobic soil layers directly to the atmosphere, bypassing diffusion and ebullition pathways.

2.3.2 Soil organic matter decomposition into CO_2 and CH_4

Oxic decomposition of organic carbon follows the principles described by Schaphoff et al. (2018). The anoxic decomposition model is adapted from Khvorostyanov et al. (2008). Aerobic conditions promote the generation of CO_2 in all soil carbon pools and anaerobic conditions lead to CH_4 production. The soil carbon pools consist of an intermediate and a slow pool with turnover rates for the oxic decomposition of 0.03 and 0.001 respectively at 10°C and a fast so-called active pool with a turnover rate of 0.3 (Schaphoff et al., 2018). For realistic decomposition dynamics, Schaphoff

https://doi.org/10.5194/egusphere-2025-6210
Preprint. Discussion started: 22 January 2026

et al. (2013) introduced a vertical soil distribution (Jobbagy and Jackson, 2000) which improved the simulation of the carbon, which can be released by permafrost thawing (see also Schaphoff et al. (2013)). Decomposition follows first order kinetics:

$$\frac{\partial C(z,t)}{\partial t} = R_{CO_2}(z,t) - R_{prod}(z,t), \tag{31}$$

where oxic (R_{CO_2}) and anoxic decomposition(R_{prod}) is reciprocally exclusive.

Soil respiration – oxic decomposition

Oxic decomposition is computed as

$$R_{\mathrm{CO_2}}(z,t) = \min\left[k_1(z,t)\cdot \mathrm{C}(z,t), \frac{\partial \mathrm{C_{max}}(z,t)}{\partial t}\right] \tag{32}$$

where C is the carbon pool size at time t and soil depth z, k_1 is the daily oxic decomposition rate, and ∂C_{max} is the mass of carbon corresponding to O_2 which is available for oxic decomposition:

$$\frac{\partial \mathrm{C_{max}}(z,t)}{\partial t} = \mathrm{O_2}(z,t)\cdot \frac{W_\mathrm{C}}{W_{\mathrm{O_2}}} \tag{33}$$

$O_2(z)$ is the mass of molecular soil O_2 at depth z. The oxic decomposition rate is expressed as:

$$k_1(z,t) = k\cdot g(T_{\mathrm{soil}}(z,t))\cdot f\left(\phi(z)\right). \tag{34}$$

k_1 incorporates the rate constant (k) that represents the reciprocal of the mean residence time τ for the litter components, as described by Schaphoff et al. (2018) for the litter components. Additionally, k_1 is influenced by the temperature dependency function $g\left(T_{\mathrm{soil}}(z,t)\right)$, and the soil moisture function $f(\phi_z)$ as outlined in Schaphoff et al. (2018) related to the non–frozen water. The temperature dependence function is based on an Arrhenius relationship as described in Schaphoff et al. (2018)

$$g\left(T_{\mathrm{soil}}(z,t)\right) = \exp\left[308.56\cdot\left(\frac{1}{56.02} - \frac{1}{T_{\mathrm{soil}}(z,t)+46.02}\right)\right], \tag{35}$$

where T_{soil} is the soil temperature in degree Celsius. The soil moisture function has its maximum around field capacity of the soil and is given by

$$f(\phi(z)) = 0.0402 - 5.005\cdot\phi(z)^3 + 4.269\cdot\phi(z)^2 + 0.719\cdot\phi(z).$$

https://doi.org/10.5194/egusphere-2025-6210
Preprint. Discussion started: 22 January 2026

Methanogenesis – anoxic decomposition

The anoxic decomposition (R_{prod}) is calculated as follows:

$$R_{\text{prod}}(z,t) = k_2(z,t) \cdot \text{C}(z,t). \tag{36}$$

The methanogenesis rate (k_2) is expressed as

$$k_2(z,t) = k \cdot r_k \cdot \exp\left(\frac{-C_{\text{O}_2}(z,t)}{O_2^*}\right) \cdot g(T_{\text{soil}}(z,t)). \tag{37}$$

$C_{\text{O}_2(z,t)}$ is the O_2 concentration at depth z, while $O_2{}^*$ represents a threshold O_2 concentration of $10\,\text{g}\,\text{m}^{-3}$. As demonstrated by Duval and Goodwin (2000) methanogenesis is significantly suppressed by higher O_2 concentrations. r_k is an empirical parameter reflecting the reduced methanogenesis rate under anoxic conditions, which is considerably slower than oxic decomposition and is set to 0.1 for the fast soil carbon pool and 0.5 for the fast decomposing litter pool. Components of the carbon pool, such as lignin, degrade much more slowly in anoxic environments due to their recalcitrant structure and resistance to microbial breakdown, further limiting methanogenesis. The decomposition rate under anoxic conditions is 4–10 times lower than under oxic conditions, with reported rates ranging from 0.02 to 1.44 mg CH_4 g^{-1} over 500 days (Lee et al., 2012). This corresponds to a decomposition rate between 1.46×10^{-5} and 0.00105. Methanogenesis rate k_2 has the same temperature dependence $g\,(T_{\text{soil}}(z,t))$ and rate constant (k) as the oxic decomposition.

2.3.3 Methane oxidation (R_{oxic})

The representation of the CH_4 oxidation (R_{oxic}) follows the approach by Walter and Heimann (2000). R_{oxic} occurs above the saturated soil layer, where enough O_2 is available.

$$R_{\text{oxic}}(z,t) = \min\left[\frac{V_{\max} \cdot \text{W}_{\text{CH}_4} \cdot C_{\text{CH}_4}(z,t)}{K_{\text{m}} \cdot \text{W}_{\text{CH}_4} + C_{\text{CH}_4}(z,t)} \cdot g\,(T_{\text{soil}}(z,t)), C_{\text{O}_2}(z,t) \cdot \frac{\text{W}_{\text{CH}_4}}{2\text{W}_{\text{O}_2}} \cdot \text{O}_{2,\text{frac}}\right], \tag{38}$$

where K_m and $V_{\max}$ are the Michaelis-Menten coefficients. These are defined in the model for $K_m = 5\mu\text{M}$ and $V_{\max} = 20\,\mu\text{M}\,\text{h}^{-1}$(Walter and Heimann, 2000). C_{CH_4} is the CH_4 concentration at time t and depth z in $\text{g}\,\text{m}^{-3}$. g(T_{soil})is the temperature response function given in Eq. 35. $V_{\max}$ and K_m need to be multiplied by the molecular mass of CH_4. O_2 consumption is limited by $\text{O}_{2,\text{frac}} = 0.95$, accounting for O_2 use for oxidation of reduced compounds, where 5% is assumed (Conrad, 1996; Xu et al., 2010; Saunois et al., 2020). O_2 consumption from aerobic microbial respiration, plant root respiration. nitrification and CH_4 oxidation is taken into account by reducing the O_2 content of the respective layer.

https://doi.org/10.5194/egusphere-2025-6210
Preprint. Discussion started: 22 January 2026

For the temperature dependency of CH_4 oxidation a Q_{10} relationship is used

$$g\left(T_{\text{soil}}(z,t)\right) = Q_{10}^{\frac{T_{\text{soil}}(z,t)-T_{\text{soil,mean}}(z)}{10}} \tag{39}$$

where $T_{\text{soil,mean}}$ is the annual mean soil temperature and the Q_{10} is set to 1.8.

2.3.4 Diffusion of Methane from soil (F_{diff})

CH_4 diffusion, which describes the movement of gas from higher to lower concentrations between layers and the air, is governed by Fick's law:

$$F_{\text{diff}}(z,t) = D_{CH_4}(z) \cdot \frac{\partial C_{CH_4}}{\partial x}(z,t), \tag{40}$$

where $D_{CH_4}(z)$ is the diffusivity at depth z and $C_{CH_4}(z,t)$ is the CH_4 concentration at time t and depth z. D_{CH_4} is calculated depending on soil water conditions:

$$D_{CH_4} = (D_{\text{air}_{CH_4}} \cdot v + D_{\text{water}_{CH_4}} \cdot w \cdot \theta_{\text{sat}} \cdot B_{CH_4}) \cdot \eta \tag{41}$$

where $D_{\text{air}_{CH_4}}$ is the diffusivity of air (1.82e-5 $m^2 s^{-1}$) and $D_{\text{water}_{CH_4}}$ the diffusivity of water (1.6e-9 $m^2 s^{-1}$ Khvorostyanov et al. (2008)). B_{CH_4} is the Bunsen coefficient for CH_4 (see Eq. 29) and $\eta = 2/3$ denotes the soil tortuosity. O_2 diffusion is calculated analogous to Eqs. 40 and 41. Initial conditions of all soil layers are:

$$C_{CH_4} = 1.207\,\text{g}\,\text{m}^{-3},$$
$$C_{O_2} = 266\,\text{g}\,\text{m}^{-3}$$

The lower boundary for both CH_4 and O_2 conditions are:

$$\frac{\partial C_{CH_4}(z = \text{soildepth})}{\partial z} = \frac{\partial O_2(z = \text{soildepth})}{\partial z} = 0 \tag{42}$$

and the upper boundary conditions are:

$$C(z=0) = \frac{p_s}{R \cdot T_{\text{air}}} \cdot \text{AC}_{\text{gas}} \cdot W, \tag{43}$$

where p_s is the atmospheric surface pressure (101000 Pa), T_{air} is the air temperature (in K) , AC_{gas} is the atmospheric content (0.209 for O_2, transient over time for CH_4), W is the molar mass of O_2 and CH_4, respectively and R is the universal gas constant (8.314 $\text{J}\,\text{mol}^{-1}\,\text{K}^{-1}$).

https://doi.org/10.5194/egusphere-2025-6210
Preprint. Discussion started: 22 January 2026

Numerical solutions to the CH_4 and O_2 diffusion problems are obtained using the finite difference method for the heat diffusion problem described by Alexiades and Solomon (1993, Sec. 4.1). For time stepping the forward Euler, Crank-Nicolson and backward Euler methods were tested. The backward Euler scheme was the only method that provided sufficient stability to enable long enough time steps required under the given computational constraints and has therefore been adopted as the default time-integration scheme in LPJmL6.

2.3.5 Methane ebullition (Q_{ebull})

CH_4 ebullition is the process by which CH_4 gas produced in anaerobic soil environments escapes into the atmosphere through gas bubbles. This occurs when the concentration of dissolved CH_4 in soil porewater exceeds its solubility threshold, causing bubble nucleation and release. The process is modulated by factors such as CH_4 concentration, soil moisture, and vegetation cover, which influence both the formation and migration of gas bubbles. The change in CH_4 concentration in a soil layer over time due to ebullition is governed by a balance between CH_4 loss via ebullition and CH_4 flux received from the layer below.

Ebullition is active only when the local CH_4 concentration exceeds a critical threshold required for bubble formation (Walter and Heimann, 2000), and the outgoing ebullition flux is then calculated as

$$Q_{\mathrm{ebull}}^{\mathrm{out}}(z,t) = k_e \cdot \max((C_{\mathrm{CH_4}}(z,t) - C_{\mathrm{thresh}}), 0), \tag{44}$$

where k_e is the ebullition efficiency constant controlling the rate of CH_4 release, which typically ranges between 0.1 to 1 per day, and C_{thresh} is the threshold CH_4 concentration for bubble formation. In this study we set $k_e = 1$. The functional form of the threshold concentration is given by

$$C_{\mathrm{thresh}} = C_{\mathrm{min}} \cdot \left(1 + 1 - \sum_{\mathrm{pft}=1}^{n_{\mathrm{PFT}}} (\alpha_{\mathrm{pft}}^{\mathrm{e}} \cdot \mathrm{FPC}_{\mathrm{pft}})\right), \tag{45}$$

Experimental studies have shown that the presence of vegetation can substantially suppress CH_4 ebullition due to competition with plant-mediated transport and structural alterations to sediment or soil (Deshmukh et al., 2020). Therefore, to represent the vegetation-dependent reduction in ebullition flux, we introduce plant functional type (PFT)-specific suppression (α^e) factors in the model (see Tables 2 and 3 for parameter values). These account for the observed differences in ebullition across vegetated and non-vegetated systems, as supported by field measurements. FPC is the fractional plant cover of the PFT, which influences bubble formation by altering gas exchange dynamics. C_{min} is the minimum CH_4 concentration required for bubble formation under standard conditions and has been observed to range between 500 and 1000 $\cdot 10^{-6}$M (Khvorostyanov et al., 2008) which corresponds to 0.008 to 0.016 g m^{-3}. We use 0.012 g m^{-3} in LPJmL6. Eq. 44 ensures that ebullition only occurs when the gas pressure exceeds the critical pressure threshold.

https://doi.org/10.5194/egusphere-2025-6210
Preprint. Discussion started: 22 January 2026

The outgoing ebullition flux is transferred upwards and is added to the incoming ebullition flux $Q^{in}_{ebull}(z,t)$ in a layer above in case of $z < 0$, or to the atmosphere in case of $z = 0$. At the shallowest soil depth, there is no overlying material to impede the upward migration of gas bubbles. Therefore, the ebullition flux originating from this depth contributes directly to the CH_4 flux emitted to the atmosphere.

At deeper soil depths, the fate of CH_4 released via ebullition depends on the moisture content of the overlying soil column. If the overlying layer is not saturated ($\theta < 0.9$), the bubbles are trapped and remain in the overlying layer, preventing direct transfer. However, if the overlying layer is water-saturated (soil moisture > 0.9), bubbles migrate further upward and are transferred to the next layer above.

This recursive upward propagation continues through the saturated soil profile until an unsaturated soil layer is found or the surface is reached. This mechanism determines whether CH_4 from deeper soil zones contributes to atmospheric emissions or remains retained within the subsurface environment.

2.3.6 Plant-Mediated Transport (Q_{plant})

Certain vascular plants possess aerenchyma, a specialized tissue forming interconnected air-filled channels within their stems, leaves, and roots. This tissue facilitates the movement of O_2 and CH_4 between the plant and its environment, playing a crucial role in gas exchange, particularly in waterlogged or anaerobic soils. O_2 is transported from the atmosphere through the stems and leaves into the roots, supporting root respiration. Conversely, CH_4 produced in anaerobic soils can diffuse into the aerenchyma through the roots and be transported upward through the plant, being released into the atmosphere, bypassing the oxidizing zones in the soil. We hypothesize that this gas exchange via aerenchyma is more prominent in grasses compared to trees, as aerenchyma is predominantly observed in herbaceous plants and is largely absent in woody species (Takahashi et al., 2014; Colmer, 2003). To quantify these processes, we adopt the approach outlined by Wania et al. (2010) which shows that gas diffusion through aerenchyma (F_{plant}) depends on both the cross-sectional area of plant tillers available for gas transport (A_{tiller}, in m^2) and the volumetric soil liquid water content (θ_{liq}, in m^3):

$$F_{plant}(t) = \int_{rootingdepth}^{soilsurface} Q_{plant}(z,t) \cdot dz, \tag{46}$$

where

$$Q_{plant}(z,t) = (C_{gas}(z,t) - C_{gas_{air}}) \cdot \exp\left(\frac{-k_{gas} \cdot A_{tiller}}{\theta_{liq}(z,t)}\right). \tag{47}$$

This equation is applied to both O_2 and CH_4 in the model, reflecting the bidirectional transport of these gases. A_{tiller} is defined as:

$$A_{tiller} = \max\left(0.001, \pi \cdot r^2_{tiller} \cdot N_{tiller} \cdot \phi_{tiller}\right), \tag{48}$$

https://doi.org/10.5194/egusphere-2025-6210
Preprint. Discussion started: 22 January 2026

where r_{tiller} is the radius of an individual plant tiller defined to be $r_{\text{tiller}} = 0.0345$ m (Nascimento et al., 2021). The variable ϕ_{tiller} is the porosity of the tiller structure, expressed as a dimensionless fraction ($\phi_{\text{tiller}} = 0.7$). The use of the max function ensures that A_{tiller} maintains a minimum value of $0.001\,\text{m}^2$, preventing numerical instability when the calculated tiller area becomes very small. N_{tiller} represents the tiller fraction, which depends on plant biomass and root distribution within the soil layer:

$$N_{\text{tiller}} = \text{C}_{leaf} \cdot (\gamma / W_{tiller}) \cdot F_{root(l)}, \tag{49}$$

where C_{leaf} is the leaf carbon per square meter for PFTs that are able to form aerenchyma and γ is the phenology status of the PFT. $W_{tiller} = 0.22$ g (Wania et al., 2010) is the weight of the tillers and $F_{root(l)}$ is the fraction of the root in the respective layer.

The gas exchange coefficient, (k_{gas} in $\text{m}\,\text{d}^{-1}$), represents the piston velocity between the water and the atmosphere. Following Wania et al. (2010), (k_{gas}) is obtained by scaling a reference transfer velocity for a Schmidt number (Sc) of 600, ($k_{600} = 2.07\,m\,d^{-1}$) with the actual Schmidt number of the respective gas:

$$k_{\text{gas}} = k_{600} \cdot \left(\frac{Sc_{\text{gas}}}{600} \right)^{n_p}, \tag{50}$$

where n_p is the Schmidt-number exponent, here set to -0.5. Sc can be calculated specifically for O_2 and CH_4:

$$Sc_{\text{CH}_4} = 1898 - 110.1 \cdot \text{T}_{\text{air}} + 2.834 \cdot {\text{T}_{\text{air}}}^2 - 0.02791 \cdot {\text{T}_{\text{air}}}^3 \tag{51}$$

and

$$Sc_{\text{O}_2} = 1800.6 - 120.1 \cdot \text{T}_{\text{air}} + 3.7818 \cdot {\text{T}_{\text{air}}}^2 - 0.047608 \cdot {\text{T}_{\text{air}}}^3 \tag{52}$$

In summary, CH_4 and O_2 fluxes are based on concentration gradients, gas transfer velocities, and tiller geometry, while accounting for soil moisture, porosity, and air content. These fluxes reflect the dynamic movement of gases between the soil and atmosphere, influenced by soil properties, plant structure, and environmental conditions.

2.3.7 Oxygen consumption by nitrification and root respiration

Dissolved oxygen in each soil layer is consumed by nitrification of ammonium and aerobic root respiration. Nitrification is represented by the overall reaction

$$\text{NH}_4^+ + 2\,\text{O}_2 \rightarrow \text{NO}_3^- + 2\text{H}^+ + \text{H}_2\text{O},$$

i.e. one mole of N nitrified requires two moles of O_2. For the nitrification rate $R_{\text{NO}_3^-}(z,t)$ (g N m^{-3} s^{-1}), the associated O_2 consumption is

https://doi.org/10.5194/egusphere-2025-6210
Preprint. Discussion started: 22 January 2026

$$S_{O_2}^{nitr}(z,t) = 2\,\frac{W_{O_2}}{W_N}\,R_{NO_3^-}(z,t), \tag{53}$$

where W_N is the molar mass of N (14 g mol^{-1}). In the numerical implementation $R_{NO_3}(z,t)$ corresponds to the depth-dependent analogue of the nitrification flux $F_{NO_3^-}$ limited by O_2, NH_4^+ availability, soil moisture, temperature and pH (see von Bloh et al. (2018)).

Aerobic root respiration represents the metabolic consumption of O_2 by living roots to sustain maintenance and growth. The model provides a depth-dependent root respiration rate $R_{root}(z,t)$ (g C m^{-3} s^{-1}), which is distributed over the soil profile according to the vertical root density. Because the O_2 balance is formulated in units of O_2 mass, this carbon–based respiration flux is converted into an equivalent O_2 sink $S_{O_2}^{root}$ using a constant mass-conversion factor, yielding

$$S_{O_2}^{root}(z,t) = \frac{W_{O_2}}{W_C}\,R_{root}(z,t). \tag{54}$$

2.4 Inundation feedback on vegetation

Inundation harms trees, grasses and crops that are not tolerant of water-saturated soils. These damages can cause (potentially lethal) productivity losses. The most important factor determining plant survival is the duration of inundation (Parolin and Wittmann, 2010). To account for the effect of inundation on vegetation we have introduced a feedback of inundation on gross primary production (GPP) and added three new PFTs which are tolerant to inundation: a tropical broadleaved evergreen flood-tolerant tree, a C3 graminoid herbaceous plant and sphagnum moss. The last two were already implemented in the LPJWhy model by Wania et al. (2009). The tropical tree is parameterized similarly to the default tropical broadleaved evergreen tree in previous LPJmL versions but with a parameterization tolerant of inundations.

Inundation areas are often not flooded constantly. To account for inundation stress we have introduced two new parameters as suggested by Wania et al. (2009). The inundation stress height (ist_m) defines at which water table depth a PFT experiences inundation stress and the inundation duration (idt_d) defines how long a PFT can endure inundation. The inundation-tolerant PFTs have a higher inundation stress height and endure longer inundation periods (Table 2). The stress factor (S_{inun}) is applied to GPP whenever the water table exceeds ist_m (GPP = GPP $\cdot\,(1 - S_{inun})$):

$$S_{inun} = \min\left(1,\ \max\left(0,\ \left[\frac{1}{1+\exp\left(-k\cdot(N_{inun} - idt_d)\right)} - 0.5\right]\times 2\right)\right), \tag{55}$$

where N_{inun} counts the number of days with inundation stress. Table 2 gives the parameter values of idt_d for the different PFTs, representing their tolerable inundation duration. Values from Wania et al. (2009) were adjusted, i.a.

https://doi.org/10.5194/egusphere-2025-6210
Preprint. Discussion started: 22 January 2026

Table 2. Parameters describing inundation stress of PFTs, negative values indicate inundation stress starting at water table heights ist_m below the surface. idt_d defines after how many days inundation stress occur. α^e gives the ebullition suppression factor. Abbreviation see Table A1

	ist_m in m	idt_d in days	α^e
TrBrEv	-0.1	20	0.7
TrBrEv*	0.5	80	0.7
TrBrDe	-0.3	20	0.7
TeNeEv	-0.25	15	0.7
TeBrEv	-0.25	15	0.7
TeBrDe	-0.2	30	0.5
BoNeEv	-0.3	15	0.4
BoBrDe	-0.25	20	0.6
BoNeDe	-0.2	20	0.4
TrHe	-0.1	20	0.3
TeHe	-0.1	25	0.3
PoHe	-0.1	15	0.3
C3gr*	0.2	55	0.3
Moss*	0.5	35	0.3

* flood-tolerant PFT.

because PFTs TrBrEv and PoHe are not present in the implementation of Wania et al. (2009). The parameters for crop functional types (CFTs) in Table 3 take into account that the different CFTs suffer differently from inundation (Kaur et al., 2020). The parameter k (0.2 in day^{-1}) controls how rapidly stress increases once the inundation duration exceeds the threshold, with larger values producing a steeper rise. When the inundation threshold (ist_m) is no longer exceeded, the duration counter decreases in accelerated daily steps (five per day), representing a faster recovery of the plants relative to the length of the preceding inundation period.

Additionally, inundation stress increases tree mortality, contributing an additional mortality component ($\text{mort}_{\text{inun}}$) that increases the overall tree mortality rate. This contribution is capped at a maximum increase (inun_{max}) of 10% relative to the potential mortality rate (mort_{max}):

$$\text{mort}_{\text{inun}} = \text{mort}_{\text{max}} \cdot (1 - \text{inun}_{\text{max}}^{S_{\text{inun}}}), \tag{56}$$

where mort_{max} represents the PFT-specific baseline mortality rate as described in Schaphoff et al. (2018).

https://doi.org/10.5194/egusphere-2025-6210
Preprint. Discussion started: 22 January 2026

Table 3. Parameters describing inundation stress of CFTs, negative values indicate inundation stress starting at water table heights ist_m below the surface. idt_d defines after how many days inundation stress occur. α^e gives the ebullition suppression factor. Abbreviation see Table A1

	ist_m in m	idt_d in days	α^e
TeCe	-0.2	20	0.7
Rice*	1.0	200	0.5
Maize	-0.2	20	0.7
TrCe	-0.2	25	0.7
Pulses	-0.3	15	0.7
TeRo	-0.2	15	0.7
TrRo	-0.2	15	0.7
Sunfl	-0.2	15	0.7
Soy	-0.1	20	0.7
GrNu	-0.3	10	0.7
Rape	-0.3	20	0.7
SuCa	-0.1	30	0.7

* flood-tolerant CFT

2.5 Land-use change and rice cultivation

To account for the actual land cover, the model had to be extended for land-use change on wetlands. Previous versions of LPJmL distinguish a rainfed and an irrigated stand on which rainfed and irrigated crop cultivation as well as the off season is simulated, respectively. Here we assume that rice cultivation takes place on wetland areas if natural wetlands are present in the respective grid cell. Therefore, a new wetland setaside stand is introduced from which cropland is sourced for rice cultivation upon sowing/transplanting. If not enough upland (dry) natural land is available in the cell to satisfy land use demand, wetland area can also be converted to managed grasslands and, as a last resort, to cropland for crops other than rice. Soil water on rice fields is filled up above field capacity through irrigation to simulate permanent inundation. There is no explicit simulation of drainage systems for non-rice cultivation on wetland areas. A land use overview scheme is given in the Supplement Fig. S1.

3 Modelling protocol

To demonstrate the performance of LPJmL6 to model the newly implemented process dynamics, it was initialized with a spin-up period of 4000 years, using repeated climatic data from 1901 to 1930 to simulate pre-industrial conditions and achieve dynamic equilibrium in vegetation structure and composition as well as in carbon and nitrogen pools, representing a hypothetical stable pre-industrial state. To account for historical land-use dynamics,

https://doi.org/10.5194/egusphere-2025-6210
Preprint. Discussion started: 22 January 2026

an additional 420 years of spin-up simulation were performed between the initial spin-up and the transient historical simulation, ensuring accurate representation of land-use history and its effects on biogeochemical pools and cycles. Following this, a transient simulation was conducted, covering the period 1901 to 2019.

4 Data used

4.1 Input data

LPJmL6 was here driven by GSWP3-W5E5 climate data (Lange et al., 2023). This dataset combines W5E5 v2.0 (Cucchi et al., 2020; Lange et al., 2021) for the period 1979–2019 with GSWP3 v1.09 (Kim, 2017) for the period 1901–1978. GSWP3 data have been bias-adjusted towards W5E5 to reduce discontinuities at the 1978/1979 transition (Mengel et al., 2021). Annual atmospheric CO_2 concentrations are taken from the TRENDY project (Friedlingstein et al., 2023). Annual atmospheric CH_4 concentrations are taken from the NOAA Global Monitoring Laboratory (NOAA Global Monitoring Laboratory, 2025). Land-use data are generated with the LandInG toolbox (Ostberg et al., 2023). LandInG integrates and harmonises a number of gridded source datasets such as cropland and pasture extent from HYDE v3.2.1 (Klein Goldewijk et al., 2017a), multiple-cropping suitability from GAEZ v3 (IIASA/FAO, 2012), and crop-specific harvested areas for the year 2000 (Monfreda et al., 2008), with census data at national scale from FAOSTAT (FAO, 2020b), AQUASTAT (FAO, 2020a) and MIRCA2000 (Portmann et al., 2010a, b) to derive gridded time series of crop-specific growing patterns (with a distinction of rain-fed and irrigated areas) and pasture areas. As fallow land is currently not supported as a separate land-use category by LPJmL, fallow land from LandInG is assigned to the "others" crop category in LPJmL. LandInG also integrates crop-specific fertilizer application patterns for the year 2000 (Mueller et al., 2012; Mueller, 2012) with national-scale fertilizer application trends (Hurtt et al., 2020) to derive gridded time series of crop-specific nitrogen fertilizer application rates. Manure application rates are based on Zhang et al. (2017); Zhang et al. (2017). Crop-specific growing periods are based on the GGCMI phase 3 crop calendar (Jägermeyr et al., 2021). Grazing management is simulated on prescribed pasture areas (see above), with livestock densities based on Heinke (2025). Soil texture and soil acidity (pH) inputs are based on HWSD v1.21 (FAO/IIASA/ISRIC/ISSCAS/JRC, 2012), which has been aggregated from the source resolution by selecting parameters representative of the most prevalent soil type in each LPJmL grid cell (Ostberg et al., 2023). River network topology is based on STN-30 (Vörösmarty et al., 2000). Prescribed lake surface areas are based on GLWD (Lehner and Döll, 2004). Dam and reservoir characteristics are based on GRanD (Lehner et al., 2011; Biemans et al., 2011). Water use for households, industry and livestock in each grid cell is taken from Flörke et al. (2013) (prioritized over irrigation; accounting for 201 km^3 in the year 2000). We use the ISLSCP II HYDRO1k elevation-derived products at 0.5°spatial resolution (Verdin et al., 2011), which provide, for each grid cell, statistics of the compound topographic index (CTI) including its mean, standard deviation and skewness; these moments are used to parameterise the gamma distribution of CTI in our wetland scheme (section 2.1). The ISLSCP II product is derived from the original 1–km HYDRO1k database (U.S. Geological Survey, 2007b). The slope values are taken

https://doi.org/10.5194/egusphere-2025-6210
Preprint. Discussion started: 22 January 2026

directly from the USGS fine-resolution 30-arc-second GTOPO30 slope product (U.S. Geological Survey, 2007a), from which we derive the mean, maximum and minimum slope of each 0.5°cell for the slope–dependent wetland parameterisation.

4.2 Validation data

A combination of geographically detailed data is used to evaluate the LPJmL6 model's ability to simulate wetland extent. Kaplan (2007) provides a global wetland map at 0.5 degree resolution, combining regional and global inventories, geomorphic and hydrological data, and satellite observations. It broadly defines wetlands, including permanently and seasonally inundated areas, and waterlogged soils. The Global Lakes and Wetlands Database (GLWD) by Lehner and Döll (2004) offers high-resolution (1 km) data on lakes, reservoirs, and wetlands, classifying water bodies by size, hydrology, and ecological features. While we use the GLWD lake area as an input to the model (section 4.1) we use the GLWD wetland extent for validating the simulated global dynamics of wetland extent. Gumbricht et al. (2017) present the SWAMP dataset, a high-resolution (231 m) map of tropical and subtropical wetlands, integrating geomorphic classification, hydrological modeling, and satellite imagery. Zhang et al. (2021) developed WAD2M, a dataset on monthly wetland extent for 2000—2018 at 25 km resolution (using the mean annual extent), focused on permanently vegetated wetlands by excluding permanent water bodies, coastal wetlands, and rice paddies.

Estimates of CH_4 emissions from rice cultivation were derived from a combination of empirical field data, synthesis studies, and global-scale inverse modeling frameworks, as follows. The resulting CH_4 emission values represent cumulative seasonal emissions (in $gCH_4\,m^{-2}$) from flooded rice systems, calculated by multiplying observed or reported mean daily CH_4 emission rates ($gCH_4\,m^{-2}\,day^{-1}$) with region-specific growing season lengths. This approach allows for spatially explicit interregional comparison of seasonal CH_4 release, facilitating benchmarking of biogeochemical models and identifying emission hotspots. A comprehensive synthesis by Wang et al. (2018) compiled over 600 site-years of CH_4 flux data collected from 1990 to 2014, encompassing diverse rice-growing environments and management regimes. Their dataset provided country-level mean emission rates and associated 95 % confidence intervals, reflecting spatial heterogeneity across sites. These values were further stratified by continent and climate zone to support global upscaling. Complementing this synthesis, Zhu and Li (2024) incorporated more recent CH_4 flux observations from East Asia, including multi-cropping systems and long-term experimental sites. Their dataset included some of the highest recorded emissions, particularly in southern China, and expanded the representativeness of regional variability. In South Asia, Gupta et al. (2021) reported empirical data on daily CH_4 fluxes from irrigated rice paddies in northern India under varying water and residue management practices, highlighting the mitigation potential of alternate wetting and drying regimes. Earlier field-based estimates provided by Wassmann et al. (2000) focused on major rice ecosystems in Southeast Asia, using controlled experiments and standardized chamber measurements under the IRRI-GTZ collaboration. Their regional emission ranges from the 1990s remain influential for emission factor development and baseline scenario assessment.

https://doi.org/10.5194/egusphere-2025-6210
Preprint. Discussion started: 22 January 2026

While these sources generally provide spatial uncertainty bounds, they do not fully capture interannual variability, which may be significant under shifting climate and agronomic conditions. To contextualize and constrain bottom-up estimates, we integrated global atmospheric inversion data from the CarbonTracker-CH_4 framework (NOAA Global Monitoring Laboratory, NOAA Global Monitoring Laboratory (n.d.); Bruhwiler et al. (2014)). This system assimilates atmospheric CH_4 concentrations from NOAA's global flask and in situ measurement network (NOAA Global Monitoring Laboratory, 2025) to infer regional and global emission patterns. Wetland and rice cultivation emissions were treated as distinct sectors, enabling partial attribution of seasonal CH_4 enhancements to rice-growing regions in Asia. Additional global source data and attribution uncertainty ranges were taken from the Global Methane Budget reports by Saunois et al. (2020, 2025), which combine bottom-up inventories, top-down atmospheric inversions, and process-based models. To analyze how CH_4 emissions vary with latitude across different datasets, the LPJmL6 model is compared with the WetCHARTs v1.0 dataset provided by Bloom et al. (2017a). WetCHARTs (Wetland and Climate CH_4 Intercomparison of Models) offers a global dataset of wetland CH_4 emissions at a 0.5°resolution, along with associated uncertainties. This dataset integrates multiple emission models, remote sensing data, and atmospheric observations to provide a comprehensive and harmonized view of CH_4 emissions from wetlands.

Monthly river discharge observations were used to evaluate monthly simulated river discharge at the basin scale. The observational compilation comprises 285 gauging stations with reported upstream drainage areas exceeding 10,000 km^2. The dataset was assembled by combining (i) pan-Arctic discharge records from R-ArcticNET (v4.0) (Lammers et al., 2001, 2016) and (ii) global monthly discharge records from the RivDIS database (v1.1) distributed by the ORNL DAAC (NASA Earthdata) (Vörösmarty et al., 1998), where the latter was restricted to stations belonging to the dataset's major basins.

We used eddy-covariance flux tower data to benchmark simulated fluxes of net ecosystem exchange (NEE) and evapotranspiration (ET),providing direct and continuous measurements of ecosystem–atmosphere exchanges of carbon dioxide and water vapor at the ecosystem scale. In this study, tower-derived NEE and ET were compared against the corresponding model outputs. While the evaluation allows for a direct assessment of the model's ability to reproduce observed flux dynamics, it is subject to several limitations. These include differences in spatial scale between the grid-based simulations and the footprint of the flux towers, potential mismatches in vegetation composition due to the model's dynamic PFT representation, and the use of large-scale meteorological forcing instead of site-specific weather observations.

To assess vegetation structure, we contrasted LPJmL6 PFT distributions with the ESA CCI–derived product of Harper et al. (2023), a 29-year (1992–2020) 300 m dataset that harmonizes land cover into fractional PFTs, enabling scale-aware, spatially explicit comparisons with model output (Harper et al., 2023).

For system-level context, we drew on the Global Carbon Budget (GCP, Friedlingstein et al., 2023), which synthesizes atmospheric CO_2 growth, ocean uptake, and land-sink estimates together with fossil and land-use emissions and reports an annual budget imbalance as an integrated constraint. We also applied the International Land Model Benchmarking framework (ILAMB), detailed at https://www.ilamb.org/, to place our results in a standardized

https://doi.org/10.5194/egusphere-2025-6210
Preprint. Discussion started: 22 January 2026

multi-metric context (bias, RMSE, seasonal phase/amplitude, spatial distribution) and to summarize performance with an overall score (see Collier et al., 2018 and ILAMB documentation).

5 Model evaluation

5.1 ILAMB comparison

As part of our evaluation process, we conducted an extensive benchmarking analysis using the ILAMB framework, [full report is available at Zenodo: https://doi.org/10.5281/zenodo.17877397]. The ILAMB project provides a standardized system for assessing the performance of land surface models against a variety of observational datasets. This framework is widely recognized for its ability to objectively evaluate model fidelity across multiple environmental and ecological variables, including carbon, water, and energy fluxes. For our analysis, we applied the ILAMB methodology to the LPJmL6 model in comparison to LPJmL5.10 shown for separate simulations with actual land use and for potential natural vegetation, producing comprehensive benchmarking outputs to compare its performance against observational data. This approach ensures a rigorous and transparent evaluation, highlighting both strengths and areas for improvement in LPJmL6's ability to simulate terrestrial ecosystem processes. The results of this benchmarking exercise serve as a valuable reference point for future model development and intercomparison efforts, contributing to the broader goal of improving Land Surface Model performance.

5.2 Wetland area and distribution

Wetland distribution simulated by LPJmL6 depend on the CTI of the cell and the simulated water table depth as described in section 2.1. In the comparison of simulated and observed wetland area we do not exclude grid cells with rice cultivation. Because rice is typically established on wet or formerly wet soils, an expansion of rice area can therefore appear as an increase in wetland area in our evaluation against simulations for natural vegetation (LPJmL6-PNV), even though these sites often represent wetlands that have been converted to cropland. The simulated wetland area is overall comparable to other independent estimates (Table 4), but systematic discrepancies between datasets are evident. SWAMP includes only the wetland area south of 39°N, which explains the absence of high-latitude wetlands in this dataset and its focus on tropical regions, particularly the Amazon (Gumbricht et al., 2017). In contrast, GLWD indicates by far the greatest extent north of 60°N, reflecting its strong emphasis on boreal and permafrost wetlands (Lehner and Döll, 2004). LPJmL6 produces a much lower extent in these regions, closer to the estimates by (Zhang et al., 2021), yet this underestimation of boreal wetlands compared to GLWD indicates that LPJmL6 does not translate permafrost-induced flooding into wetlands. Conversely, LPJmL6 is able to reproduce the strong tropical maximum in the Amazon region that dominates the SWAMP dataset.

The latitudinal distribution (Fig. 3) highlights these contrasting signals: GLWD exhibits a pronounced peak in the high northern latitudes, SWAMP primarily represents tropical wetlands, and LPJmL6 shows a more balanced

https://doi.org/10.5194/egusphere-2025-6210
Preprint. Discussion started: 22 January 2026

Table 4. Wetland area (in 10^6 km^2) according to different data products, compared to simulations with LPJmL6 (with land-use change) and LPJmL6-PNV (potential natural vegetation only).

	GLWD	SWAMP	Kaplan (2007)	Zhang et al. (2021)	LPJmL6	LPJmL6-PNV
Global	11.4	6.0	5.7	3.6	5.6	5.6
>60°N	2.3		1.1	0.1	0.2	0.2
>30°N - 60°N	4.8	0.7*	1.9	1.2	1.2	1.5
<30°N	4.3	5.3	2.7	2.3	4.2	3.9

* area only partly represented

distribution with clear tropical hotspots and additional mid-latitude wetlands in Eurasia. These differences also have direct implications for global methane budgets, as both tropical floodplains and high-latitude permafrost wetlands are recognized as key but highly uncertain contributors to natural CH_4 emissions (Saunois et al., 2020; Hugelius et al., 2020). The strong disagreement in global totals across models and observational datasets (ranging from 3.6 to 11.4 × 10^6 km^2) underlines the need for improved observational constraints and harmonized definitions of wetlands.

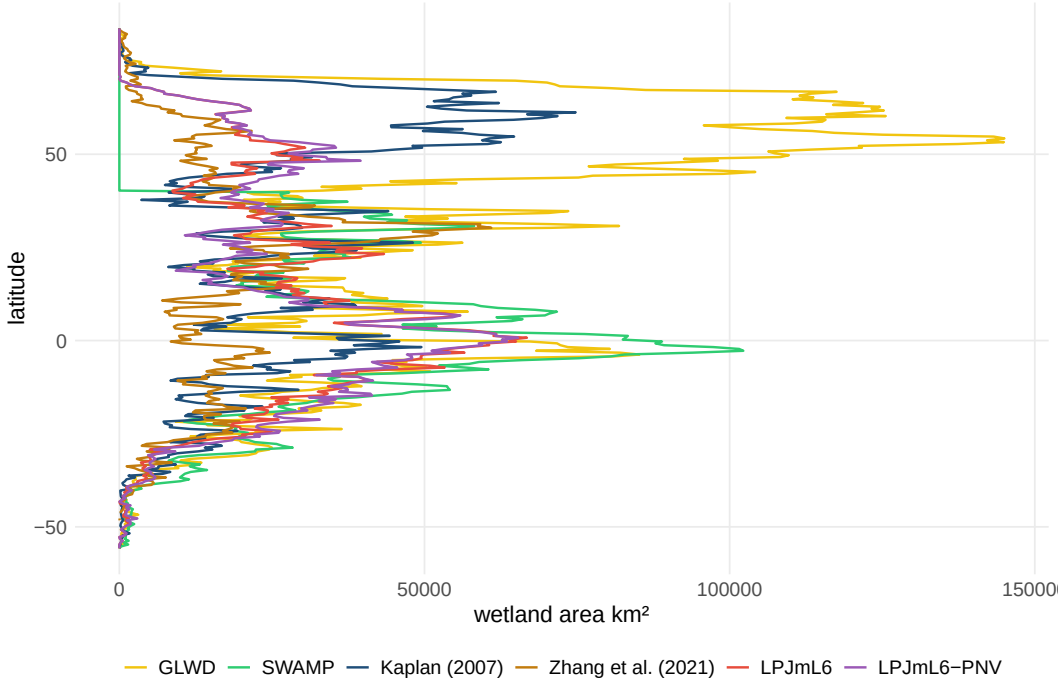

Figure 3. Latitudinal distribution of zonal wetland area from different data products and from LPJmL6 (with land-use change) and LPJmL6–PNV (potential natural vegetation). Wetland area is integrated along longitude for each half degree latitude band (km^2).

https://doi.org/10.5194/egusphere-2025-6210
Preprint. Discussion started: 22 January 2026

5.3 Methane budget

In this section, we confront the land CH_4 budget simulated by LPJmL6 with independent constraints on the global CH_4 budget. The global budget is determined by the balance between all surface sources and atmospheric sinks of CH_4 and is constrained by the observed atmospheric CH_4 burden, its temporal growth and estimates of the atmospheric CH_4 lifetime (Stevenson et al., 2020; Saunois et al., 2020; He et al., 2021; Saunois et al., 2025). These constraints define a range of total CH_4 emissions and, by subtraction of quantified source categories, a residual range attributable to net land sources.

LPJmL6 represents a subset of the global CH_4 cycle, namely emissions from natural wetlands, rice cultivation, wildfires and other agricultural soils, as well as aerobic soil CH_4 uptake. We refer to the sum of these components (emissions minus soil uptake) as the LPJmL6 land CH_4 budget. To relate this modelled land budget to the global CH_4 budget, we combine LPJmL6 fluxes with independent estimates of other anthropogenic and natural sources that are not simulated by LPJmL6 (enteric fermentation and manure management, landfills and waste, fossil fuel–related emissions, biomass and biofuel burning, and additional natural sources). This allows a consistent comparison of LPJmL6 with bottom-up (BU) and top-down (TD) global estimates and with the lifetime-based constraints on total emissions.

5.3.1 Methane emissions

The global constraints on CH_4 sources and sinks outlined above allow a more detailed comparison of LPJmL6-simulated emissions with other global estimates. LPJmL6 simulates CH_4 emissions from wetlands, rice fields, and wildfires, and can distinguish between emissions from agricultural land and natural land. Furthermore, LPJmL6 explicitly represents soil CH_4 uptake via diffusion from the atmosphere into the soil. To derive the possible range of CH_4 emissions compatible with observations, source categories that are not explicitly calculated by LPJmL6 have to be added. These include anthropogenic emissions from enteric fermentation and manure management, and from landfills and waste (about 170–205 $TgCH_4\,a^{-1}$), as well as fossil fuel–related emissions (about 145 $TgCH_4\,a^{-1}$) (NOAA Global Monitoring Laboratory, 2025) and biomass combustion (about 28 $TgCH_4\,a^{-1}$). Together, these account for 462–481 $TgCH_4\,a^{-1}$ (Saunois et al., 2025, 2020; Li et al., 2021; Stanley et al., 2016). Additional natural sources not represented in LPJmL6, such as emissions from freshwater systems, geological sources, termites and the ocean, account for a further 64–259 $TgCH_4\,a^{-1}$, , with particularly large uncertainty for freshwater emissions. For the illustrative period 2010–2019, the atmospheric CH_4 sink is estimated to be between 523 and 649 $TgCH_4\,a^{-1}$.

Depending on the estimated CH_4 lifetime in the atmosphere given by Stevenson et al. (2020), between 31 and 242 $TgCH_4\,a^{-1}$ remain attributable to land net sources, for which LPJmL6 simulates about 142.1 $TgCH_4\,a^{-1}$ (wetlands, fire, rice cultivation, and other agricultural soil emissions and the explicitly simulated soil sink; mean over the years 2000 to 2019; see Table 6). If, however, we enforce global budget consistency by combining the lower (upper) estimates of the atmospheric sink with the lower (upper) estimates of CH_4 sources not simulated by LPJmL6, the

https://doi.org/10.5194/egusphere-2025-6210
Preprint. Discussion started: 22 January 2026

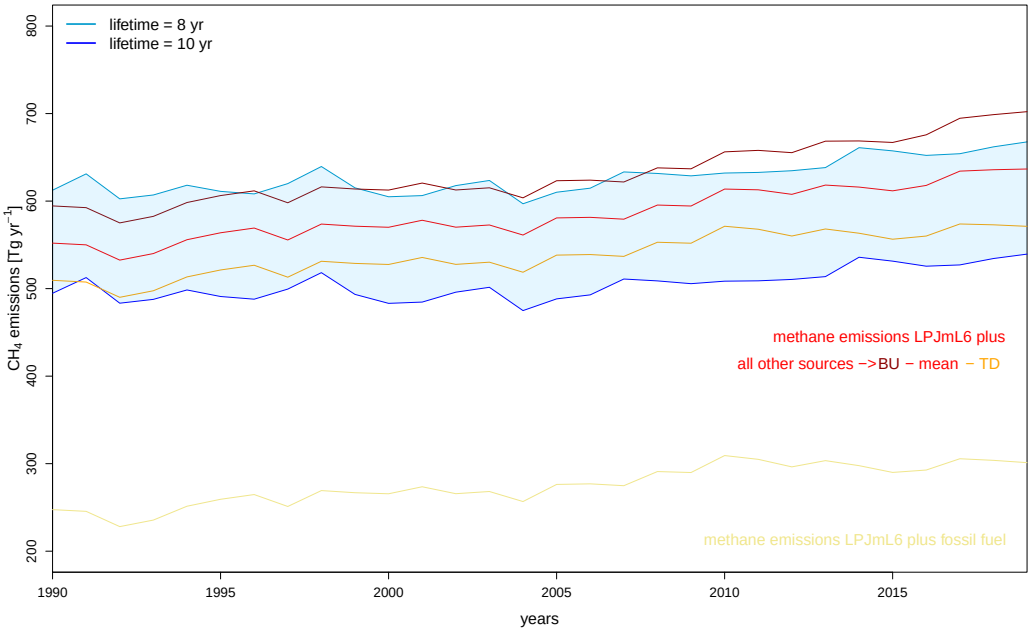

Figure 4. Global methane budget calculated from the atmospheric methane concentration and estimated lifetime of methane and the atmospheric growth resulting in the estimated overall methane sink that gives the range of the assumed methane emissions. Methane sources are anthropogenic (enteric fermentation& manure, landfills & waste, biomass & biofuel burning) and natural (incl. freshwater, geological, wildfires, termites, oceanic) (Saunois et al., 2025) and the range of the atmospheric methane lifetime is given by Stevenson et al. (2020). The two blue lines (labelled lifetime = 8 yr and lifetime = 10 yr) and the blue shaded area between them represent the atmospheric constraint, indicating the range of total global methane emissions, i.e. the region in which the sum of all sources and the soil sink should lie for a closed global methane budget. Bottom-up (BU) and top-down (TD) estimates, given as decadal means for 2000–2009 and 2010–2019, are converted to continuous annual values by linear interpolation between these two means; the resulting BU and TD time series are added to the simulated LPJmL6 methane sources and define the range shown by the orange and dark red lines. LPJmL6 simulated net methane sources include emissions from wetlands, rice cultivation, and wildfires and the soil sink.

residual range attributable to land net sources narrows to 116–157 $TgCH_4\,a^{-1}$, which still encompasses the LPJmL6 estimate (see Fig. 4).

When all emissions simulated by LPJmL6 are combined with estimates for the remaining anthropogenic and natural sources, the resulting overall CH_4 budget matches well with the observationally constrained overall emissions Fig. 4. We construct two such combined estimates: one using bottom-up (BU) values for the non-LPJmL sources and one using top-down (TD) values. Adding the same LPJmL6 land emissions to these two source data sets shifts both curves upwards by the modelled land flux; in our set-up this makes the BU-based combination systematically

https://doi.org/10.5194/egusphere-2025-6210
Preprint. Discussion started: 22 January 2026

higher and the TD-based combination lower. Consequently, the BU+LPJmL6 series forms the upper envelope and the TD+LPJmL6 series the lower envelope of the total-budget range shown by the red and orange lines in Fig. 4, respectively.

Table 5 summarizes CH_4 emissions from wetlands as estimated by the Global Methane Budget project (Kirschke et al., 2013; Saunois et al., 2016, 2020, 2025). For the period 2000–2009, BU estimates range between 147 and 175 $TgCH_4\,a^{-1}$, whereas TD estimates range from 180 to 217 $TgCH_4\,a^{-1}$. The discrepancy between these methodologies is evident across all decades examined. Notably, the differences are largest in the 1980s and 1990s, exceeding 50 $TgCH_4\,a^{-1}$. MOre recent estimates show reduced discrepancies, with TD estimates decreasing significantly while BU estimates remain relatively stable. LPJmL6 aligns closely with BU estimates, reflecting its process-based methodology and explicit integration of wetland hydrology.

Table 5. Global methane emissions in $TgCH_4\,a^{-1}$ from natural wetlands across four decades, presenting values separately for bottom-up (BU) and top-down (TD) methods. The variation reflects the methodological differences and uncertainties in emission processes.

References	1980-1989		1990-1999		2000-2009		2003-2012		2010-2019	
	BU	TD	BU	TD	BU	TD	BU	TD	BU	TD
Kirschke et al. (2013)	167^{+64}_{-52}	225^{+41}_{-42}	150^{+10}_{-6}	206^{+59}_{-37}	175^{+33}_{-33}	217^{+67}_{-40}				
Saunois et al. (2016)					166^{+38}_{-41}	183^{+39}_{-32}	167^{+35}_{-40}	185^{+112}_{-32}		
Saunois et al. (2020)					147^{+32}_{-45}	180^{+16}_{-27}				
Saunois et al. (2025)					153^{+36}_{-37}	158^{+14}_{-13}			159^{+44}_{-40}	165^{+20}_{-49}
This study*	126		134		155		164		180	

* here we report data from the simulation with actual vegetation, but exclude emissions from rice fields for consistency with the reference data

Figure 5 illustrates the latitudinal distribution of CH_4 emissions from wetlands simulated by LPJmL6 and LPJmL6–PNV in comparison with the WetCHARTs ensemble (Bloom et al., 2017b). All data sets show a pronounced maximum in the tropics, confirming the dominance of tropical wetlands in the global CH_4 budget. In these latitudes, LPJmL6 and especially LPJmL6–PNV exhibit higher peak emissions than the WetCHARTs ensemble median, while remaining largely within the ensemble spread. Outside the tropics, LPJmL6 and LPJmL6–PNV emissions generally fall within the WetCHARTs ensemble spread, with broadly comparable magnitudes in temperate and boreal latitudes and slightly enhanced values for LPJmL6–PNV at northern high latitudes.

5.3.2 Methane emissions from the different flux components

Quantifying the exact global contribution of each pathway is challenging because of spatial and temporal variability in wetland extent, hydrology and vegetation, as well as differences in wetland types and environmental conditions.

https://doi.org/10.5194/egusphere-2025-6210
Preprint. Discussion started: 22 January 2026

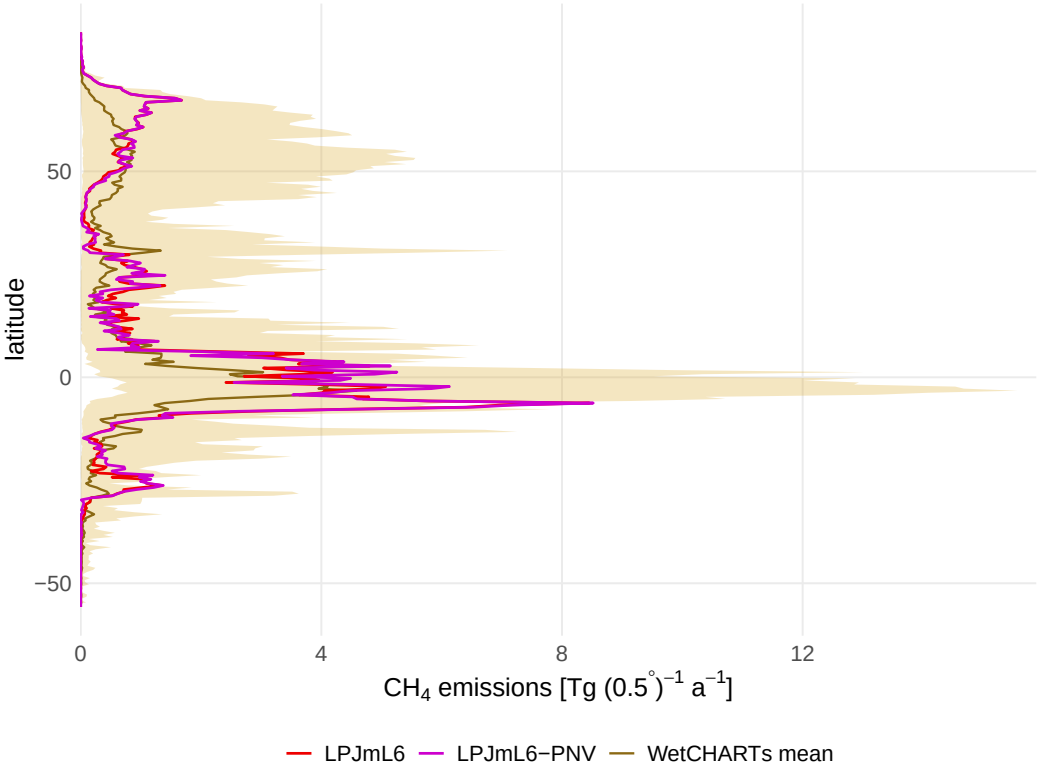

Figure 5. Latitudinal profiles of methane emissions from LPJmL6 in comparison with the WetCHARTs ensemble (Bloom et al., 2017b). Ensemble spread is shown as a shaded band and the ensemble median as a solid line.

Table 6 therefore summarises the LPJmL6 global methane budget separated into atmospheric flux pathways (diffusion, plant-mediated transport, ebullition and fire emissions) and source categories (natural wetlands, rice fields, grasslands and other cropland), together with soil oxidation and the resulting net methane sink.

The atmospheric flux partitioning shows that diffusion remains by far the dominant CH_4 emission pathway, with global emissions increasing from 117.6 to 157.5 Tg CH_4 a^{-1} between the 1980s and 2010–2019. Plant-mediated transport roughly doubles from 19.5 to 40.6 Tg CH_4 a^{-1} over the same period, whereas ebullition remains comparatively small (about 2 Tg CH_4 a^{-1}) and exhibits no clear trend, in line with the minor contribution of ebullition reported by Bieniada et al. (2021). Fire emissions are simulated at around 10 Tg CH_4 a^{-1}, consistent with independent estimates of global wildfire CH_4 emissions of approximately 10 Tg CH_4 a^{-1} and contributing about 5% of the total natural source (Saunois et al., 2025).

The soil methane sink in LPJmL6 can be compared with independent constraints. Murguia-Flores et al. (2018) estimated a global soil CH_4 sink of 33.5 Tg CH_4 a^{-1} for 1990–2009, whereas LPJmL6 simulates a stronger net uptake of about 52 Tg CH_4 a^{-1} over the same period (Table 6). A key difference is that LPJmL6 does not explicitly represent

https://doi.org/10.5194/egusphere-2025-6210
Preprint. Discussion started: 22 January 2026

Table 6. LPJmL6 estimates of global methane balance differentiated for different components in $TgCH_4\,a^{-1}$.

	1980-1989	1990-1999	2000-2009	2010-2019
diffusion	117.6	125.1	141.9	157.5
plant mediated transport	19.5	21.3	28.2	40.6
ebullition	1.8	2.3	2.2	2.7
fire emissions	9.9	10.3	9.8	9.8
total emissions	148.8	159.0	182.1	210.5
net methane sink	-47.0	-51.6	-53.3	55.1
emission on the remaining natural wetlands	117.1	123.6	141.9	166.0
emission from rice fields	13.3	14.9	17.5	20.9
emission from grasslands	6.7	7.5	8.6	9.4
emission from the remaining cropland	2.0	2.7	4.2	4.5
oxidation through the soil	137.0	145.5	148.3	147.6

the atmospheric CH_4 sink associated with methanotrophic activity in well-aerated soils; instead, CH_4 oxidation is treated as part of the soil CH_4 balance. The gross soil oxidation flux in LPJmL6 is close to 150 Tg $CH_4\,a^{-1}$, reflecting the substantial fraction of CH_4 that is oxidized while diffusing through the unsaturated zone. Despite these structural differences, the simulated net soil sink lies within, albeit towards the upper end of, the range of 9–51 Tg $CH_4\,a^{-1}$ reported by atmospheric inversions and bottom-up estimates (Saunois et al., 2025).

Because LPJmL6 explicitly represents both natural and managed ecosystems, including land use and land-use change, it can attribute global CH_4 emissions to distinct source categories. In our simulations, emissions from natural wetlands increase from 117 to 166 Tg $CH_4\,a^{-1}$ between the 1980s and 2010–2019, while emissions from rice fields rise from 13.3 to 20.9 Tg $CH_4\,a^{-1}$. This corresponds to an increase of about 57% in rice-field emissions compared to only about 13% growth in harvested rice area. Emissions from other agricultural land (excluding rice and grasslands) grow from 2.0 to 4.5 Tg $CH_4\,a^{-1}$, and grassland emissions from 6.7 to 9.4 Tg $CH_4\,a^{-1}$. For comparison, EPA (2012) estimated that other agricultural CH_4 sources contribute roughly 20 Tg $CH_4\,a^{-1}$ for 2005–2020, which is higher than the LPJmL6 estimate but broadly consistent when considering that the EPA category also includes savanna and residue burning. Overall, all simulated source categories exhibit increasing CH_4 emissions over recent decades, likely reflecting the combined effects of climate change and evolving land management; however, the relative contributions of these drivers warrant further investigation.

Another important aspect of LPJmL6 is the explicit representation of both natural and managed ecosystems, including land-use and land-use change dynamics. This structure allows us to attribute simulated changes in global CH_4 emissions to distinct source categories and regions across the terrestrial surface and to link emerging trends to underlying drivers. Such source-resolved information is essential for understanding, and ultimately mitigating, the role of wetlands and agricultural systems in global greenhouse gas budgets. The LPJmL6 model allows us to separately quantify global CH_4 emissions from natural wetlands, rice fields, grasslands and other agricultural land.

https://doi.org/10.5194/egusphere-2025-6210
Preprint. Discussion started: 22 January 2026

In the simulations, emissions from natural wetlands increase from 117 Tg $CH_4\,a^{-1}$ in the 1980s to 166 Tg $CH_4\,a^{-1}$ in 2010–2019. Emissions from rice fields rise from 13.3 to 20.9 Tg $CH_4\,a^{-1}$ over the same period, corresponding to an increase of about 57%, whereas harvested rice area increases by only about 13%. Emissions from other agricultural land (excluding rice and grasslands) grow from 2.0 to 4.5 Tg $CH_4\,a^{-1}$, and grassland emissions from 6.7 to 9.4 Tg $CH_4\,a^{-1}$. Over the same period, simulated global grassland area increases by only about 5%, implying that the roughly 40% rise in grassland CH_4 emissions is driven primarily by changing environmental conditions and management rather than by areal expansion alone. For comparison,EPA (2012) estimated that other agricultural CH_4 sources contribute roughly 20 Tg $CH_4\,a^{-1}$ for 2005–2020, which is higher than the LPJmL6 estimate but broadly consistent when considering that the EPA category also includes savanna and residue burning. Overall, all simulated source categories exhibit increasing CH_4 emissions over recent decades, consistent with the combined effects of changing climate conditions and evolving agricultural practices; however, the relative contributions of these drivers require further investigation.

5.3.3 Emission from rice cultivation, grasslands and other agricultural land

Table 7 summarizes literature estimates of global CH_4 emissions from rice cultivation, aggregated over the growing seasons, together with the corresponding LPJmL6 simulations. Most literature values are multi-year means for the period indicated in the table (rather than single-year snapshots). They are based on a range of methodological approaches, including emission-factor inventories, statistical upscaling from field measurements, and FAOSTAT-based accounting, and span roughly 18.3 to 38.8 $TgCH_4\,a^{-1}$. LPJmL6 simulates an increase from a global mean of 13.0 $TgCH_4\,a^{-1}$ in the 1980s to 20.4 $TgCH_4\,a^{-1}$ during 2010–2019, which places our results toward the lower end of the published range (Table 7). A likely explanation is that the current representation of rice production systems assumes one cropping season per grid cell, whereas multi-cropping (double or even triple rice) is widespread in parts of South and Southeast Asia and eastern China (Waha et al., 2025, 2020). In such regions, annual emissions exceed the values simulated by LPJmL6 because emissions from multiple growing seasons within a calendar year are not explicitly represented. In annual sums of LPJmL6 simulated emissions, we combine planted rice area with those from wetland-setaside emissions on these fields, which captures major biogeochemical controls but may still under-represent management effects such as straw incorporation, organic amendments, and deliberate drainage. In the LPJmL6 simulations, the unproductive (non-growing) period contributes about 4 $TgCH_4\,a^{-1}$. While the emission estimates obtained with other methodologies are strongly influenced by how the contributing days are defined, the very wide range of 8 – 78 Tg $CH_4\ a^{-1}$ simulated by by the process-based model CH4MOD (Hu et al., 2024) is mainly driven by differing assumptions about management.

Across rice-growing regions, methane emissions from rice fields exhibit strong spatial and temporal variability. LPJmL6 simulates country-mean cumulative growing-season emissions that range from a few to more than 100 $gCH_4\,m^{-2}\,a^{-1}$, with local grid-cell values reaching up to 328 $gCH_4\,m^{-2}\,a^{-1}$ in the most strongly emitting areas (Table 8). The observed values compiled in Table 9 span a comparable order of magnitude, with maximum values

https://doi.org/10.5194/egusphere-2025-6210
Preprint. Discussion started: 22 January 2026

Table 7. Global CH_4 emissions from rice cultivation during the growing season

Source	Global Emissions ($TgCH_4\,a^{-1}$)	years	Methodology
Yan et al. (2009)	18.3 – 38.8	2000	IPCC Tier 2, based on global EF database
Hu et al. (2024)	8 – 78	2008 – 2017	Process-Based Model (CH4MOD) under different management
Pazhanivelan et al. (2024)	19.9	2017 – 2018	Tier 2/Remote Sensing
FAO (2020c)	24.4	2010 – 2019	Modeled emissions based on FAOSTAT data
EPA (2012)	18.4	2015	IPCC-based bottom-up modeling
Wang et al. (2023a)	27 ± 6	2008 – 2017	IPCC Inventory Guidelines (Tier 2/3)
Saunois et al. (2025)	25 – 37	2010 – 2019	Integrated from national inventories
This study	20.9	2010 – 2019	simulated by LPJmL6

Table 8. Country-level cumulative CH_4 emissions from rice fields during the growing season simulated by LPJmL6 (1990–2014 mean, $gCH_4\,m^{-2}\,a^{-1}$). For each country, the table reports the mean, minimum, and maximum emissions within the national rice area.

Country	Mean	Min	Max
Bangladesh	13.62	3.46	39.24
Brazil	75.84	4.21	222.90
China	17.62	0.77	52.91
India	11.18	0.94	34.08
Indonesia	33.58	0.35	238.21
Italy	19.52	0.06	104.86
Japan	7.83	0.01	48.53
Philippines	3.45	0.58	9.42
South Korea	10.15	0.09	29.94
Spain	10.99	0.22	38.08
Uruguay	110.20	3.10	328.15
Vietnam	21.18	1.04	46.90

extending from about 13 up to 347.5 $gCH_4\,m^{-2}\,a^{-1}$, indicating pronounced sub-national heterogeneity within the sampled regions. Independent field studies further highlight the very strong variability of rice CH_4 emissions. Wang et al. (2022) report substantial year-to-year differences in growing-season emissions from Chinese rice fields, with high emissions of 36.8 $gCH_4\,m^{-2}\,a^{-1}$ in 2018 and low emissions of 5.3 $gCH_4\,m^{-2}\,a^{-1}$ in 2019, while Qian et al. (2023) document even higher plot-scale values approaching 580 $gCH_4\,m^{-2}\,a^{-1}$ under specific conditions, illustrating the potential for extreme fluxes in certain regions or management settings. It is important to note that LPJmL6 always provides spatially complete coverage of each national rice area, whereas most literature values in Table 9 are

https://doi.org/10.5194/egusphere-2025-6210
Preprint. Discussion started: 22 January 2026

derived from individual sites or sub-regions and therefore cannot be interpreted as true national means, even in the comparatively extensive dataset of Wang et al. (2018). This mismatch in spatial representativeness, together with differences in local management practices, environmental conditions and measurement protocols, explains part of the discrepancies between simulated and observed ranges, while the overall overlap in magnitude supports the ability of LPJmL6 to capture first-order patterns of rice CH_4 emissions.

Table 9: Observed cumulative CH_4 emissions from rice fields during the rice-growing season ($gCH_4\,m^{-2}\,a^{-1}$), compiled from field studies and grouped by region. Reported minimum and maximum values denote the lowest and highest growing-season emissions observed across the years covered in each study.

Region	Country	Mean	Min	Max	Reference
East Asia	China	–	0.3	127.4	Wang et al. (2018)
East Asia	China	19.9	1.0	97.0	Zhu and Li (2024)
East Asia	Japan	–	0.6	86.2	Wang et al. (2018)
East Asia	South Korea	–	9.7	214.5	Wang et al. (2018)
South Asia	India	–	0.8	347.5	Wang et al. (2018)
South Asia	India	–	3.0	15.0	Gupta et al. (2021)
South Asia	India	7.7	0.4	19.0	Bhatia (2013)
South Asia	Bangladesh	–	11.6	13.2	Wang et al. (2018)
Southeast Asia	Philippines	–	0.3	95.6	Wang et al. (2018)
Southeast Asia	Philippines	–	2.00	55.0	Wassmann et al. (2000)
Southeast Asia	Vietnam	–	3.1	35.3	Wang et al. (2018)
Southeast Asia	Indonesia	–	2.6	72.2	Wang et al. (2018)
South America	Brazil	–	4.6	51.7	Wang et al. (2018)
South America	Uruguay	–	9.33	24.9	Wang et al. (2018)
Europe	Spain	–	6.9	97.2	Wang et al. (2018)
Europe	Italy	–	0.8	81.9	Wang et al. (2018)

Globally, grasslands exhibit simulated CH_4 emissions that are half those from rice paddies, as indicated in Table 6. This important source of CH_4 emissions arises from two primary factors. First, the vast spatial extent of grasslands worldwide provides a substantial area for CH_4 production and emission, despite the generally lower CH_4 fluxes per unit area compared to rice paddies. Second, many grassland regions, particularly those converted from historical peatlands, are characterized by drained organic soils. The drainage of these former peatlands for agricultural use not only alters the hydrological regime but also influences the soil carbon dynamics, creating conditions conducive to CH_4 emissions (van den Pol-van Dasselaar, 1998). Residual croplands constitute a small but non-zero CH_4 source that is highly sensitive to field-scale hydrology. Even in nominally aerated systems, shallow or perched water tables,

https://doi.org/10.5194/egusphere-2025-6210
Preprint. Discussion started: 22 January 2026

episodic waterlogging after irrigation or storms, and poorly drained depressions can create anoxic microsites where methanogenesis occurs. The resulting emissions are intermittent and heterogeneous, governed primarily by water-table depth and inundation frequency. Although flux magnitudes are typically far lower than those from wetlands, such emissions can be regionally relevant in poorly drained landscapes and in wet seasons, and they carry high spatial and interannual variability.

5.4 Carbon pools and fluxes

The implementation of the anoxic decomposition also influences the organic carbon pools and the CO_2 fluxes into the atmosphere. Therefore the LPJmL6 model needs to be benchmarked for the other important carbon cycle variables as well.

5.4.1 Net biome production

The release of soil carbon is decelerated due to the representation of wetlands in the LPJmL6 models. The anoxic decomposition is about 10 times slower and thus carbon is sequestered in soils for a much longer time. Thus the model can well reproduce the magnitude of the global carbon sink – including land-use change (LUC) emissions – within the estimate range of the Global Carbon Budget (GCB) 2023 (Friedlingstein et al., 2023) from Dynamic Global Vegetation Models (DGVM) and from the bookkeeping approach (DGVM-LU-BK) (see Table 10 and Fig. 6). Table 10 shows that LPJmL6 reproduces decadal terrestrial sink magnitudes within the GCB 2023 DGVM and DGVM-LU-BK uncertainty ranges and exhibits the expected strengthening from the 1990s to the 2010s; across the two GCB methods, residual differences can be traced to land-use-change treatment—bookkeeping versus implicit DGVM dynamics—and no systematic decadal bias is evident; this also holds for LPJmL6, indicating robust, method-invariant trends in the net land carbon sink. In Fig. 6, the simulated terrestrial sink follows the independently constrained apparent sink and the atmospheric CO_2 growth rate with comparable interannual variability, indicating that LPJmL6 captures the major climate-driven fluctuations and the multi-decadal increase in sink strength without long-term divergence from independent estimates.

5.4.2 Net ecosystem exchange

We used eddy-covariance flux tower data to benchmark simulated NEE (Fig. 7; full data description in section 4.2). As noted there, comparisons are constrained by scale mismatches between grid cells and tower footprints, possible vegetation (PFT) mismatches, and the use of large-scale meteorological forcing rather than site-specific observations, which limits the ability to capture site-specific variability in carbon fluxes.

Nevertheless, the comparison demonstrates that correlations between simulated and observed fluxes are generally high across many sites, indicating that the model captures the overall temporal dynamics of NEE reasonably well. However, the centered root mean square difference (CRMSD) and the normalized standard deviation reveal larger

https://doi.org/10.5194/egusphere-2025-6210
Preprint. Discussion started: 22 January 2026

Table 10. Net biome production-Terrestrial land sink including land use change emissions estimated by Global Carbon Budget 2023 and simulated by LPJmL6

	GCB 2023		LPJmL6
	DGVM (net)	DGVM-LU-BK	
1990s	0.7 ±0.5	0.9 ±0.9	1.1
2000s	1.1 ±0.4	1.4 ±1.0	1.3
2010s	1.6 ±0.6	2.0 ±1.0	2.0

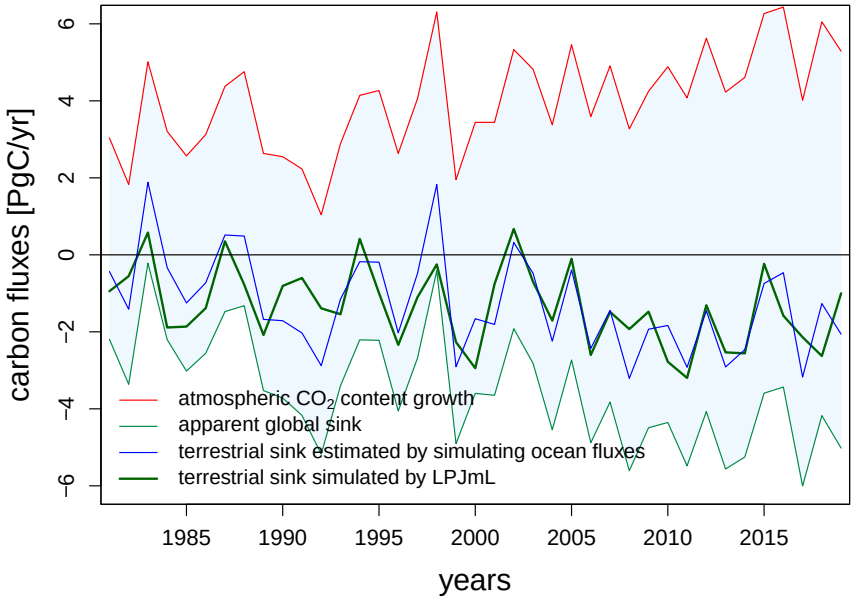

Figure 6. Terrestrial sink estimated by LPJmL6 and Global Carbon Budget 2023 (Friedlingstein et al., 2023).

discrepancies, suggesting that while the timing of seasonal and interannual variability is reproduced, the magnitude of fluxes is often either over- or underestimated.

5.4.3 GPP

The ILAMB comparison demonstrates that the model successfully reproduces gross primary production (GPP) within the same order of magnitude as reported by Jung et al. (2011) (global mean 119 ±6 PgC a^{-1} for 1982–2008 vs. 126 PgC a^{-1} simulated by LPJmL6). This agreement is also in line with later FLUXCOM syntheses that place

https://doi.org/10.5194/egusphere-2025-6210
Preprint. Discussion started: 22 January 2026

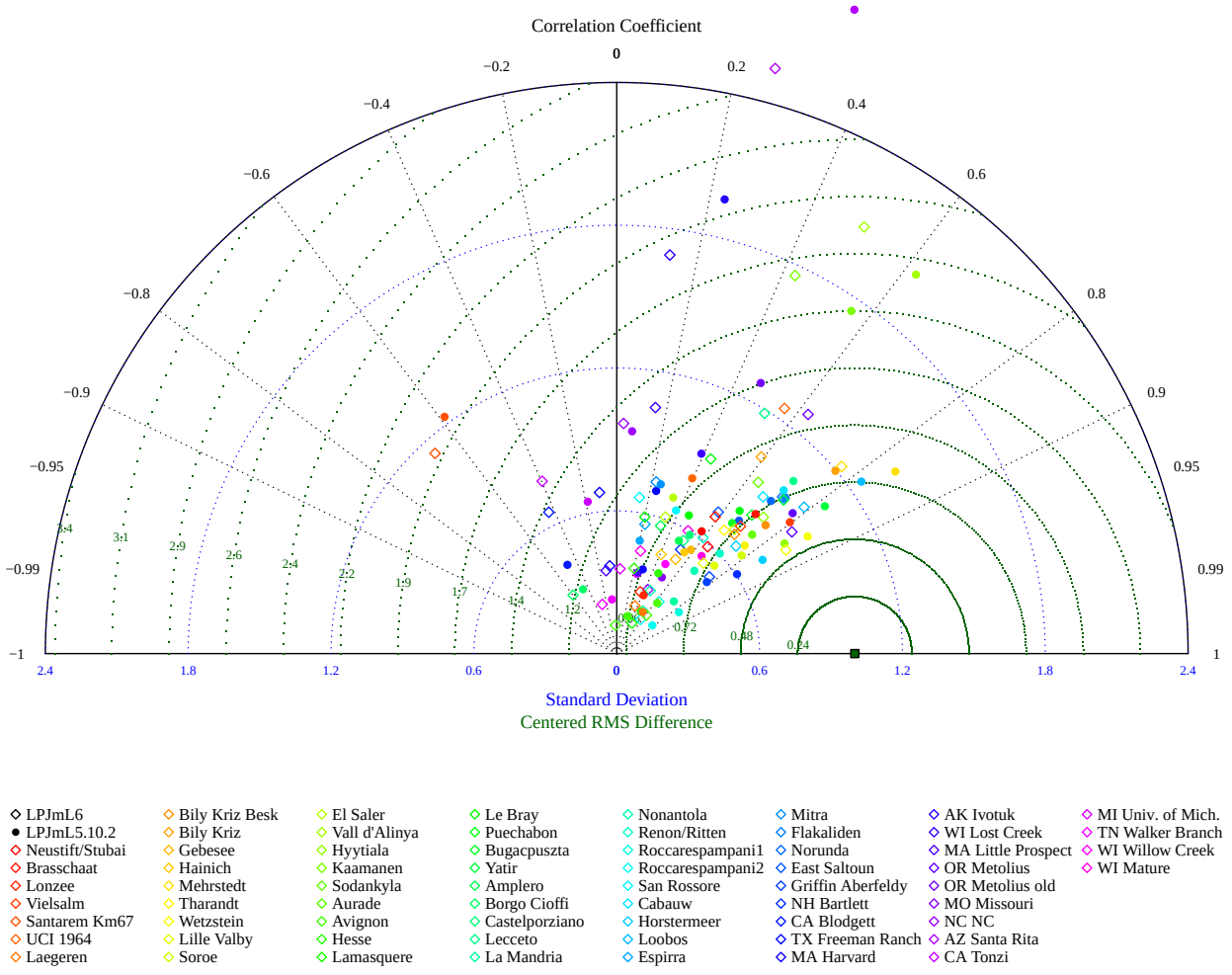

Figure 7. Taylor diagram showing the comparison of simulated net ecosystem exchange (NEE) against eddy-covariance flux tower measurements. Observational data are derived from the FLUXNET network, which provides standardized eddy-covariance measurements of ecosystem–atmosphere carbon and water fluxes (Pastorello et al., 2020)

global GPP roughly in the 106–130 PgC a^{-1} range, depending on predictors and machine-learning methods used (Jung et al., 2020).

5.4.4 Aboveground biomass (AGB)

Across the ILAMB benchmark, reference biomass products differ in scope (forest AGB vs. all vegetation; above- vs. below-ground components), spatial/temporal coverage, and retrieval/inversion methodology, yielding a wide spread

https://doi.org/10.5194/egusphere-2025-6210
Preprint. Discussion started: 22 January 2026

in implied global stocks. LPJmL6 estimates global woody biomass to be 422 PgC (mean 2000–2019). Among reference datasets, products that resolve high biomass in humid tropical and high-latitude forests report totals comparable to LPJmL6, for example, GEOCARBON ∼408 PgC (GEO, 2014); the Xu–Saatchi synthesis 381 ± 2 PgC for 2000–2019 (Xu et al., 2021). By contrast, ESA CCI Biomass provides forest AGB of ∼300 PgC (above-ground forest only) (GEO, 2014; Santoro et al., 2021), and NBCD2000 is regional (conterminous U.S., sim∼2000 baseline), serving primarily for spatial pattern evaluation rather than global sums (Kellndorfer et al., 2012). These definitional and methodological contrasts account for the spread in ILAMB intercomparisons and explain why LPJmL6 aligns more closely with datasets emphasizing woody stocks across humid tropical and boreal forests, whereas ESA CCI implies lower global totals.

From the reference data sets used in ILAMB, only the Xu–Saatchi (Xu et al., 2021) product (381 PgC) aligns closely with the LPJmL6 simulation result of 422 PgC, whereas most other datasets imply substantially higher global biomass totals ranging from 300 to 408 PgC.

5.5 Water fluxes

We assess the large-scale terrestrial water cycle to ensure that the CH_4 implementation operates within a physically consistent land-surface framework. The analysis combines global budgets with spatial diagnostics (renewable water resources and groundwater recharge) and skill metrics for multi-decadal river discharge and evapotranspiration (ET) simulations.

5.5.1 Global water fluxes

Table 11 synthesizes ranges of data-driven and model-based estimates for the principal terrestrial water fluxes – evapotranspiration (ET), transpiration (T), total runoff from land, groundwater recharge, and irrigation withdrawals. ET ($62\times10^3\,km^3\,a^{-1}$) and T ($39\times10^3\,km^3\,a^{-1}$) fall within published model ranges and are near the lower bounds of data-driven syntheses, indicating a conservative global partitioning of ET. Total runoff and river discharge (47 and $40\times10^3\,km^3\,a^{-1}$) lie near the centers of reported ranges, consistent with independent constraints. Groundwater recharge ($31\times10^3\,km^3\,a^{-1}$) exceeds data-driven and modeled estimates; this difference reflects varying definitions (diffuse vs. focused recharge and return flows), considered land areas, and averaging periods, also examined spatially in section 5.5.2, with discharge and ET evaluations provided in sections 5.5.3 and 5.5.4. Nevertheless, the LPJmL6 estimate is near the upper end of published values and coincides with greater groundwater storage in the simulations than reported Müller Schmied et al. (2021) (Fig. 8).

5.5.2 Groundwater recharge and renewable storage

Fig. 8 compares long-term mean groundwater storage (GWS) and groundwater recharge for 1981–2010 from WaterGAP 2.2 (Müller Schmied et al., 2021) and LPJmL6. Recharge is highest in humid tropics and monsoon regions

https://doi.org/10.5194/egusphere-2025-6210
Preprint. Discussion started: 22 January 2026

Table 11. Simulated global terrestrial water fluxes, and ranges of data-driven and modeled estimates (in $10^3\,km^3\,a^{-1}$). Evapotranspiration and transpiration represent long-term land averages (1982–2011); runoff and discharge are multi-decadal climatologies (1982–2011 land means); infiltration denotes diffuse groundwater recharge; irrigation withdrawals (around 2010) include both surface and groundwater abstraction.

Flux	Data-driven ($10^3\,km^3\,a^{-1}$)	Modelled ($10^3\,km^3\,a^{-1}$)	LPJmL6 ($10^3\,km^3\,a^{-1}$)
Evapotranspiration (ET)[1,2]	64–69	50–70	62
Transpiration (T)[3,4]	55 ± 12	39–52	39
Total runoff (land)[5,6,7]	41–46	40–50	47
Groundwater recharge[9,10]	12–13	∼11–30	31*
Irrigation withdrawals (blue water)[11–14]	2.4–2.9	2.3–3.3	2.2

References: [1] Pan et al. (2020); [2] Wild et al. (2015); [3] Jasechko et al. (2013); [4] Good et al. (2015); [5] Schneider et al. (2017); [6] Godoy et al. (2021); [7] Döll et al. (2016); [8] Mohan et al. (2018); [9] Döll and Fiedler (2008); [10] FAO (2020a); [11] Wada and Bierkens (2014a); [12] Wada and Bierkens (2014b); [13] Huang et al. (2018); [14] FAO (2014);

*including return flows from irrigation

(Amazon, Congo, SE Asia, eastern India), and is moderate in temperate wet zones, and near zero across arid belts (Sahara, Arabian Peninsula, central Australia); orographic bands (Andes, Himalaya) are evident. Storage broadly tracks persistently wet lowlands and large sedimentary basins, with minima in deserts and high-latitude regions. LPJmL6 tends to display sharper spatial gradients and stronger orographic signals, while WaterGap is smoother and often more conservative in semi-arid interiors.

5.5.3 Discharge for large river basins

The comparison of discharge data shows that LPJmL6 is able to reproduce the seasonal hydrographs (see Fig. 9 and in the Supplement Fig. S8, especially in the southern latitudes. There are small improvements compared to LPJmL5.10. The far northern discharge levels are also reproduced quite well, with the largest discrepancy in the mid-latitudes. In some regions with low R^2 , errors are dominated by timing mismatch: the model typically leads the observed cycle (peaks occur earlier), while amplitudes are reasonably captured (see Supplement Fig. S8).

5.5.4 Evapotranspiration fluxes

Simulated ET was compared against eddy-covariance flux tower measurements. While towers provide high-frequency and highly localized ET estimates, the coarse spatial resolution of the simulations introduces a scale mismatch similar to that encountered for NEE.

Model-data agreement of ET is even higher than for NEE, in terms of both correlation coefficients (the model reproduces the temporal variability of ET with greater accuracy) and the CRMSD and the normalized standard

https://doi.org/10.5194/egusphere-2025-6210
Preprint. Discussion started: 22 January 2026

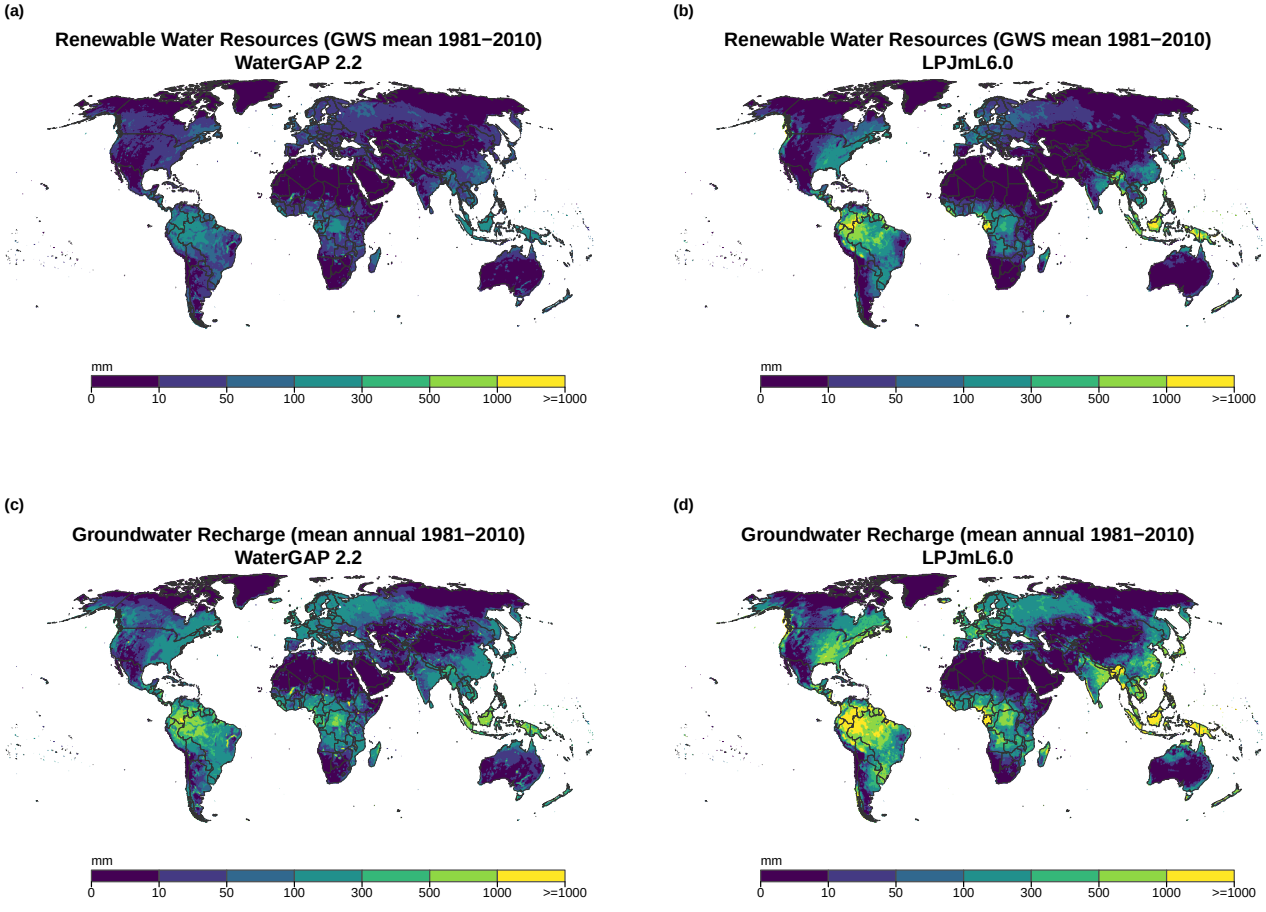

Figure 8. Comparison of WaterGAP 2.2 (Müller Schmied et al., 2021) and LPJmL6 maps of (a,b) renewable groundwater storage (GWS; multi-year mean, 1981–2010) and (c,d) groundwater recharge (mean annual, 1981–2010). Colors show discrete classes for storage in mm; for recharge the units are mm a^{-1}.

deviation (the magnitude of ET fluxes is represented more consistently across sites). This likely reflects the fact that ET is primarily controlled by atmospheric demand and canopy conductance, processes that are more directly constrained by meteorological forcing and vegetation structure in the model, whereas NEE additionally depends on complex carbon turnover processes and ecosystem-specific dynamics.

5.6 Vegetation distribution

A comparison of LPJmL6-simulated actual land cover (natural vegetation plus managed cropland and grassland) witj ESA CCI LC4 land-cover product (Harper et al., 2023) reveals a generally good match in spatial patterns

https://doi.org/10.5194/egusphere-2025-6210
Preprint. Discussion started: 22 January 2026

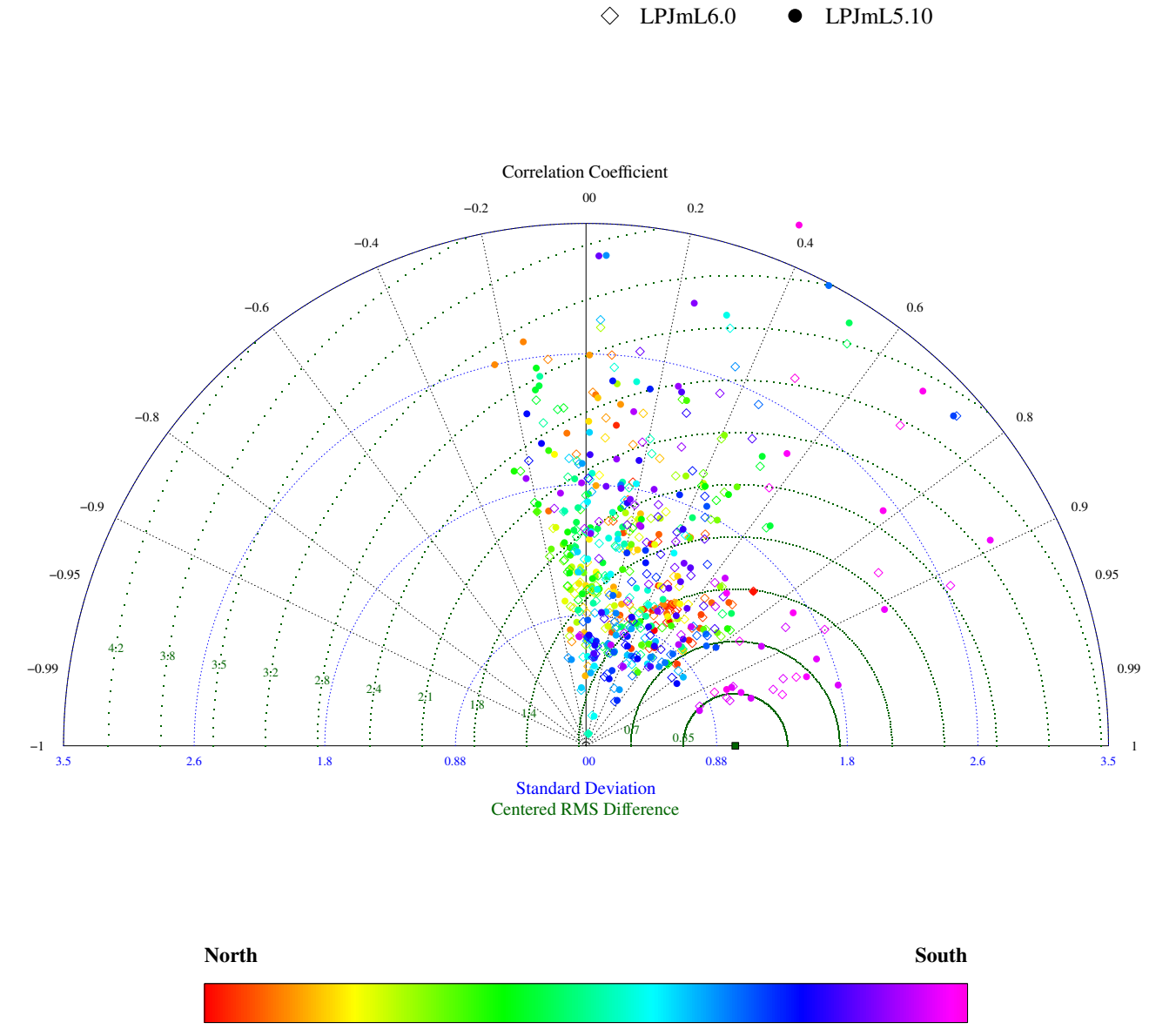

Figure 9. Comparison of simulated discharge with 286 gauges provided by ArcticNET and UNH/GRDC. Stations with basin area $> 10000\,\mathrm{km}^2$ are taken into account. Gauges are ordered from north to south by color (see legend).

https://doi.org/10.5194/egusphere-2025-6210
Preprint. Discussion started: 22 January 2026

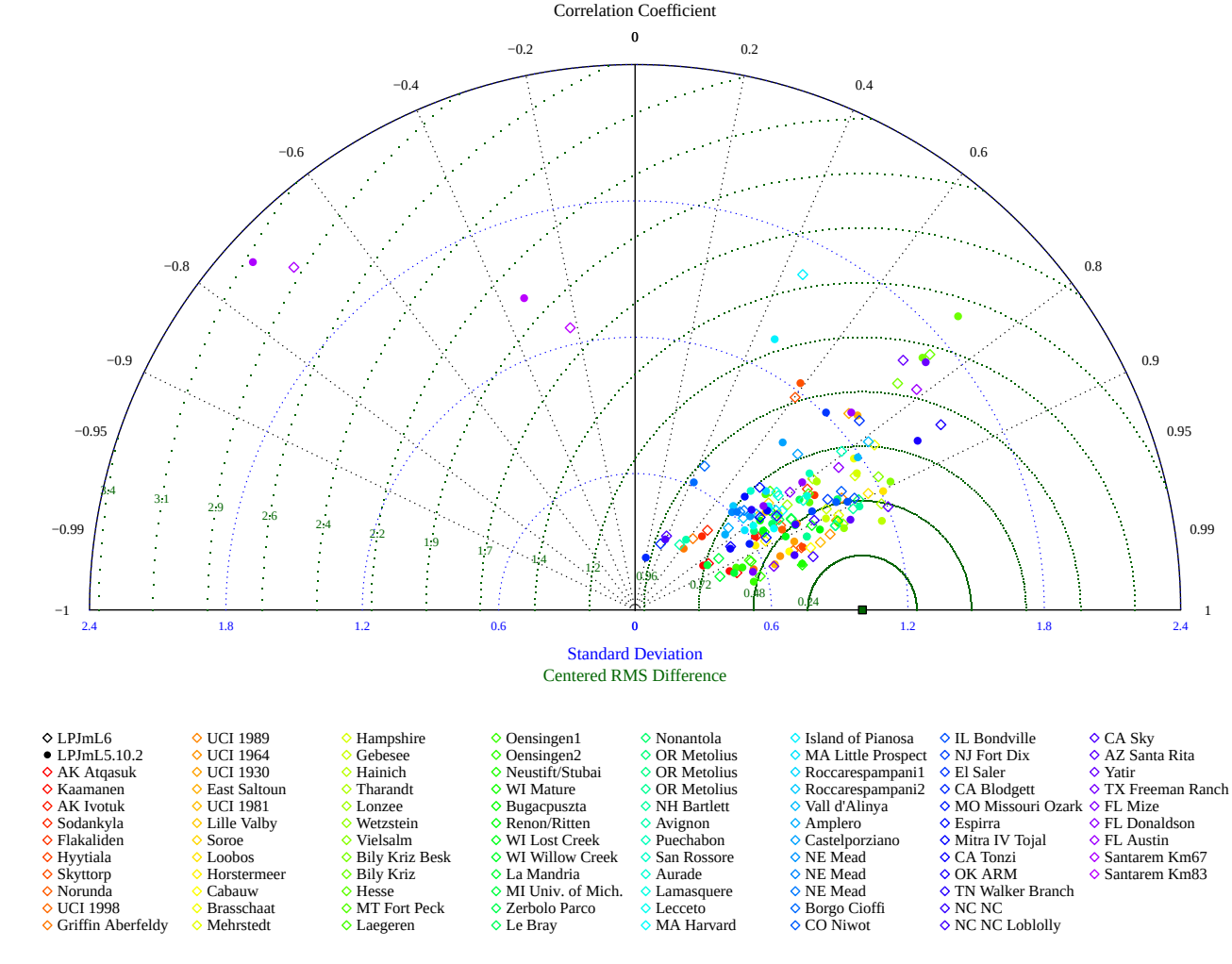

Figure 10. Taylor diagram showing the comparison of simulated evapotranspiration fluxes against eddy-covariance flux tower measurements. Observational data are derived from the FLUXNET network, which provides standardized eddy-covariance measurements of ecosystem–atmosphere carbon and water fluxes (Pastorello et al., 2020)

for PFTs (Fig. 11). However, in the temperate and southern boreal zone, ESA CCI LC4 data predominantly show broadleaved summergreen trees, while LPJmL6 simulates a substantially lower abundance of this PFT. Part of this divergence likely stems from the LC-to-PFT reclassification applied to ESA CCI LC4, which can inflate broadleaved summergreen fractions in mosaic and open-forest landscapes and has been shown to introduce spatially structured errors, including overestimation near the taiga–tundra ecotone (Wang et al., 2023b). In the inner tropics, LPJmL6 dominantly simulates broadleaved evergreen trees in line with the observed data, yet it also produces a minor

https://doi.org/10.5194/egusphere-2025-6210
Preprint. Discussion started: 22 January 2026

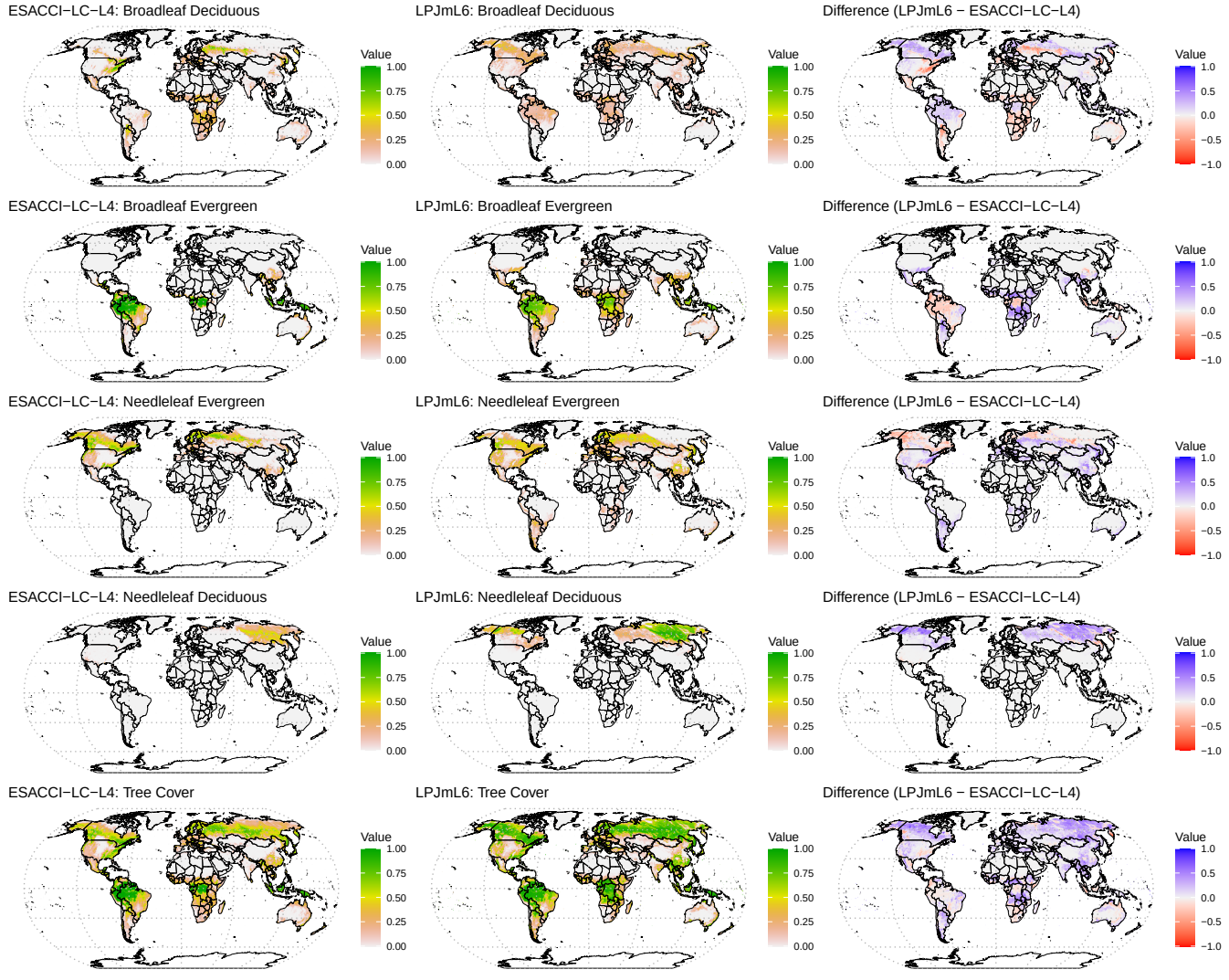

Figure 11. Vegetation distribution of LPJmL6 compared to ESACCI-LC-L4 data (Harper et al., 2023)

fraction of broadleaved deciduous cover, consistent with the common deciduous–evergreen coexistence in tropical forests (Muehleisen et al., 2024), reflecting the influence of rainfall variability. Mora et al. (2014) suggest that remote sensing data, such as the ESA CCI LC4 dataset, may overestimate the extent of broadleaved evergreen trees in these regions due to challenges in distinguishing between evergreen and deciduous species under dense canopies and during certain seasons. Factors contributing to this misclassification include mixed pixel composition, seasonal variations in leaf phenology, and limitations in sensor resolution. For instance, the complexity of tropical forest structures and the similarity in spectral signatures between different tree species can lead to inaccuracies in classification (Zhong et al., 2024). Finally, while the model effectively simulates the presence of needleleaved deciduous trees in appropriate areas,

https://doi.org/10.5194/egusphere-2025-6210
Preprint. Discussion started: 22 January 2026

aligning well with ESA observations, LPJmL6 tends to over-represent their overall abundance in the high-latitude boreal forests of Eurasia and North America.

Uncertainties also arise from the representation of land use, both in observational products and in the prescribed land-use forcing used to drive LPJmL6. Reconstructions and scenarios of cropland and pasture area differ substantially among datasets, particularly in regions with smallholder or mosaic agriculture, leading to divergent estimates of the area available for natural and managed PFTs (e.g. Prestele et al., 2016; Hurtt et al., 2020; Klein Goldewijk et al., 2017b). These discrepancies propagate into both the LC-to-PFT reclassification of ESA CCI LC4 and the land-use trajectories imposed on LPJmL6, so part of the mismatch between simulated and observed PFT patterns likely reflects uncertainties in land-use data rather than Vegetation dynamics alone.

6 Conclusions

We present LPJmL version 6, including a newly developed process-consistent CH_4 module that links hydrological, vegetation dynamical and biogeochemical processes to atmospheric CH_4 exchange. A new wetland scheme combines a dynamic water table with a CTI-based inundation fraction that is recalculated from the grid-cell CTI distribution, enabling the simulation of spatially and temporally varying anoxic areas within each cell.

Evaluation demonstrates (i) agreement in global wetland area with several inventories, while highlighting a persistent, first-order observational divergence (3.6–11.4 million km^2) that translates into different emission potentials; LPJmL6 captures the tropical signal and part of the mid-latitude peak but remains conservative in boreal zones relative to GLWD. (ii) global CH_4 emissions that are consistent with atmospheric measurement constraints when combined with non-modeled sectors that bring the modeled net flux into the 506–630 Tg CH_4 a^{-1} corridor for 2008–2017. (iii) mechanistic attribution showing diffusion as a leading pathway and ebullition as small, with fires contributing 5% of natural sources. LPJmL6 successfully simulates the interactions between environmental factors such as temperature, soil moisture, and vegetation, which govern CH_4 production, oxidation, and transport. Its ability to capture regional and temporal emission trends aligns well with observational datasets and other global estimates, particularly in high-emission regions like tropical wetlands and rice cultivation areas. However, the model also highlights uncertainties in CH_4 emissions from agricultural land and high-latitude regions, emphasizing the need for improved data on wetland dynamics and small-scale CH_4 sources. Uncertainties are dominated by (a) wetland extent in high latitudes and (b) agricultural sources, including rice-area dynamics and management, which LPJmL6 now resolves but for which observational constraints remain unequivocal. The model aligns with bottom-up wetland emission estimates across decades, while top-down estimates have converged downward, reducing the historical BU–TD gap and supporting the process-based approach.

The implementation of CH_4 dynamics in LPJmL6 represents a significant advancement in the modeling of terrestrial land surface dynamics and, in particular, CH_4 emissions. By integrating CH_4 processes within the broader framework of the global carbon, nitrogen, and water cycles, the model allows for detailed assessments of emissions

https://doi.org/10.5194/egusphere-2025-6210
Preprint. Discussion started: 22 January 2026

from different land-use groups, here reported separately for natural wetlands, rice paddies, grasslands, and the remaining cropland. The dynamic representation of wetlands and permafrost processes, combined with hydrological modeling, enhances the understanding of CH_4 flux variability across diverse ecosystems.

CH_4 emissions from land use and wetlands are a significant contributor to climate change. Forested wetlands, wetland dynamics, permafrost, and various anthropogenic and natural sources contribute all to the global CH_4 budget. By understanding the complex dynamics of CH_4 emissions and their environmental regulation, effective strategies for mitigating climate change can be developed. Continued research and monitoring of CH_4 emissions are essential for improving our understanding of this potent greenhouse gas and its impact on the planet.

LPJmL6 is a robust tool for understanding the complexities of CH_4 dynamics under current and future climate conditions. These advances allow for more accurate projections of CH_4 emissions, critical for formulating effective climate-mitigation policies. Continued refinement of CH_4-related processes, such as improved parameterization of wetland extents and anthropogenic emission factors, will further increase the realism of LPJmL6-derived surface fluxes. When these fluxes are used in, or coupled to, atmospheric transport and chemistry modules within Earth system modelling frameworks, they can help to better constrain the global CH_4 budget and attribution of observed concentration trends, thereby supporting more robust climate-impact assessments. In addition to enhancing CH_4 representation, the improvements made to the soil water status significantly advance the model's ability to capture land surface dynamics. This enhancement is particularly impactful for simulating water stress in natural vegetation and crops, leading to more accurate representation of plant-water interactions. Notably, this advancement represents a co-benefit of the CH_4-focused implementation, offering improvements beyond CH_4 simulations by strengthening the model's capacity to simulate hydrological processes and their influence on terrestrial ecosystems.

Code and data availability. The LPJmL6 model version further developed and used in this study is archived on Zenodo: https://zenodo.org/records/17911633 (Schaphoff et al., 2025b) and is also available from GitHub (https://github.com/PIK-LPJmL/LPJmL). The evaluation and analysis scripts, including all ILAMB validation scripts and configuration files required to reproduce the diagnostics, are likewise archived on Zenodo: https://doi.org/10.5281/zenodo.17877397 (Schaphoff et al., 2025a). The LPJmL6 model output used for the evaluation in this paper is provided in NetCDF format via Zenodo: https://doi.org/10.5281/zenodo.17877397 (Schaphoff et al., 2025a). Together, these repositories contain all model code, scripts, and simulation data necessary to reproduce the results presented here, apart from the external observational and benchmark data sets, which are available from the original providers cited in the main text.

All observational, remote-sensing, and synthesis products used for model evaluation are third-party datasets and are not redistributed with this manuscript; users must obtain them directly from the original providers under their respective licenses/usage policies. Wetland extent evaluation used: the Global Lakes and Wetlands Database (GLWD; https://www.worldwildlife.org/pages/global-lakes-and-wetlands-database, accessed 2018-08-15; the Kaplan wetland map (https://doi.org/10.5281/zenodo.18274983); the SWAMP "Tropical and Subtropical Wetlands Distribution" dataset (https://doi.org/10.17528/CIFOR/DATA.00058, accessed 2024-11-24); and WAD2M wetland dynamics (https://zenodo.org/records/5553187, accessed

https://doi.org/10.5194/egusphere-2025-6210
Preprint. Discussion started: 22 January 2026

2024-09-03). Latitudinal CH_4 emission benchmarking used WetCHARTs v1.0 (https://doi.org/10.3334/ORNLDAAC/1502, accessed 2017-06-01). Atmospheric constraints used CarbonTracker-CH_4 (https://gml.noaa.gov/ccgg/carbontracker-ch4/, accessed 2024-02-28) and NOAA CH_4 trend products (https://gml.noaa.gov/ccgg/trends_ch4/, accessed 2024-02-28). Eddy-covariance NEE and ET were taken from FLUXNET2015 (https://fluxnet.org/data/fluxnet2015-dataset/, accessed 2017-04-17). Vegetation structure evaluation used ESA CCI Land Cover "Global Plant Functional Types (PFT) Dataset" (http://maps.elie.ucl.ac.be/CCI/viewer/download.php, accessed 2022-08-19). System-level synthesis constraints used the Global Carbon Budget data (https://doi.org/10.18160/GCP-2023, accessed 2024-03-15) and the Global Methane Budget data portal (https://www.globalcarbonproject.org/methanebudget/ and data page https://www.globalcarbonproject.org/methanebudget/24/data.htm, accessed 2024-03-18). R-ArcticNET v4.0 station attributes and monthly discharge tables are available from the project download at https://www.r-arcticnet.sr.unh.edu/v4.0/AllData/index.html, accessed 2012-05-15 (R-ArcticNET Project). RivDIS v1.1 can be accessed via https://doi.org/10.3334/ORNLDAAC/199, accessed 2015-03-14 (Vörösmarty et al., 1998).

Multi-metric benchmarking used ILAMB software and its reference dataset collection (https://www.ilamb.org/; datasets: https://www.ilamb.org/datasets.html).

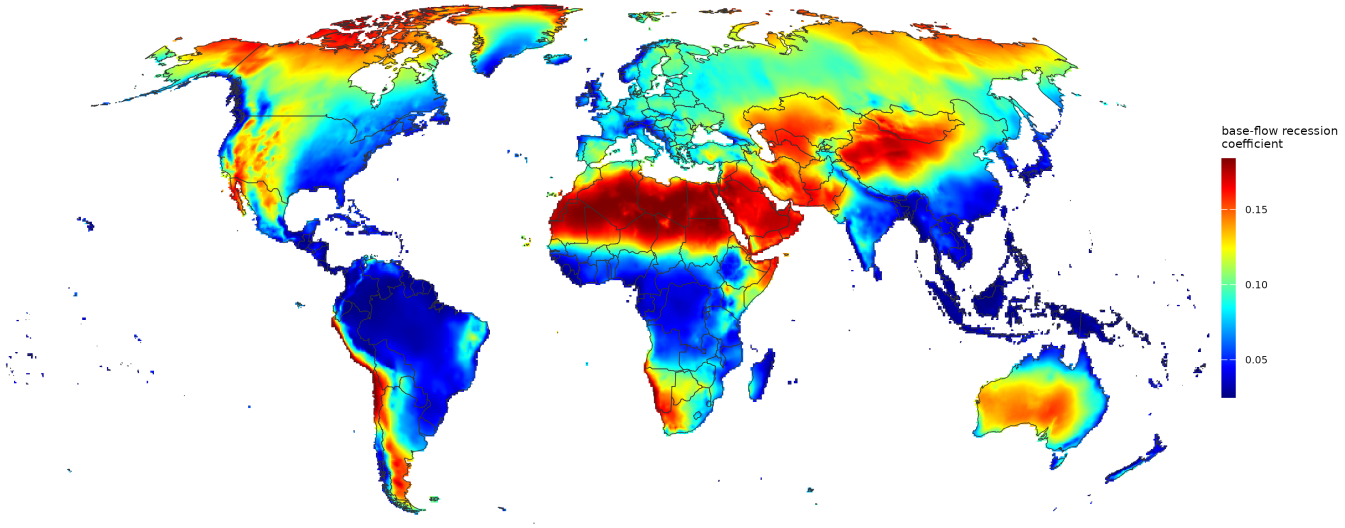

Figure A1. Base-flow recession coefficient determining the outflow rate from groundwater stores as a fraction of the store (ERMITAGE project report (2013),).

https://doi.org/10.5194/egusphere-2025-6210
Preprint. Discussion started: 22 January 2026

Table A1. Abbreviation of PFTs and CFTs.

Tropical broadleaved evergreen tree	TrBrEv
Tropical broadleaved raingreen tree	TrBrDe
Temperate needleleaved evergreen tree	TeNeEv
Temperate broadleaved evergreen tree	TeBrEv
Temperate broadleaved summergreen tree	TeBrDe
Boreal needleleaved evergreen tree	BoNeEv
Boreal broadleaved summergreen tree	BoBrDe
Boreal needleleaved summergreen tree	BoNeDe
Tropical herbaceous	TrHe
Temperate herbaceous	TeHe
Polar herbaceous	PoHe
C3 flood tolerant grasses	C3gr
Temperate cereals	TeCe
Tropical cereals	TrCe
Temperate roots	TeRo
Tropical roots	TrRo
Sunflower	SunFl
Soy-bean	Soy
Groundnut	GrNu
Rapeseed	Rape
Sugar-cane	SuCa

https://doi.org/10.5194/egusphere-2025-6210
Preprint. Discussion started: 22 January 2026

Author contributions. SiS conceived and developed the model, performed the analyses, and led the writing of the manuscript. DH and WvB co-developed the model and provided expert guidance on the mathematical methods. All co-authors offered substantial feedback on successive drafts and contributed to the design and interpretation of the process evaluation.

Competing interests. The authors declare that they have no conflict of interest. CM is member of the editorial board of GMD.

Acknowledgements. SO was supported by the Conservation International Foundation, grant number CI-114129 and from the Future of Life Institute through the CODEC project.

https://doi.org/10.5194/egusphere-2025-6210
Preprint. Discussion started: 22 January 2026

References

State of Food and Agriculture. Biofuels: prospects, risks and opportunities, FAO, http://www.fao.org/docrep/011/i0100e/i0100e00.htm.

GEOCARBON Global Forest Aboveground Biomass (Mg/ha), UNEP/GRID Geneva GeoNetwork, https://datacore-gn.unepgrid.ch/geonetwork/srv/api/records/5e695176-266d-4697-bc06-c2d9196845b4, global forest AGB map produced in the EU FP7 GEOCARBON project by combining Avitabile et al. (2016; pan-tropics) and Santoro et al. (2015; northern hemisphere) products, 2014.

Alexiades, V. and Solomon, A.: Mathematical Modeling Of Melting And Freezing Processes, Hemisphere, 1993.

Bartlett, K. B. and Harriss, R. C.: Review and assessment of methane emissions from wetlands, Chemosphere, 26, 261–320, https://doi.org/10.1016/0045-6535(93)90427-7, 1992.

Beck, H. E., van Dijk, A. I. J. M., Miralles, D. G., de Jeu, R. A. M., (Sampurno) Bruijnzeel, L. A., McVicar, T. R., and Schellekens, J.: Global patterns in base flow index and recession based on streamflow observations from 3394 catchments, Water Resources Research, 49, 7843–7863, https://doi.org/10.1002/2013WR013918, 2013.

Beven, K. and Kirkby, M.: A physically-based variable contributing area model of basin hydrology., Hydrological Sciences Bulletin, 24(1), 43–69, 1979.

Bhatia, A. e. a.: Methane and nitrous oxide emissions from Indian rice paddies, and their global warming potential, Current Science, 105, 661–666, 2013.

Biemans, H., Haddeland, I., Kabat, P., Ludwig, F., Hutjes, R. W. a., Heinke, J., von Bloh, W., and Gerten, D.: Impact of reservoirs on river discharge and irrigation water supply during the 20th century, Water Resources Research, 47, W03 509, https://doi.org/10.1029/2009WR008929, 2011.

Bieniada, A., Green, S. M., Peacock, M., et al.: Steady and ebullitive methane fluxes from active, restored and unrestored fens in a hemiboreal region, Ecological Engineering, 164, 106 209, https://doi.org/10.1016/j.ecoleng.2021.106209, quantified CH4 ebullition vs diffusion; vascular cover (reed, sedge) strongly affects ebullition fraction., 2021.

Bloom, A., Bowman, K., Lee, M., Turner, A., SchroederR, R., Worden, J., Weidner, R., McDonald, K., and Jacob, D.: CMS: Global 0.5-deg Wetland Methane Emissions and Uncertainty (WetCHARTs v1.0), https://doi.org/10.3334/ORNLDAAC/1502, 2017a.

Bloom, A. A., Bowman, K. W., Lee, M., Turner, A. J., Schroeder, R., Worden, J. R., Weidner, R., McDonald, K. C., and Jacob, D. J.: A global wetland methane emissions and uncertainty dataset for atmospheric chemical transport models (WetCHARTs version 1.0), Geoscientific Model Development, 10, 2141–2156, https://doi.org/10.5194/gmd-10-2141-2017, 2017b.

Bruhwiler, L. M. P., Basu, S., Bergamaschi, P., Bousquet, P., Dlugokencky, E., Houweling, S., Janardanan, R., Miller, S., Pandey, S., Prigent, C., et al.: CarbonTracker-CH_4: An assimilation system for estimating emissions of atmospheric methane, Atmospheric Chemistry and Physics, 14, 8269–8293, https://doi.org/10.5194/acp-14-8269-2014, 2014.

Christen, E. W., Chung, S.-O., and Quayle, W.: Simulating the fate of molinate in rice paddies using the RICEWQ model, Agricultural Water Management, 85, 38–46, https://doi.org/10.1016/j.agwat.2006.03.008, 2006.

Clapp, R. B. and Hornberger, G. M.: Empirical equations for some soil hydraulic properties, Water Resour. Res., 14, 601–604, https://doi.org/10.1029/wr014i004p00601, 1978.

https://doi.org/10.5194/egusphere-2025-6210
Preprint. Discussion started: 22 January 2026

Collier, N., Hoffman, F. M., Lawrence, D. M., Keppel-Aleks, G., Koven, C. D., Riley, W. J., Randerson, J. T., Swenson, S. C., Thornton, P. E., Wieder, W. R., Xu, C., Yang, X., and Zeng, X.: The International Land Model Benchmarking (ILAMB) System: Design, Theory, and Implementation, Journal of Advances in Modeling Earth Systems, 10, 2731–2750, https://doi.org/10.1029/2018MS001354, 2018.

Colmer, T. D.: Long-distance transport of gases in plants: a perspective on internal aeration and radial oxygen loss from roots, Plant, Cell & Environment, 26, 17–36, https://doi.org/10.1046/j.1365-3040.2003.00846.x, 2003.

Conrad, R.: Soil microorganisms as controllers of atmospheric trace gases (H2, CO, CH4, OCS, N2O, and NO), Microbiological Reviews, 60, 609–640, https://doi.org/10.1128/mr.60.4.609-640.1996, 1996.

Cucchi, M., Weedon, G. P., Amici, A., Bellouin, N., Lange, S., Müller Schmied, H., Hersbach, H., and Buontempo, C.: WFDE5: bias-adjusted ERA5 reanalysis data for impact studies, Earth System Science Data, 12, 2097–2120, https://doi.org/10.5194/essd-12-2097-2020, 2020.

D. Gerten, S. Schaphoff, M. Bonsch, A. Popp, P. Holden, C. Wallace, K. Hiscock, T. Osborn; ed. N. Edwards, B. Pizzileo: Enhancing Robustness and Model Integration for The Assessment of Global Environmental Change, https://arquivo.pt/wayback/20160421111120/http://ermitage.cs.man.ac.uk/?q=node/52, grant Agreement No. 265170; archived at Arquivo.pt.

Duval, B. and Goodwin, S.: Methane production and release from two New England peatlands, International Microbiology, 3, 89–96, 2000.

Döll, P. and Fiedler, K.: Global-scale modeling of groundwater recharge, Hydrology and Earth System Sciences, 12, 863–885, https://doi.org/10.5194/hess-12-863-2008, 2008.

Döll, P., Douville, H., Güntner, A., Schmied, H. M., and Wada, Y.: Modelling freshwater resources at the global scale: Challenges in integrating hydrological components, Surveys in Geophysics, 37, 195–221, https://doi.org/10.1007/s10712-015-9343-1, 2016.

EPA: Global Anthropogenic Non-CO2 Greenhouse Gas Emissions: 1990–2030, Report EPA 430-R-12-006, U.S. Environmental Protection Agency (EPA), Washington, D.C., https://www.epa.gov/global-mitigation-non-co2-greenhouse-gases/global-non-co2-ghg-emissions-1990-2030, accessed 2025-12-02, 2012.

FAO: AQUASTAT database - Food and Agriculture Organization of the United Nations (FAO), http://www.fao.org/nr/water/aquastat/data/query/index.html?lang=en, 2014.

FAO: AQUASTAT database, Food and Agriculture Organization of the United Nations, Rome, http://www.fao.org/nr/water/aquastat/data/query/index.html?lang=en, accessed 2020-04-17, 2020a.

FAO: FAOSTAT database, Food and Agriculture Organization of the United Nations, Rome, http://www.fao.org/faostat/en/, accessed 2020-01-27, 2020b.

FAO: FAOSTAT Emissions Data, https://www.fao.org/faostat/en/#data/GT, 2020c.

FAO/IIASA/ISRIC/ISSCAS/JRC: Harmonized World Soil Database (version 1.21), FAO, Rome, Italy and IIASA, Laxenburg, Austria, https://iiasa.ac.at/web/home/research/researchPrograms/water/HWSD.html, accessed 2021-03-11, 2012.

Flörke, M., Kynast, E., Bärlund, I., Eisner, S., Wimmer, F., and Alcamo, J.: Domestic and industrial water uses of the past 60 years as a mirror of socio-economic development: A global simulation study, Global Environmental Change, 23, 144–156, https://doi.org/10.1016/j.gloenvcha.2012.10.018, 2013.

https://doi.org/10.5194/egusphere-2025-6210
Preprint. Discussion started: 22 January 2026

Friedlingstein, P., O'Sullivan, M., Jones, M. W., Andrew, R. M., Bakker, D. C. E., Hauck, J., Landschützer, P., Le Quéré, C., Luijkx, I. T., Peters, G. P., Peters, W., Pongratz, J., Schwingshackl, C., Sitch, S., Canadell, J. G., Ciais, P., Jackson, R. B., Alin, S. R., Anthoni, P., Barbero, L., Bates, N. R., Becker, M., Bellouin, N., Decharme, B., Bopp, L., Brasika, I. B. M., Cadule, P., Chamberlain, M. A., Chandra, N., Chau, T.-T.-T., Chevallier, F., Chini, L. P., Cronin, M., Dou, X., Enyo, K., Evans, W., Falk, S., Feely, R. A., Feng, L., Ford, D. J., Gasser, T., Ghattas, J., Gkritzalis, T., Grassi, G., Gregor, L., Gruber, N., Gürses, O., Harris, I., Hefner, M., Heinke, J., Houghton, R. A., Hurtt, G. C., Iida, Y., Ilyina, T., Jacobson, A. R., Jain, A., Jarníková, T., Jersild, A., Jiang, F., Jin, Z., Joos, F., Kato, E., Keeling, R. F., Kennedy, D., Klein Goldewijk, K., Knauer, J., Korsbakken, J. I., Körtzinger, A., Lan, X., Lefèvre, N., Li, H., Liu, J., Liu, Z., Ma, L., Marland, G., Mayot, N., McGuire, P. C., McKinley, G. A., Meyer, G., Morgan, E. J., Munro, D. R., Nakaoka, S.-I., Niwa, Y., O'Brien, K. M., Olsen, A., Omar, A. M., Ono, T., Paulsen, M., Pierrot, D., Pocock, K., Poulter, B., Powis, C. M., Rehder, G., Resplandy, L., Robertson, E., Rödenbeck, C., Rosan, T. M., Schwinger, J., Séférian, R., Smallman, T. L., Smith, S. M., Sospedra-Alfonso, R., Sun, Q., Sutton, A. J., Sweeney, C., Takao, S., Tans, P. P., Tian, H., Tilbrook, B., Tsujino, H., Tubiello, F., van der Werf, G. R., van Ooijen, E., Wanninkhof, R., Watanabe, M., Wimart-Rousseau, C., Yang, D., Yang, X., Yuan, W., Yue, X., Zaehle, S., Zeng, J., and Zheng, B.: Global Carbon Budget 2023, Earth System Science Data, 15, 5301–5369, https://doi.org/10.5194/essd-15-5301-2023, 2023.

Godoy, A. R., Castanheira, B. G., Paiva, R. C. D., and Collischonn, W.: Global river discharge reanalysis based on multiple observation datasets, Water Resources Research, 57, e2020WR028 427, https://doi.org/10.1029/2020WR028427, 2021.

Good, S. P., Noone, D., and Bowen, G.: Hydrologic connectivity constrains partitioning of global terrestrial water fluxes, Science, 349, 175–177, https://doi.org/10.1126/science.aaa5931, 2015.

Gumbricht, T., Román-Cuesta, R., Verchot, L., Herold, M., Wittmann, F; Householder, E., Herold, N., and Murdiyarso, D.: Tropical and Subtropical Wetland Distribution, https://doi.org/10.17528/CIFOR/DATA.00058, sWAMP, 2017.

Gupta, K., Kumar, R., Baruah, K. K., Hazarika, S., Karmakar, S., and Bordoloi, N.: Greenhouse gas emission from rice fields: a review from Indian context, Environmental Science and Pollution Research, 28, 30 551–30 572, https://doi.org/10.1007/s11356-021-13935-1, 2021.

Haggard, B., Moore Jr, P., and Brye, K.: Effect of slope on runoff from a small variable-slope box, Journal of Environmental hydrology, 13, 25–45, 2005.

Harper, K. L., Lamarche, C., Hartley, A., Peylin, P., Ottlé, C., Bastrikov, V., San Martín, R., Bohnenstengel, S. I., Kirches, G., Boettcher, M., Shevchuk, R., Brockmann, C., and Defourny, P.: A 29-year time series of annual 300 m resolution plant-functional-type maps for climate models, Earth System Science Data, 15, 1465–1499, https://doi.org/10.5194/essd-15-1465-2023, 2023.

He, J., Naik, V., and Horowitz, L. W.: Hydroxyl Radical (OH) Response to Meteorological Forcing and Implication for the Methane Budget, Geophysical Research Letters, 48, e2021GL094 140, https://doi.org/10.1029/2021GL094140, e2021GL094140 2021GL094140, 2021.

Heinke, J.: A livestock density input for LPJmL5.5, https://doi.org/10.5281/zenodo.14946695, 2025.

Heinke, J., Rolinski, S., and Müller, C.: Modelling the role of livestock grazing in C and N cycling in grasslands with LPJmL5.0-grazing, Geoscientific Model Development, 16, 2455–2475, https://doi.org/10.5194/gmd-16-2455-2023, 2023.

https://doi.org/10.5194/egusphere-2025-6210
Preprint. Discussion started: 22 January 2026

Hu, Q., Li, J., Xie, H., Huang, Y., Canadell, J. G., Yuan, W., Wang, J., Zhang, W., Yu, L., Li, S., Lu, X., Li, T., and Qin, Z.: Global methane emissions from rice paddies: CH4MOD model development and application, iScience, 27, 111 237, https://doi.org/https://doi.org/10.1016/j.isci.2024.111237, 2024.

Huang, Z., Hejazi, M., Li, X., Tang, Q., Vernon, C., Leng, G., Liu, Y., Döll, P., Eisner, S., Gerten, D., Hanasaki, N., and Wada, Y.: Reconstruction of global gridded monthly sectoral water withdrawals for 1971–2010 and analysis of their spatiotemporal patterns, Hydrology and Earth System Sciences, 22, 2117–2133, https://doi.org/10.5194/hess-22-2117-2018, 2018.

Hugelius, G., Loisel, J., Chadburn, S., Jackson, R. B., Jones, M., MacDonald, G. M., Marushchak, M., Olefeldt, D., Packalen, M., Siewert, M. B., Treat, C., and Turetsky, M.: Large stocks of peatland carbon and nitrogen are vulnerable to permafrost thaw, Proceedings of the National Academy of Sciences, 117, 20 438–20 446, https://doi.org/10.1073/pnas.1916387117, 2020.

Hurtt, G. C., Chini, L., Sahajpal, R., Frolking, S., Bodirsky, B. L., Calvin, K., Doelman, J. C., Fisk, J., Fujimori, S., Klein Goldewijk, K., Hasegawa, T., Havlik, P., Heinimann, A., Humpenöder, F., Jungclaus, J., Kaplan, J. O., Kennedy, J., Krisztin, T., Lawrence, D., Lawrence, P., Ma, L., Mertz, O., Pongratz, J., Popp, A., Poulter, B., Riahi, K., Shevliakova, E., Stehfest, E., Thornton, P., Tubiello, F. N., van Vuuren, D. P., and Zhang, X.: Harmonization of global land use change and management for the period 850–2100 (LUH2) for CMIP6, Geosci. Model Dev., 13, 5425–5464, https://doi.org/10.5194/gmd-13-5425-2020, data available at https://luh.umd.edu/, accessed 2021-07-08, 2020.

IIASA/FAO: Global Agro-ecological Zones (GAEZv3.0), IIASA, Laxenburg, Austria and FAO, Rome, Italy, http://www.gaez.iiasa.ac.at/, accessed 2020-07-17, 2012.

Jasechko, S., Sharp, Z. D., Gibson, J. J., Birks, S. J., Yi, Y., and Fawcett, P. J.: Terrestrial water fluxes dominated by transpiration, Nature, 496, 347–350, https://doi.org/10.1038/nature11983, 2013.

Jobbagy, E. G. and Jackson, R. B.: The Vertical Distribution of Soil Organic Carbon and Its Relation to Climate and Vegetation, Ecological Applications, 10, 423–436, http://www.jstor.org/stable/2641104, articleType: research-article / Full publication date: Apr., 2000 / Copyright © 2000 Ecological Society of America, 2000.

Jung, M., Reichstein, M., Margolis, H. A., Cescatti, A., Richardson, A. D., Arain, M. A., Arneth, A., Bernhofer, C., Bonal, D., Chen, J., Gianelle, D., Gobron, N., Kiely, G., Kutsch, W., Lasslop, G., Law, B. E., Lindroth, A., Merbold, L., Montagnani, L., Moors, E. J., Papale, D., Sottocornola, M., Vaccari, F., and Williams, C.: Global patterns of land-atmosphere fluxes of carbon dioxide, latent heat, and sensible heat derived from eddy covariance, satellite, and meteorological observations, Journal of Geophysical Research: Biogeosciences, 116, n/a–n/a, https://doi.org/10.1029/2010JG001566, 2011.

Jung, M., Schwalm, C., Migliavacca, M., Walther, S., Camps-Valls, G., Koirala, S., Anthoni, P., Besnard, S., Bodesheim, P., Carvalhais, N., Chevallier, F., Gans, F., Goll, D. S., Haverd, V., Köhler, P., Ichii, K., Jain, A. K., Liu, J., Lombardozzi, D., Nabel, J. E. M. S., Nelson, J. A., O'Sullivan, M., Pallandt, M., Papale, D., Peters, W., Pongratz, J., Rödenbeck, C., Sitch, S., Tramontana, G., Walker, A., Weber, U., and Reichstein, M.: Scaling carbon fluxes from eddy covariance sites to globe: synthesis and evaluation of the FLUXCOM approach, Biogeosciences, 17, 1343–1365, https://doi.org/10.5194/bg-17-1343-2020, 2020.

Jägermeyr, J., Müller, C., Minoli, S., Ray, D., and Siebert, S.: GGCMI Phase 3 crop calendar, https://doi.org/10.5281/zenodo.5062513, 2021.

Kaplan, J.: A composite map of global wetland distribution at 0.5 degree resolution, https://doi.org/10.5281/zenodo.18274983, 2007.

https://doi.org/10.5194/egusphere-2025-6210
Preprint. Discussion started: 22 January 2026

Kaur, G., Singh, G., Motavalli, P. P., Nelson, K. A., Orlowski, J. M., and Golden, B. R.: Impacts and management strategies for crop production in waterlogged or flooded soils: A review, Agronomy Journal, 112, 1475–1501, 2020.

Kellndorfer, J., Walker, W., Kirsch, K., Fiske, G., Bishop, J., LaPoint, E., Hoppus, M., and Westfall, J.: NACP Aboveground Biomass and Carbon Baseline Data (NBCD 2000), U.S.A., 2000, https://doi.org/10.3334/ORNLDAAC/1081, 2012.

Khvorostyanov, D. V., Krinner, G., Ciais, P., M. Heimann, and Zimov, S. A.: Vulnerability of permafrost carbon to global warming. Part I: model description and role of heat generated by organic matter decomposition, Tellus B, 60, 250–264, http://dx.doi.org/10.1111/j.1600-0889.2007.00333.x, 2008.

Kim, H.: Global Soil Wetness Project Phase 3 Atmospheric Boundary Conditions (Experiment 1) [Data set], https://doi.org/10.20783/DIAS.501, 2017.

Kirschke, S., Bousquet, P., Ciais, P., Saunois, M., Canadell, J. G., Dlugokencky, E. J., Bergamaschi, P., Bergmann, D., Blake, D. R., Bruhwiler, L., Cameron-Smith, P., Castaldi, S., Chevallier, F., Feng, L., Fraser, A., Heimann, M., Hodson, E. L., Houweling, S., Josse, B., Fraser, P. J., Krummel, P. B., Lamarque, J.-F., Langenfelds, R. L., Le Quere, C., Naik, V., O'Doherty, S., Palmer, P. I., Pison, I., Plummer, D., Poulter, B., Prinn, R. G., Rigby, M., Ringeval, B., Santini, M., Schmidt, M., Shindell, D. T., Simpson, I. J., Spahni, R., Steele, L. P., Strode, S. A., Sudo, K., Szopa, S., van der Werf, G. R., Voulgarakis, A., van Weele, M., Weiss, R. F., Williams, J. E., and Zeng, G.: Three decades of global methane sources and sinks, Nature Geosci, 6, 813–823, http://dx.doi.org/10.1038/ngeo1955, 2013.

Klein Goldewijk, K., Beusen, A., Doelman, J., and Stehfest, E.: Anthropogenic land use estimates for the Holocene - HYDE 3.2, Earth Syst. Sci. Data, 9, 927–953, https://doi.org/10.5194/essd-9-927-2017, data available at https://www.pbl.nl/en/image/links/hyde, accessed 2017-10-25, 2017a.

Klein Goldewijk, K., Beusen, A., Doelman, J., and Stehfest, E.: Anthropogenic land use estimates for the Holocene – HYDE 3.2, Earth System Science Data, 9, 927–953, https://doi.org/10.5194/essd-9-927-2017, 2017b.

Kleinen, T., Brovkin, V., and Schuldt, R. J.: A dynamic model of wetland extent and peat accumulation: results for the Holocene, Biogeosciences, 9, 235–248, https://doi.org/10.5194/bg-9-235-2012, 00017, 2012.

Lammers, R. B., Shiklomanov, A. I., Vörösmarty, C. J., Fekete, B. M., and Peterson, B. J.: Assessment of contemporary Arctic river runoff based on observational discharge records, Journal of Geophysical Research: Atmospheres, 106, 3321–3334, https://doi.org/10.1029/2000JD900444, 2001.

Lammers, R. B., Shiklomanov, A. I., Vörösmarty, C. J., Fekete, B. M., and Peterson, B. J.: R-ArcticNet, A Regional Hydrographic Data Network for the Pan-Arctic Region (ISO-image of CD-ROM), https://doi.org/10.1594/PANGAEA.859422, accessed 2026-01-14, 2016.

Lange, S., Menz, C., Gleixner, S., Cucchi, M., Weedon, G. P., Amici, A., Bellouin, N., Schmied, H. M., Hersbach, H., Buontempo, C., and Cagnazzo, C.: WFDE5 over land merged with ERA5 over the ocean (W5E5 v2.0), https://doi.org/10.48364/ISIMIP.342217, 2021.

Lange, S., Mengel, M., Treu, S., and Büchner, M.: ISIMIP3a atmospheric climate input data, https://doi.org/10.48364/ISIMIP.982724.2, 2023.

Lawrence, D. and Slater, A.: Incorporating organic soil into a global climate model, Climate Dynamics, 30, 145–160, http://dx.doi.org/10.1007/s00382-007-0278-1, 10.1007/s00382-007-0278-1, 2008.

Lee, H., Schuur, E. A., Inglett, K. S., Lavoie, M., and Chanton, J. P.: The rate of permafrost carbon release under aerobic and anaerobic conditions and its potential effects on climate, Global Change Biology, 18, 515–527, 2012.

https://doi.org/10.5194/egusphere-2025-6210
Preprint. Discussion started: 22 January 2026

Lehner, B. and Döll, P.: Development and validation of a global database of lakes, reservoirs and wetlands, J. Hydrol., 296, 1–22, https://doi.org/10.1016/j.jhydrol.2004.03.028, data available at https://www.worldwildlife.org/pages/global-lakes-and-wetlands-database, accessed 2018-08-15, 2004.

Lehner, B., Liermann, C. R., Revenga, C., Vörösmarty, C., Fekete, B., Crouzet, P., Döll, P., Endejan, M., Frenken, K., and Magome, J.: High-resolution mapping of the world's reservoirs and dams for sustainable river-flow management, Frontiers in Ecology and the Environment, 9, 494–502, 2011.

Li, Y., Shang, J., Zhang, C., Zhang, W., Niu, L., Wang, L., and Zhang, H.: The role of freshwater eutrophication in greenhouse gas emissions: A review, Science of The Total Environment, 768, 144 582, https://doi.org/10.1016/j.scitotenv.2020.144582, 2021.

Lutz, F., Herzfeld, T., Heinke, J., Rolinski, S., Schaphoff, S., Von Bloh, W., Stoorvogel, J. J., and Müller, C.: Simulating the effect of tillage practices with the global ecosystem model LPJmL (version 5.0-tillage), Geoscientific Model Development, 12, 2419–2440, 2019.

Mengel, M., Treu, S., Lange, S., and Frieler, K.: ATTRICI v1.1 – counterfactual climate for impact attribution, Geoscientific Model Development, 14, 5269–5284, https://doi.org/10.5194/gmd-14-5269-2021, 2021.

Mohan, C., Western, A. W., Wei, Y., and Saft, M.: Predicting groundwater recharge for varying land cover and climate conditions – a global meta-study, Hydrology and Earth System Sciences, 22, 2689–2703, https://doi.org/10.5194/hess-22-2689-2018, 2018.

Monfreda, C., Ramankutty, N., and Foley, J. a.: Farming the planet: 2. Geographic distribution of crop areas, yields, physiological types, and net primary production in the year 2000, Global Biogeochem. Cycles, 22, GB1022, https://doi.org/10.1029/2007GB002947, data available from http://www.earthstat.org/, accessed 2018-10-30, 2008.

Moore, T. R., Roulet, N. T., and Waddington, J. M.: Uncertainty in predicting the effect of climatic change on the carbon cycling of Canadian peatlands, Climatic Change, 40, 229–245, https://doi.org/10.1023/A:1005439401383, 2011.

Mora, B., Tsendbazar, N.-E., Herold, M., and Arino, O.: Global land cover mapping: Current status and future trends, Land use and land cover mapping in Europe: practices & trends, pp. 11–30, 2014.

Muehleisen, A. J., Schwartz, N. B., Stump, S. M., and Staver, A. C.: Rainfall variability and deciduous-evergreen coexistence in tropical forests, Theoretical Ecology, 17, 255–268, https://doi.org/10.1007/s12080-024-00588-2, 2024.

Mueller, N.: Crop-specific global fertilizer application rates from "Closing yield gaps through nutrient and water management", Version 1, Zenodo, https://doi.org/10.5281/zenodo.5260732, accessed 2022-03-08, 2012.

Mueller, N. D., Gerber, J. S., Johnston, M., Ray, D. K., Ramankutty, N., and Foley, J. A.: Closing yield gaps through nutrient and water management, Nature, 490, 254–257, https://doi.org/10.1038/nature11420, 2012.

Müller Schmied, H., Cáceres, D., Eisner, S., Flörke, M., Herbert, C., Niemann, C., Peiris, T. A., Popat, E., Portmann, F. T., Reinecke, R., Schumacher, M., Shadkam, S., Telteu, C.-E., Trautmann, T., and Döll, P.: The global water resources and use model WaterGAP v2.2d: model description and evaluation, Geoscientific Model Development, 14, 1037–1079, https://doi.org/10.5194/gmd-14-1037-2021, 2021.

Murguia-Flores, F., Arndt, S., Ganesan, A. L., Murray-Tortarolo, G., and Hornibrook, E. R. C.: Soil Methanotrophy Model (MeMo v1.0): a process-based model to quantify global uptake of atmospheric methane by soil, Geoscientific Model Development, 11, 2009–2032, https://doi.org/10.5194/gmd-11-2009-2018, 2018.

https://doi.org/10.5194/egusphere-2025-6210
Preprint. Discussion started: 22 January 2026

Nascimento, H. L. B., Pedreira, B. C., Sollenberger, L. E., Pereira, D. H., Magalhães, C. A. S., and Chizzotti, F. H. M.: Herbage accumulation, canopy structure and tiller morphology of marandu palisadegrass growing in open pasture and in silvopasture, Agroforestry Systems, 95, 339–352, https://doi.org/10.1007/s10457-020-00590-7, 2021.

Niu, G.-Y. and Yang, Z.-L.: Effects of frozen soil on snowmelt runoff and soil water storage at a continental scale, Journal of Hydrometeorology, 7, 937–952, 2006.

Niu, G.-Y., Yang, Z.-L., Dickinson, R. E., and Gulden, L. E.: A simple TOPMODEL-based runoff parameterization (SIMTOP) for use in global climate models, Journal of Geophysical Research: Atmospheres, 110, 2005.

NOAA Global Monitoring Laboratory: Trends in Atmospheric Methane (CH_4), https://gml.noaa.gov/ccgg/trends_ch4/, accessed: 2025-07-10, 2025.

NOAA Global Monitoring Laboratory: CarbonTracker-CH_4 Flux Histograms – Global Region, https://gml.noaa.gov/ccgg/carbontracker-ch4/fluxhistograms.php?region=GLOB, accessed: 2025-07-10, n.d.

Oleson, K. W., Lawrence, D. M., Bonan, G. B., Drewniak, B., Huang, M., Koven, C. D., Levis, S., Li, F., Riley, W. J., Subin, Z. M., Swenson, S. C., Thornton, P. E., Bozbiyik, A., Fisher, R., Kluzek, E., Lamarque, J.-F., Lawrence, P. J., Muszala, S., Ricciuto, D. M., Sacks, W. J., Sun, Y., Tang, J., and Yang, Z.-L.: Technical Description of version 4.5 of the Community Land Model (CLM4.5), NCAR Technical Note NCAR/TN-503+STR, National Center for Atmospheric Research (NCAR), Boulder, Colorado, USA, https://doi.org/10.5065/D6RR1W7M, nCAR Earth System Laboratory, Climate and Global Dynamics Division, 2013.

Ostberg, S., Müller, C., Heinke, J., and Schaphoff, S.: LandInG 1.0: a toolbox to derive input datasets for terrestrial ecosystem modelling at variable resolutions from heterogeneous sources, Geoscientific Model Development, 16, 3375–3406, https://doi.org/10.5194/gmd-16-3375-2023, 2023.

Pan, S., Pan, N., Tian, H., Friedlingstein, P., Sitch, S., Shi, H., Arora, V. K., Haverd, V., Jain, A. K., Kato, E., Lienert, S., Lombardozzi, D., Nabel, J. E. M. S., Ottlé, C., Poulter, B., Zaehle, S., and Running, S. W.: Evaluation of global terrestrial evapotranspiration using state-of-the-art approaches in remote sensing, machine learning and land surface modeling, Hydrology and Earth System Sciences, 24, 1485–1509, https://doi.org/10.5194/hess-24-1485-2020, 2020.

Parolin, P. and Wittmann, F.: Struggle in the flood: tree responses to flooding stress in four tropical floodplain systems, AoB PLANTS, 2010, plq003, https://doi.org/10.1093/aobpla/plq003, 2010.

Pastorello, G., Trotta, C., Canfora, E., Chu, H., Christianson, D., Cheah, Y.-W., Poindexter, C., Chen, J., Elbashandy, A., Humphrey, M., Isaac, P., Polidori, D., Ribeca, A., van Ingen, C., Zhang, L., Amiro, B., Ammann, C., Arain, M. A., ArdÃ¶, J., Arkebauer, T., Arndt, S. K., Arriga, N., Aubinet, M., Aurela, M., Baldocchi, D., Barr, A., Beamesderfer, E., Marchesini, L. B., Bergeron, O., Beringer, J., Bernhofer, C., Berveiller, D., Billesbach, D., Black, T. A., Blanken, P. D., Bohrer, G., Boike, J., Bolstad, P. V., Bonal, D., Bonnefond, J.-M., Bowling, D. R., Bracho, R., Brodeur, J., BrÃ¼mmer, C., Buchmann, N., Burban, B., Burns, S. P., Buysse, P., Cale, P., Cavagna, M., Cellier, P., Chen, S., Chini, I., Christensen, T. R., Cleverly, J., Collalti, A., Consalvo, C., Cook, B. D., Cook, D., Coursolle, C., Cremonese, E., Curtis, P. S., Da Andrea, E., da Rocha, H., Dai, X., Davis, K. J., De Cinti, B., de Grandcourt, A., De Ligne, A., De Oliveira, R. C., Delpierre, N., Desai, A. R., Di Bella, C. M., di Tommasi, P., Dolman, H., Domingo, F., Dong, G., Dore, S., Duce, P., DufrÃªne, E., Dunn, A., Duarek, J., Eamus, D., Eichelmann, U., ElKhidir, H. A. M., Eugster, W., Ewenz, C. M., Ewers, B., Famulari, D., Fares, S., Feigenwinter, I., Feitz, A., Fensholt, R., Filippa, G., Fischer, M., Frank, J., Galvagno, M., Gharun, M., Gianelle, D., Gielen, B., Gioli, B., Gitelson, A., Goded, I., Goeckede, M., Goldstein, A. H., Gough, C. M., Goulden, M. L., Graf, A., Griebel, A., Gruening,

https://doi.org/10.5194/egusphere-2025-6210
Preprint. Discussion started: 22 January 2026

C., GrÃ¼nwald, T., Hammerle, A., Han, S., Han, X., Hansen, B. U., Hanson, C., Hatakka, J., He, Y., Hehn, M., Heinesch, B., Hinko-Najera, N., HÃ¶rtnagl, L., Hutley, L., Ibrom, A., Ikawa, H., Jackowicz-Korczynski, M., JanouÅ¡, D., Jans, W., Jassal, R., Jiang, S., Kato, T., Khomik, M., Klatt, J., Knohl, A., Knox, S., Kobayashi, H., Koerber, G., Kolle, O., Kosugi, Y., Kotani, A., Kowalski, A., Kruijt, B., Kurbatova, J., Kutsch, W. L., Kwon, H., Launiainen, S., Laurila, T., Law, B., Leuning, R., Li, Y., Liddell, M., Limousin, J.-M., Lion, M., Liska, A. J., Lohila, A., LÃ³pez-Ballesteros, A., LÃ³pez-Blanco, E., Loubet, B., Loustau, D., Lucas-Moffat, A., LÃ¼ers, J., Ma, S., Macfarlane, C., Magliulo, V., Maier, R., Mammarella, I., Manca, G., Marcolla, B., Margolis, H. A., Marras, S., Massman, W., Mastepanov, M., Matamala, R., Matthes, J. H., Mazzenga, F., McCaughey, H., McHugh, I., McMillan, A. M. S., Merbold, L., Meyer, W., Meyers, T., Miller, S. D., Minerbi, S., Moderow, U., Monson, R. K., Montagnani, L., Moore, C. E., Moors, E., Moreaux, V., Moureaux, C., Munger, J. W., Nakai, T., Neirynck, J., Nesic, Z., Nicolini, G., Noormets, A., Northwood, M., Nosetto, M., Nouvellon, Y., Novick, K., Oechel, W., Olesen, J. E., Ourcival, J.-M., Papuga, S. A., Parmentier, F.-J., Paul-Limoges, E., Pavelka, M., Peichl, M., Pendall, E., Phillips, R. P., Pilegaard, K., Pirk, N., Posse, G., Powell, T., Prasse, H., Prober, S. M., Rambal, S., Rannik, A., Raz-Yaseef, N., Reed, D., de Dios, V. R., Restrepo-Coupe, N., Reverter, B. R., Roland, M., Sabbatini, S., Sachs, T., Saleska, S. R., Sanchez-Cäete, E. P., Sanchez-Mejia, Z. M., Schmid, H. P., Schmidt, M., Schneider, K., Schrader, F., Schroder, I., Scott, R. L., SedlÃ¡k, P., Serrano-Ortäz, P., Shao, C., Shi, P., Shironya, I., Siebicke, L., Å igut, L., Silberstein, R., Sirca, C., Spano, D., Steinbrecher, R., Stevens, R. M., Sturtevant, C., Suyker, A., Tagesson, T., Takanashi, S., Tang, Y., Tapper, N., Thom, J., Tiedemann, F., Tomassucci, M., Tuovinen, J.-P., Urbanski, S., Valentini, R., van der Molen, M., van Gorsel, E., van Huissteden, K., Varlagin, A., Verfaillie, J., Vesala, T., Vincke, C., Vitale, D., Vygodskaya, N., Walker, J. P., Walter-Shea, E., Wang, H., Weber, R., Westermann, S., Wille, C., Wofsy, S., Wohlfahrt, G., Wolf, S., Woodgate, W., Li, Y., Zampedri, R., Zhang, J., Zhou, G., Zona, D., Agarwal, D., Biraud, S., Torn, M., and Papale, D.: The FLUXNET2015 dataset and the ONEFlux processing pipeline for eddy covariance data, Scientific Data, 7, 225, https://doi.org/10.1038/s41597-020-0534-3, 2020.

Pazhanivelan, S., Sudarmanian, N. S., Geethalakshmi, V., Deiveegan, M., Ragunath, K., Sivamurugan, A. P., and Shanmugapriya, P.: Assessing Methane Emissions from Rice Fields in Large Irrigation Projects Using Satellite-Derived Land Surface Temperature and Agronomic Flooding: A Spatial Analysis, Agriculture, 14, https://doi.org/10.3390/agriculture14030496, 2024.

Portmann, F. T., Siebert, S., and Döll, P.: MIRCA2000-Global monthly irrigated and rainfed crop areas around the year 2000: A new high-resolution data set for agricultural and hydrological modeling, Global Biogeochem. Cycles, 24, GB1011, https://doi.org/10.1029/2008GB003435, 2010a.

Portmann, F. T., Siebert, S., and Döll, P.: MIRCA2000, Version 1.1 [Data set], Zenodo, https://doi.org/10.5281/zenodo.7422506, accessed 2018-03-19, 2010b.

Prestele, R., Alexander, P., Rounsevell, M. D. A., Arneth, A., Calvin, K., Doelman, J., Eitelberg, D. A., Engström, K., Fujimori, S., Hasegawa, T., Havlik, P., Humpenöder, F., Jain, A. K., Krisztin, T., Kyle, P., Meiyappan, P., Popp, A., Sands, R. D., Schaldach, R., Schüngel, J., Stehfest, E., Tabeau, A., Van Meijl, H., Van Vliet, J., and Verburg, P. H.: Hotspots of uncertainty in land-use and land-cover change projections: a global-scale model comparison, Global Change Biology, 22, 3967–3983, https://doi.org/https://doi.org/10.1111/gcb.13337, 2016.

Qian, H., Zhu, X., Huang, S., Linquist, B., Kuzyakov, Y., Wassmann, R., Minamikawa, K., Martinez-Eixarch, M., Yan, X., Zhou, F., Sander, B. O., Zhang, W., Shang, Z., Zou, J., Zheng, X., Li, G., Liu, Z., Wang, S., Ding, Y., van Groenigen,

https://doi.org/10.5194/egusphere-2025-6210
Preprint. Discussion started: 22 January 2026

K. J., and Jiang, Y.: Greenhouse gas emissions and mitigation in rice agriculture, Nature Reviews Earth & Environment, 4, 716–732, https://doi.org/10.1038/s43017-023-00482-1, 2023.

R-ArcticNET Project: R-ArcticNET v4.0 Available Data (Site Attributes and Discharge Tables), https://www.r-arcticnet.sr.unh.edu/v4.0/AllData/index.html, accessed 2026-01-14.

Riley, W., Subin, Z., Lawrence, D., Swenson, S., Torn, M., Meng, L., Mahowald, N., and Hess, P.: Barriers to predicting changes in global terrestrial methane fluxes: analyses using CLM4Me, a methane biogeochemistry model integrated in CESM, Biogeosciences, 8, 1925–1953, 2011.

Santoro, M., Cartus, O., Carvalhais, N., Rozendaal, D. M. A., Avitabile, V., Araza, A., de Bruin, S., Herold, M., Quegan, S., Rodríguez-Veiga, P., Balzter, H., Carreiras, J., Schepaschenko, D., Korets, M., Shimada, M., Itoh, T., Moreno Martínez, Á., Cavlović, J., Cazzolla Gatti, R., and others: The global forest above-ground biomass pool for 2010 estimated from high-resolution satellite observations, Earth System Science Data, 13, 3927–3950, https://doi.org/10.5194/essd-13-3927-2021, 2021.

Saunois, M., Bousquet, P., Poulter, B., Peregon, A., Ciais, P., Canadell, J. G., Dlugokencky, E. J., Etiope, G., Bastviken, D., Houweling, S., Janssens-Maenhout, G., Tubiello, F. N., Castaldi, S., Jackson, R. B., Alexe, M., Arora, V. K., Beerling, D. J., Bergamaschi, P., Blake, D. R., Brailsford, G., Brovkin, V., Bruhwiler, L., Crevoisier, C., Crill, P., Covey, K., Curry, C., Frankenberg, C., Gedney, N., Höglund-Isaksson, L., Ishizawa, M., Ito, A., Joos, F., Kim, H.-S., Kleinen, T., Krummel, P., Lamarque, J.-F., Langenfelds, R., Locatelli, R., Machida, T., Maksyutov, S., McDonald, K. C., Marshall, J., Melton, J. R., Morino, I., Naik, V., O'Doherty, S., Parmentier, F.-J. W., Patra, P. K., Peng, C., Peng, S., Peters, G. P., Pison, I., Prigent, C., Prinn, R., Ramonet, M., Riley, W. J., Saito, M., Santini, M., Schroeder, R., Simpson, I. J., Spahni, R., Steele, P., Takizawa, A., Thornton, B. F., Tian, H., Tohjima, Y., Viovy, N., Voulgarakis, A., van Weele, M., van der Werf, G. R., Weiss, R., Wiedinmyer, C., Wilton, D. J., Wiltshire, A., Worthy, D., Wunch, D., Xu, X., Yoshida, Y., Zhang, B., Zhang, Z., and Zhu, Q.: The global methane budget 2000–2012, Earth System Science Data, 8, 697–751, https://doi.org/10.5194/essd-8-697-2016, 2016.

Saunois, M., Stavert, A. R., Poulter, B., Bousquet, P., Canadell, J. G., Jackson, R. B., Raymond, P. A., Dlugokencky, E. J., Houweling, S., Patra, P. K., Ciais, P., Arora, V. K., Bastviken, D., Bergamaschi, P., Blake, D. R., Brailsford, G., Bruhwiler, L., Carlson, K. M., Carrol, M., Castaldi, S., Chandra, N., Crevoisier, C., Crill, P. M., Covey, K., Curry, C. L., Etiope, G., Frankenberg, C., Gedney, N., Hegglin, M. I., Höglund-Isaksson, L., Hugelius, G., Ishizawa, M., Ito, A., Janssens-Maenhout, G., Jensen, K. M., Joos, F., Kleinen, T., Krummel, P. B., Langenfelds, R. L., Laruelle, G. G., Liu, L., Machida, T., Maksyutov, S., McDonald, K. C., McNorton, J., Miller, P. A., Melton, J. R., Morino, I., Müller, J., Murguia-Flores, F., Naik, V., Niwa, Y., Noce, S., O'Doherty, S., Parker, R. J., Peng, C., Peng, S., Peters, G. P., Prigent, C., Prinn, R., Ramonet, M., Regnier, P., Riley, W. J., Rosentreter, J. A., Segers, A., Simpson, I. J., Shi, H., Smith, S. J., Steele, L. P., Thornton, B. F., Tian, H., Tohjima, Y., Tubiello, F. N., Tsuruta, A., Viovy, N., Voulgarakis, A., Weber, T. S., van Weele, M., van der Werf, G. R., Weiss, R. F., Worthy, D., Wunch, D., Yin, Y., Yoshida, Y., Zhang, W., Zhang, Z., Zhao, Y., Zheng, B., Zhu, Q., Zhu, Q., and Zhuang, Q.: The Global Methane Budget 2000–2017, Earth System Science Data, 12, 1561–1623, https://doi.org/10.5194/essd-12-1561-2020, 2020.

Saunois, M., Martinez, A., Poulter, B., Zhang, Z., Raymond, P. A., Regnier, P., Canadell, J. G., Jackson, R. B., Patra, P. K., Bousquet, P., Ciais, P., Dlugokencky, E. J., Lan, X., Allen, G. H., Bastviken, D., Beerling, D. J., Belikov, D. A., Blake, D. R., Castaldi, S., Crippa, M., Deemer, B. R., Dennison, F., Etiope, G., Gedney, N., Höglund-Isaksson, L., Holgerson,

https://doi.org/10.5194/egusphere-2025-6210
Preprint. Discussion started: 22 January 2026

M. A., Hopcroft, P. O., Hugelius, G., Ito, A., Jain, A. K., Janardanan, R., Johnson, M. S., Kleinen, T., Krummel, P. B., Lauerwald, R., Li, T., Liu, X., McDonald, K. C., Melton, J. R., Mühle, J., Müller, J., Murguia-Flores, F., Niwa, Y., Noce, S., Pan, S., Parker, R. J., Peng, C., Ramonet, M., Riley, W. J., Rocher-Ros, G., Rosentreter, J. A., Sasakawa, M., Segers, A., Smith, S. J., Stanley, E. H., Thanwerdas, J., Tian, H., Tsuruta, A., Tubiello, F. N., Weber, T. S., van der Werf, G. R., Worthy, D. E. J., Xi, Y., Yoshida, Y., Zhang, W., Zheng, B., Zhu, Q., Zhu, Q., and Zhuang, Q.: Global Methane Budget 2000–2020, Earth System Science Data, 17, 1873–1958, https://doi.org/10.5194/essd-17-1873-2025, 2025.

Schaphoff, S., Heyder, U., Ostberg, S., Gerten, D., Heinke, J., and Lucht, W.: Contribution of permafrost soils to the global carbon budget, Environmental Research Letters, 8, 014 026, http://stacks.iop.org/1748-9326/8/i=1/a=014026, 2013.

Schaphoff, S., von Bloh, W., Rammig, A., Thonicke, K., Biemans, H., Forkel, M., Gerten, D., Heinke, J., Jägermeyr, J., Knauer, J., Langerwisch, F., Lucht, W., Müller, C., Rolinski, S., and Waha, K.: LPJmL4 – a dynamic global vegetation model with managed land – Part 1: Model description, Geoscientific Model Development, 11, 1343–1375, https://doi.org/10.5194/gmd-11-1343-2018, 2018.

Schaphoff, S., Hötten, D., Müller, C., Gerten, D., Ostberg, S., and von Bloh, W.: Code and data for: "Implementing methane dynamics into the LPJmL6 model", https://doi.org/10.5281/zenodo.17877397, 2025a.

Schaphoff, S., von Bloh, W., Rammig, A., Thonicke, K., Biemans, H., Forkel, M., Gerten, D., Heinke, J., Jägermeyr, J., Langerwisch, F., Lucht, W., Rolinski, S., Waha, K., Ostberg, S., Wirth, S. B., Fader, M., Drüke, M., Jans, Y., Lutz, F., Herzfeld, T., Minoli, S., Porwollik, V., Stehfest, E., de Waal, L., Beringer (Erbrecht), T., Rost (Jachner), S., Gumpenberger, M., Heyder, U., Werner, C., Braun, J., Breier, J., Stenzel, F., Mathesius, S., Hemmen, M., Billing, M., Oberhagemann, L., Sakschewski, B., and Müller, C.: LPJmL: central open-source github repository of LPJmL at PIK, https://doi.org/10.5281/zenodo.17911633, 2025b.

Schneider, U., Becker, A., Finger, P., Meyer-Christoffer, A., Ziese, M., and Rudolf, B.: GPCC Full Data Monthly Product Version 2018 at 1.0°: Monthly Land-Surface Precipitation from Rain-Gauges built on GTS-based and Historical Data, Global Precipitation Climatology Centre (GPCC), https://doi.org/10.5676/DWD_GPCC/FD_M_V2018_100, 2017.

Sivapalan, M., Beven, K., and Wood, E. F.: On hydrologic similarity: 2. A scaled model of storm runoff production, Water Resources Research, 23, 2266–2278, https://doi.org/10.1029/WR023i012p02266, 1987.

Stanley, E. H., Casson, N. J., Christel, S. T., Crawford, J. T., Loken, L. C., and Oliver, S. K.: The ecology of methane in streams and rivers: patterns, controls, and global significance, Ecological Monographs, 86, 146–171, https://doi.org/10.1890/15-1027, 2016.

Stevenson, D. S., Zhao, A., Naik, V., O'Connor, F. M., Tilmes, S., Zeng, G., Murray, L. T., Collins, W. J., Griffiths, P. T., Shim, S., Horowitz, L. W., Sentman, L. T., and Emmons, L.: Trends in global tropospheric hydroxyl radical and methane lifetime since 1850 from AerChemMIP, Atmospheric Chemistry and Physics, 20, 12 905–12 920, https://doi.org/10.5194/acp-20-12905-2020, 2020.

Swenson, S. C. and Lawrence, D. M.: Assessing a groundwater and runoff parameterization using GRACE-based groundwater storage estimates, Journal of Advances in Modeling Earth Systems, 6, 779–799, https://doi.org/10.1002/2013MS000282, 2014.

Swenson, S. C., Lawrence, D. M., and Lee, H.: Improved simulation of the terrestrial hydrological cycle in permafrost regions by the Community Land Model, Journal of Advances in Modeling Earth Systems, 4, https://doi.org/https://doi.org/10.1029/2012MS000165, 2012a.

https://doi.org/10.5194/egusphere-2025-6210
Preprint. Discussion started: 22 January 2026

Swenson, S. C., Lawrence, D. M., and Lee, H.: Improved simulation of the terrestrial hydrological cycle in permafrost regions by the Community Land Model, Journal of Advances in Modeling Earth Systems, 4, n/a–n/a, https://doi.org/10.1029/2012MS000165, 2012b.

Takahashi, H., Yamauchi, T., Colmer, T. D., and Nakazono, M.: Aerenchyma Formation in Plants, in: Low-Oxygen Stress in Plants: Oxygen Sensing and Adaptive Responses to Hypoxia, pp. 247–265, Springer Vienna, Vienna, https://doi.org/10.1007/978-3-7091-1254-0_13, 2014.

Turetsky, M. R., Kotowska, A., Bubier, J., Dise, N. B., Crill, P., Hornibrook, E. R. C., Minkkinen, K., Moore, T. R., Myers-Smith, I. H., Nykänen, H., Olefeldt, D., Rinne, J., Saarnio, S., Shurpali, N., Tuittila, E.-S., Waddington, J. M., White, J. R., Wickland, K. P., and Wilmking, M.: A synthesis of methane emissions from 71 northern, temperate, and subtropical wetlands, Global Change Biology, 20, 2183–2197, https://doi.org/10.1111/gcb.12580, 2014.

U.S. Geological Survey: USGS EROS Archive - Digital Elevation - Global 30 Arc-Second Elevation (GTOPO30), https://www.usgs.gov/centers/eros/science/usgs-eros-archive-digital-elevation-global-30-arc-second-elevation-gtopo30?qt-science_center_objects=0#qt-science_center_objects, accessed: 2018, 2007a.

U.S. Geological Survey: USGS EROS Archive - Digital Elevation - HYDRO1k, https://www.usgs.gov/centers/eros/science/usgs-eros-archive-digital-elevation-hydro1k#overview, accessed: 2010, 2007b.

van den Pol-van Dasselaar, A.: Methane emissions from grasslands, internal phd, wu, Netherlands, https://doi.org/10.18174/201574, wU thesis 2483 Proefschrift Wageningen, 1998.

Verdin, K. L., Hall, F. G., Collatz, G. J., Meeson, B. W., Los, S. O., Brown de Colstoun, E., and Landis, D. R.: ISLSCP II HYDRO1k Elevation-derived Products, ISLSCP Initiative II Collection, Oak Ridge National Laboratory Distributed Active Archive Center (ORNL DAAC), Oak Ridge, Tennessee, USA, doi:10.3334/ORNLDAAC/1007, 2011.

von Bloh, W., Schaphoff, S., Müller, C., Rolinski, S., Waha, K., and Zaehle, S.: Implementing the nitrogen cycle into the dynamic global vegetation, hydrology, and crop growth model LPJmL (version 5.0), Geoscientific Model Development, 11, 2789–2812, https://doi.org/10.5194/gmd-11-2789-2018, 2018.

Vörösmarty, C. J., Fekete, B. M., and Tucker, B. A.: Global River Discharge, 1807–1991, Version 1.1 (RivDIS), https://doi.org/10.3334/ORNLDAAC/199, 1998.

Vörösmarty, C. J., Fekete, B. M., Meybeck, M., and Lammers, R. B.: Global system of rivers: Its role in organizing continental land mass and defining land-to-ocean linkages, Global Biogeochem. Cycles, 14, 599–621, https://doi.org/10.1029/1999GB900092, 2000.

Wada, Y. and Bierkens, M. F. P.: Sustainability of global water use: past reconstruction and future projections, Environmental Research Letters, 9, 104 003, https://doi.org/10.1088/1748-9326/9/10/104003, 2014a.

Wada, Y. and Bierkens, M. F. P.: Integrated assessment of global water resources using PCR-GLOBWB: Current state and future projections, Hydrology and Earth System Sciences, 18, 2853–2873, https://doi.org/10.5194/hess-18-2853-2014, 2014b.

Waha, K., Dietrich, J. P., Portmann, F. T., Siebert, S., Thornton, P. K., Bondeau, A., and Herrero, M.: Multiple cropping systems of the world and the potential for increasing cropping intensity, Global Environ. Change, 64, 102 131, https://doi.org/10.1016/j.gloenvcha.2020.102131, 2020.

Waha, K., Folberth, C., Biemans, H., Boere, E., Bondeau, A., Hartley, A. J., Hoogenboom, G., Jägermeyr, J., Liu, Y., Mathison, C., Müller, C., Nkwasa, A., Olin, S., Ruane, A. C., De Vos, K., White, J. W., Williams, K., and Yu, Q.: Land use

https://doi.org/10.5194/egusphere-2025-6210
Preprint. Discussion started: 22 January 2026

modelling needs to better account for multiple cropping to inform pathways for sustainable agriculture, Commun. Earth Environ., 6, 1–13, https://doi.org/10.1038/s43247-025-02724-0, 2025.

Walter, B. P. and Heimann, M.: A process-based, climate-sensitive model to derive methane emissions from natural wetlands: Application to five wetland sites, sensitivity to model parameters, and climate, Global Biogeochem. Cycles, 14, 745–765, http://dx.doi.org/10.1029/1999GB001204, 2000.

Wang, J., Akiyama, H., Yagi, K., and Yan, X.: Controlling variables and emission factors of methane from global rice fields, Atmospheric Chemistry and Physics, 18, 10 419–10 431, https://doi.org/10.5194/acp-18-10419-2018, 2018.

Wang, J., Ciais, P., Smith, P., Yan, X., Kuzyakov, Y., Liu, S., Li, T., and Zou, J.: The role of rice cultivation in changes in atmospheric methane concentration and the Global Methane Pledge, Global Change Biology, 29, 2776–2789, https://doi.org/https://doi.org/10.1111/gcb.16631, 2023a.

Wang, L., Arora, V. K., Bartlett, P., Chan, E., and Curasi, S. R.: Mapping of ESA's Climate Change Initiative land cover data to plant functional types for use in the CLASSIC land model, Biogeosciences, 20, 2265–2282, https://doi.org/10.5194/bg-20-2265-2023, 2023b.

Wang, Y., Hu, Z., Liu, C., Wu, Z., and Chen, S.: Methane emissions in japonica rice paddy fields under different elevated CO2 concentrations, Nutrient Cycling in Agroecosystems, 122, 173–189, https://doi.org/10.1007/s10705-022-10197-2, 2022.

Wania, R., Ross, I., and Prentice, I. C.: Integrating peatlands and permafrost into a dynamic global vegetation model: 2. Evaluation and sensitivity of vegetation and carbon cycle processes, Global Biogeochem. Cycles, 23, GB3015–, http://dx.doi.org/10.1029/2008GB003413, 2009.

Wania, R., Ross, I., and Prentice, I.: Implementation and evaluation of a new methane model within a dynamic global vegetation model: LPJ-WHyMe v1. 3, Geoscientific Model Development Discussions, 3, 1–59, 2010.

Wassmann, R., Neue, H.-U., Lantin, R. S., Buendia, L. V., and Rennenberg, H.: Characterization of Methane Emissions from Rice Fields in Asia. I. Comparison among Field Sites in Five Countries, Nutrient Cycling in Agroecosystems, 58, 1–12, https://doi.org/10.1023/A:1009848813994, 2000.

Whalen, S. C. and Reeburgh, W. S.: Methane emissions from boreal wetlands, Journal of Geophysical Research: Atmospheres, 96, 16 971–16 982, https://doi.org/10.1029/91JD00048, 1991.

Wiesenburg, D. A. and Guinasso Jr, N. L.: Equilibrium solubilities of methane, carbon monoxide, and hydrogen in water and sea water, Journal of chemical and engineering data, 24, 356–360, 1979.

Wild, M., Folini, D., Hakuba, M. Z., Schär, C., Seneviratne, S. I., Kato, S., Rutan, D., Ammann, C., Wood, E. F., and König-Langlo, G.: The energy balance over land and oceans: An assessment based on direct observations and CMIP5 climate models, Climate Dynamics, 44, 3393–3429, https://doi.org/10.1007/s00382-014-2430-z, 2015.

Wirth, S. B., Braun, J., Heinke, J., Ostberg, S., Rolinski, S., Schaphoff, S., Stenzel, F., von Bloh, W., Taube, F., and Müller, C.: Biological nitrogen fixation of natural and agricultural vegetation simulated with LPJmL 5.7.9, Geoscientific Model Development, 17, 7889–7914, https://doi.org/10.5194/gmd-17-7889-2024, 2024.

Xu, L., Saatchi, S. S., Yang, Y., Yu, Y., Pongratz, J., Bloom, A. A., Bowman, K., Worden, J., Liu, J., Yin, Y., Domke, G., McRoberts, R. E., Woodall, C., Nabuurs, G.-J., de Miguel, S., Keller, M., Harris, N., Maxwell, S., and Schimel, D.: Dataset for "Changes in Global Terrestrial Live Biomass over the 21st Century", https://doi.org/10.5281/zenodo.4161694, data set, 2021.

https://doi.org/10.5194/egusphere-2025-6210
Preprint. Discussion started: 22 January 2026

Xu, R., Dai, J., Luo, W., Yin, X., Li, Y., Tai, X., Han, L., Chen, Y., Lin, L., and Li, G.: A photothermal model of leaf area index for greenhouse crops, Agricultural and Forest Meteorology, 150, 541–552, https://doi.org/10.1016/j.agrformet.2010.01.019, 2010.

Yamamoto, S., Alcauskas, J. B., and Crozier, T. E.: Solubility of methane in distilled water and seawater, Journal of Chemical and Engineering Data, 21, 78–80, 1976.

Yan, X., Akiyama, H., Yagi, K., and Akimoto, H.: Global estimations of the inventory and mitigation potential of methane emissions from rice cultivation conducted using the 2006 IPCC Guidelines, Global Biogeochemical Cycles, 23, GB2002, https://doi.org/10.1029/2008GB003299, 2009.

Yang, T., He, Q., Jiang, J., Sheng, L., Jiang, H., and He, C.: Impact of Water Table on Methane Emission Dynamics in Terrestrial Wetlands and Implications on Strategies for Wetland Management and Restoration, Wetlands, 42, 120, https://doi.org/10.1007/s13157-022-01634-7, 2022.

Zeng, X. and Decker, M.: Improving the numerical solution of soil moisture–based Richards equation for land models with a deep or shallow water table, Journal of Hydrometeorology, 10, 308–319, https://doi.org/10.1175/2008JHM1011.1, 2009.

Zhang, B., Tian, H., Lu, C., Dangal, S. R. S., Yang, J., and Pan, S.: Manure nitrogen production and application in cropland and rangeland during 1860–2014: A 5-minute gridded global data set for Earth system modeling, Earth Syst. Sci. Data Discuss., pp. 1–35, https://doi.org/10.5194/essd-2017-11, 2017.

Zhang, B., Tian, H., Lu, C., Dangal, S. R. S., Yang, J., and Pan, S.: Manure nitrogen production and application in cropland and rangeland during 1860 - 2014: A 5-minute gridded global data set for Earth system modeling, [Data set], PANGAEA, https://doi.org/10.1594/PANGAEA.871980, accessed 2022-05-04, 2017.

Zhang, Z., Fluet-Chouinard, E., Jensen, K., McDonald, K., Hugelius, G., Gumbricht, T., Carroll, M., Prigent, C., Bartsch, A., and Poulter, B.: Development of the global dataset of Wetland Area and Dynamics for Methane Modeling (WAD2M), Earth System Science Data, 13, 2001–2023, https://doi.org/10.5194/essd-13-2001-2021, 2021.

Zhong, L., Dai, Z., Fang, P., Cao, Y., and Wang, L.: A Review: Tree Species Classification Based on Remote Sensing Data and Classic Deep Learning-Based Methods, Forests, 15, https://doi.org/10.3390/f15050852, 2024.

Zhu, Y. and Li, H.: Methane emissions from rice paddies in the Yangtze River Delta region of China: synthesis of new estimates, International Journal of Environmental Science and Technology, https://doi.org/10.1007/s13762-024-06050-4, 2024.